GHARDA INSTITUTE OF TECHNOLOGY

A/P: LAVEL, TAL.KHED, DIST.RATNAGIRI.
Tel.: 02356 - 273134, Fax: 02356 – 262980
Website: www.git-india.edu.in, Email: principal@git-india.edu.in

Technical Magazine

Index

Crack Detection in A Cantilever Beam Using Correlation Model and Machine Learning Approach

Vikas KHALKAR
Faculty, Gharda Institute of Technology, Lavel, India,
e-mail: vikas_khalkar@rediffmail.com

Pratik OAK
Faculty, Gharda Institute of Technology, Lavel, India,
e-mail: pvoak@git-india.edu.in

A MOSHI
Faculty, National Engineering College, Kovilpatti, India,
e-mail: moshibeo2010@gmail.com

Pon HARIHARASAKHTISUDHAN
Faculty, Sri Krishna College of Technology, Kovaipudur, India,
e-mail: harimeed2012@gmail.com

Lalitkumar JUGULKAR
Faculty, Rajarambapu Institute of Technology, Islampur, Sangli, India,
e-mail: lalitkumar.jugulkar@ritindia.edu

Raman BANE
Faculty, Gharda Institute of Technology, Lavel, India,
e-mail: rrbane@git-india.edu.in

Abstract: - Crack in a structural member alters local stiffness that affects the dynamic response, such as natural frequency and mode shapes. The purpose of structural health monitoring is to diagnose and predict structural health. In this paper, a correlation model is developed to detect crack parameters, i.e., crack location and crack depth, in the beam. To evaluate the authenticity of the developed correlation model, the Artificial Intelligence-based approach is used to predict the crack parameters. Twenty-three Artificial Intelligence algorithms were used to predict the locations and depths of the crack in a cantilever beam. The developed correlation model used the first two normalized natural frequencies to predict the crack parameters. On the other hand, the first three normalized natural frequencies were used to input the machine learning models to predict the crack parameters. In this research study, V-shaped and U-shaped open edges cracks were considered on the cantilever beam. FEA software, ANSYS, is used to do the modal vibration analysis of various cracked cases of beams. The data set of V-shaped and a U-shaped cracked case obtained from finite element analysis (FEA) were used to develop the correlation model and machine learning models. The results for crack locations and crack depth obtained from the correlation model and machine learning models agree with the actual results. In the future, the proposed correlation model of crack detection can be used to detect cracks in more complicated structures.

Keywords: - Correlation model, ANN, Machine learning, Natural frequency, FEA and Crack location.

1. INTRODUCTION

Beams are used in various structural applications in the automotive, civil, and aerospace industries. The presence of crack affects the structure's stiffness and affects the mechanical response of the whole structure to a more considerable extent. Due to these changes, there is a reduction in modal frequencies and mode shapes. Therefore, it is feasible to anticipate the crack characteristics by determining changes in the vibration parameters [1].

A fault diagnosis method based on genetic algorithms (GAs), and a model of damaged (cracked) structure is proposed. For modeling the cracked-beam structure an analytical model of a cracked cantilever beam is utilized, and natural frequencies were

obtained using numerical methods. This method utilized genetic algorithms to monitor the possible changes in the natural frequencies of the structure. The identification of the crack location and depth in the cantilever beam is formulated as an optimization problem, and binary and continuous genetic algorithms (BGA, CGA) are used to find the optimal location and depth by minimizing the cost function which is based on the difference of measured and calculated natural frequencies. Khatir et al. [2] presents a methodology for nondestructive detection, localization, and quantification of various damages in simple and continuous beams, as well as a more sophisticated structure, the two-dimensional frame structure.

The Firefly Algorithm and Genetic Algorithm are employed as optimization methods, while the Coordinate Modal Assurance Criterion is used as an objective function in the suggested methodology. The findings suggest that the proposed combination of the Coordinate Modal Assurance Criterion and the Firefly Algorithm or Genetic Algorithm can be utilized to quickly discover various local structural faults in complex structures. Visual inspection of cracks and damages is unsuitable and not worth considering in most cases; thus, non-destructive testing (NDT) methods like thermography, ultrasonic testing, X-ray diffraction, etc., are used to predict damage in the structures. However, these methods require time and expenses. So the other possible methods are motivated to be developed [3]. In this analogy, the use of mathematical methods, vibration-based methods, and soft-computing techniques such as artificial neural networks (a subfield of artificial intelligence) are promising and favorable.

Nasiri et. Al [4] presented a review paper utilizing Artificial Intelligence (AI) methods for mechanical fault detection. They discussed the applications of Bayesian networks, GA (genetic algorithms), fuzzy logic, case-based reasoning, and ANN, i.e., artificial neural networks. Sutar et al. [3] investigated transverse crack in cantilever beam by proposing a neural network-based controller. Crack stiffness to beam elemental stiffness matrix was used to obtain a homogenous linear elastic beam finite element by Teidj et al. [5] and used the measurement of the changes in the beam frequencies and observed their variations to detect the crack defect characteristics.

Thatoi et al. [6] described the Cascade Forward Back Propagation (CFBP) network to detect cracks in structural beams with the idea of changes in the natural frequencies and their measurements. Pan et al. [7] developed a two-stage approach combining of artificial neural network (ANN) and genetic algorithm (GA) to identify crack characteristics. Orhan et al. [8] introduced the new crack model

(combination of V-shaped and Rectangular shaped crack) with the known V-shaped cracked model in order to investigate the effect of geometry change on the natural frequencies and mode shapes under free vibration loading. The result of this study reveals that composite structures are less sensitive for the geometry change as long as vibration characteristics are concerned. Gillich et al. [17] proposed two machine learning methods, random forest (RF) and the artificial neural network (ANN), as searching tools in this paper. Their databases contain damage scenarios for a prismatic cantilever beam with one crack and ideal and non-ideal boundary conditions.

The crack assessment was made in two steps. First, a coarse damage location was found from the networks trained for scenarios comprising the whole beam. Afterward, the assessment was made involving a particular network trained for the segment of the beam on which the crack was previously found. They used the two machine learning methods to estimate the crack location and severity with high accuracy for both simulation and laboratory experiments.

Regarding the location of the crack, which was the main goal of the practitioners, the errors were less than 0.6%. Based on these achievements, they concluded that the damage assessment we proposed, in conjunction with the machine learning methods, is robust and reliable. In this paper, Tufisi et al. [18] proposed a model for detecting transverse cracks in simply supported beams, which can be part of more complex structural systems. The relative frequency shifts of the structure are considered a basis for damage identification.

An original method developed by the authors is employed to evaluate the required modal parameters. A multi-stage optimization approach based on the rigidity loss suffered by the affected structure is employed to recognize the locations of potential cracks accurately. The outcome presented in this research shows the computational ability of the proposed model to indicate the presence and location of damages in the beam-like structures. In this study, Tufisi et al. [19] present a method (DS-SHC) used for estimating the DS for closed and open transverse cracks in beam-like structures using the intact and damaged beam deflections under its weight and a Stochastic Hill Climbing (SHC) algorithm. After describing the procedure of applying DS-SHC, we calculate for a prismatic cantilever beam the severities for different crack types and depths. The results are tested by comparing the DS obtained with DS-SHC with those acquired from dynamic tests made using professional simulation software.

We obtained a good fit between the severities determined in these two ways. Subsequently, they performed laboratory experiments and found that the

severities obtained with the DS-SHC method can accurately predict the frequency changes due to the crack. Hence, these severities are a valuable tool for damage detection.

In this paper, Tufisi et al. [20] proposed an analytical approach for generating the data needed to train a Random Forest model (RF) that will perform the SHM task to detect, locate, and assess the severity of transverse cracks in beam-like structures.

Using an original method, they calculated the relative frequency shifts (RFS) for different damage scenarios and used the generated data to train the RF model. Subsequently, the RF model is validated using data obtained from FEM simulations using different mesh sizes for different damage scenarios on steel beams.

The results indicate that the RF model can detect the presence of the defect and find the position and depth of the transverse cracks very precisely if the crack is located in the area where the beam achieves the maximum bending moment. By correctly categorizing accelerometer data, deep learning algorithms achieve the objective [21] of evaluating the condition of beams in a non-invasive manner. While an essential indicator, the high probabilistic accuracy attained on the validation set is typically insufficient in most practical circumstances.

When damage occurs, the accurate prognosis must also be comprehensible to humans, considering the factors that led to that specific outcome. It will increase confidence and the chance of rectifying functioning conditions in the future. We use the LIME and SHAP algorithms to correlate model-neutral global and local explanations to create an interpretable model. We offer a compound stability-fit compensation index due to the potential instability of the local explanations.

The action of fatigue load on structures results in single-sided open-edged cracks. Stress corroded turbine blades cause localized loss of the material in them. After removing the localized material from the blade, the damage location can be mapped into U-shaped or V-shaped open-edged cracks. As a result, this research study has considered two types of open-edged crack on the cantilever beam.

The research paper's analysis is separated into two parts. The natural frequencies for various V-shaped and U-shaped open-edged cracked cases were determined using the numerical method in the first half.

Furthermore, in the second half, a developed correlation model and machine learning approach were employed to cracked beam to detect the crack parameters in the cantilever beam.

2. INVERSE METHOD OF CRACK DETECTION WITH CORRELATION MODEL

This research study proposes a correlation model between the normalized natural frequencies and normalized crack parameters, i.e., crack location and crack depth, as a forward approach. It is given in Equation (1).

$$Y = f\left(\frac{L_1}{L}, \frac{a}{H}\right) \qquad (1)$$

Y is the ratio between the natural frequency of the cracked beam and the natural frequency of the un-cracked beam.

L_1/L is the ratio of the distance of the crack from the cantilevered end to the length of the beam.

a/H is the ratio of crack depth to the depth of the beam.

$$f\left(\frac{L_1}{L}, \frac{a}{H}\right) - Y = 0 \qquad (2)$$

Then, inverse method using correlation model is proposed to detect the location and depth of the crack in a cantilever beam.

3. CORRELATION MODEL

The natural frequencies of the cracked beam were normalized with that of the intact beam. Y_1 and Y_2 are the normalized natural frequencies in the first and second modes, respectively. They were plotted against the dimensionless crack parameters, i.e., crack location and crack depth. The first and second natural frequencies were used to obtain the correlation model for the curve fitting. Only two equations were required to find two unknown crack parameters, i.e., crack location and depth. Based on the non-linear relationship between crack parameters and frequency ratios, non-linear polynomial curve fitting was used to get two equations for two natural frequency ratios at the first and second modes. Equations 3 and 4 were developed using the data set of V-shaped cracked cases.

Similarly, Equations (5) and (6) were developed using the data set of U-shaped cracked cases. The data set of V-shaped and U-shaped cracked cases are presented in Table 1. Correlation models for the natural frequencies ratio at the first and second modes for V-shaped cracked cases were developed, and they are given in Equation (3) and Equation (4), respectively. Similarly, the correlation models for the natural frequencies ratio at the first and second modes

for U-shaped cracked cases were developed. They are given in Equation (5) and Equation (6), respectively.

$$1.03190 - \left(0.24618 * \left(\tfrac{L_1}{L}\right)\right) - \left(0.10796 * \left(\tfrac{a}{H}\right)\right) + \left(0.60948 * \left(\tfrac{L_1}{L}\right) * \left(\tfrac{a}{H}\right)\right) + \left(0.46021 * \left(\tfrac{L_1}{L}\right)^2\right) - \left(0.54735 * \left(\tfrac{a}{H}\right)^2\right) - \left(0.90726 * \left(\tfrac{L_1}{L}\right)^2 * \left(\tfrac{a}{H}\right)\right) + \left(1.52640 * \left(\tfrac{L_1}{L}\right) * \left(\tfrac{a}{H}\right)^2\right) - (0.21756 * \left(\tfrac{L_1}{L}\right)^3) - \left(0.63026 * \left(\tfrac{a}{H}\right)^3\right) - Y_1 = 0 \qquad (3)$$

$$0.82733 + \left(1.11904 * \left(\tfrac{L_1}{L}\right)\right) + \left(0.47147 * \left(\tfrac{a}{H}\right)\right) - \left(3.13757 * \left(\tfrac{L_1}{L}\right) * \left(\tfrac{a}{H}\right)\right) - \left(1.70394 * \left(\tfrac{L_1}{L}\right)^2\right) + \left(0.40455 * \left(\tfrac{a}{H}\right)^2\right) + \left(3.09003 * \left(\tfrac{L_1}{L}\right)^2 * \left(\tfrac{a}{H}\right)\right) - \left(0.34222 * \left(\tfrac{L_1}{L}\right) * \left(\tfrac{a}{H}\right)^2\right) + (0.70575 * \left(\tfrac{L_1}{L}\right)^3) - \left(0.53943 * \left(\tfrac{a}{H}\right)^3\right) - Y_2 = 0 \qquad (4)$$

$$1.03189 - \left(0.26371 * \left(\tfrac{L_1}{L}\right)\right) - \left(0.11329 * \left(\tfrac{a}{H}\right)\right) + \left(0.56253 * \left(\tfrac{L_1}{L}\right) * \left(\tfrac{a}{H}\right)\right) + \left(0.53075 * \left(\tfrac{L_1}{L}\right)^2\right) - \left(0.55074 * \left(\tfrac{a}{H}\right)^2\right) - \left(0.86077 * \left(\tfrac{L_1}{L}\right)^2 * \left(\tfrac{a}{H}\right)\right) + \left(1.59538 * \left(\tfrac{L_1}{L}\right) * \left(\tfrac{a}{H}\right)^2\right) - (0.27456 * \left(\tfrac{L_1}{L}\right)^3) - \left(0.69112 * \left(\tfrac{a}{H}\right)^3\right) - Y_1 = 0 \qquad (5)$$

$$0.81314 + \left(1.22783 * \left(\tfrac{L_1}{L}\right)\right) + \left(0.49187 * \left(\tfrac{a}{H}\right)\right) - \left(3.32663 * \left(\tfrac{L_1}{L}\right) * \left(\tfrac{a}{H}\right)\right) - \left(1.90931 * \left(\tfrac{L_1}{L}\right)^2\right) + \left(0.43864 * \left(\tfrac{a}{H}\right)^2\right) + \left(3.29483 * \left(\tfrac{L_1}{L}\right)^2 * \left(\tfrac{a}{H}\right)\right) - \left(0.39802 * \left(\tfrac{L_1}{L}\right) * \left(\tfrac{a}{H}\right)^2\right) + (0.81597 * \left(\tfrac{L_1}{L}\right)^3) - \left(0.56162 * \left(\tfrac{a}{H}\right)^3\right) - Y_2 = 0 \qquad (6)$$

To determine the locations and depths of V-shaped cracks in a cantilever beam, Equation (3) and Equation (4) were used. Similarly, Equation (5) and Equation (6) were used to determine the locations and depths of U-shaped cracks in a cantilever beam. The third order correlation models presented in equations (3), (4), (5) and (6) were generated by performing regression analysis with the aid of Design Expert software.

The reliability of the correlation models is generally determined by the R-squared values. The R-squared value nearer to '1' represents the good fit of the data on the generated correlation models. In the present work, the R-squared values of the generated correlation models presented in equations (3), (4), (5) and (6) were found to be 0.9943, 0.8890, 0.9939 and 0.8914 respectively. As the R-squared values of all the generated correlation models are nearer to '1', the models are ensured to be reliable.

To predict the crack depth and crack locations in a V-shaped cracked beam, the first and second normalized frequencies were used and were substituted in Equation (3) and Equation (4), respectively. Afterward, Equations (3) and Equation (4) were solved simultaneously using Microsoft Excel to predict the locations and depth of V-shaped cracks in a cantilever beam.

Similarly, Equations (5) and Equation (6) were solved simultaneously using Microsoft Excel to predict the locations and depths of U-shaped cracks in a cantilever beam.

4. SIMULATED CRACK CONFIGURATIONS

Geometric properties: The cross-sectional area and length of the beam are 0.02×0.02 m^2 and 0.32 m, respectively.

Material properties: Young's modulus (E) = 2.104×10^{11} N/m^2, Mass density (ρ) = 7820 kg/m^3, Mass (M) = 1.00096 kg.

In this study, a total of 160 cracked specimens of steel materials were considered to investigate the effect of different kinds of cracks on the natural frequencies of a cantilever beam. The width of the crack (along the longitudinal direction) is chosen as 0.5 mm. Two separate cases were considered, i.e., case 1 and case 2.

Case 1: 80 specimens of V-shaped cracked cases were considered in this case. This case was subdivided into five sub-cases. In the first sub-case, 16 specimens were considered. 50 mm crack location was chosen for the crack, and at this location, crack depth was varied from 1 mm to 16 mm by an interval of 1 mm.

The second, third, fourth, and fifth sub cases were similar to that of the first sub-case; the only difference was that instead of 50 mm crack location; 100 mm, 150 mm, 200 mm, and 250 mm cracks locations were chosen for the second, third, fourth and fifth sub-cases respectively.

Case 2: Case 2 was like case 1; the only difference was that instead of V-shaped crack geometries, U-shaped crack geometries were considered on the specimens.

The one case of V-shaped and U-shaped cracked cases are shown in Figure 1 and Figure 2 respectively.
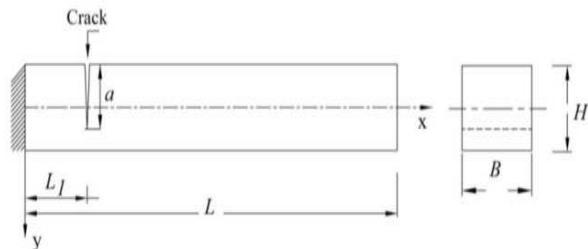
Figure 1. Cracked cantilever beam with V-shaped crack.
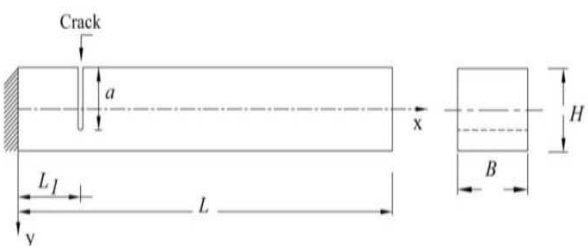
Figure 2. Cracked cantilever beam with U-shaped crack.

5. FINITE ELEMENT MODELING AND ANALYSIS

ANSYS finite element program [9] was used to determine the natural frequency of cracked cantilevered beams. For this purpose, a rectangular zone of the required geometric properties was created, and then this zone was extruded to obtain the model in three dimensions. A small area of dimensional requirements was created and extruded to represent the crack in the primary model. After that subtract command was used for subtracting the small volume from the volume of the primary model [10, 11, 22 & 23]. Then a cracked three-dimensional solid model gets obtained. A Solid 186 (tetrahedral) element was used to mesh the cracked model of a cantilever beam. After meshing, the FEA model carried 6159 elements. Results of natural frequencies remained almost the same irrespective of the sizes of the elements (5 mm, 6 mm, and 7 mm) tried in the analysis. Furthermore, a 5 mm mesh size was finalized to mesh all the models. This element has some unique features, i.e., stress stiffening, large strain, and large deflection. Finite element boundary conditions were applied on the beam to constrain all degrees of freedom of the cantilevered end of the beam. The Block Lanczos eigenvalue solver was used to compute the natural frequencies of cracked beams. Mesh independent study was carried out to study the effect of mesh size on the natural frequency of cracked beams. Through mesh-independent study, it was found that natural frequency results were independent of the mesh size. Figures 3–5 illustrate a few natural frequency plots.

Figure 3. First natural frequency plot of V-shaped cracked case: Location ratio= 0.3125; depth ratio= 0.4.

Figure 4. Second natural frequency plot of V-shaped cracked case: Location ratio= 0.3125; depth ratio= 0.4.

Figure 5. Third natural frequency plot of V-shaped cracked case: Location ratio= 0.3125; depth ratio= 0.4.

6. METHODLOGY

To predict the crack depth and crack locations in the beams, the input and output variables have normalized; hence, they are in the same range of 0 to 1.

The actual experimental results were compared with the simulation through machine learning-based classifiers. *Machine learning* is the self-prediction methodology that takes a few parameters as an input and known output responses. Based on these two input data, the algorithms generate a self-learning model. Various algorithms are suggested [15] in the state-of-art methods and they are used in most prediction related applications.

Decision Tree, Discriminant Analysis, Support Vector machines, Nearest Neighbor, Ensemble classifier, and Artificial Neural Network-based prediction are made in the proposed work. These classifier algorithms have their own trained model generation principles and few sub-algorithms. The discriminant analysis works on assuming different Gaussian distributions based on data generation. For linear discriminant analysis, each model class has the

same covariance matrix with varying mean values. In contrast, variations in both mean and covariance of each class are in the quadratic discriminant analysis (QDA). Predict classifies to minimize the expected classification cost. The SVM binary classification algorithm finds an optimal hyper-plane that separates the data into two classes. Depending on the homogeneity of the input parameters, the width of the hyper-plane varies. Prediction can be made for more accuracy [13-14] using linear or non-linear filters/kernels. A k-nearest neighbor classifier known as KNN is based on a distance metric. It has various distance metrics like cosine, cubic, Euclidean (weighted), etc. This classifier is considered one of the most straightforward prediction techniques.

Ensemble classifier uses a vote of different classifiers for class prediction. Five ensemble classifiers are most commonly used in state-of-art methodologies viz. Ensemble Boosted Trees, Ensemble Bagged Trees, Ensemble Subspace Discriminant, Ensemble Subspace KNN, and Ensemble RUS Boosted Trees.

The Decision Tree classifier predicts [12] on a hierarchy basis. It does not require any pre-requisite knowledge and is also considered as most straightforward prediction technique.

An artificial neural network (ANN) is a famous technique [15] that resembles the human brain guessing mechanism. It is the artificial intelligence (AI) base preferred for most complex problems. Feed forward ANN is the method we used in our proposed work. Performance Metrics Used for Analysis.

Confusion Matrix- The tabular representation of prediction performance and error factor is called as confusion matrix. It shows the performance as predicted class Vs true class.
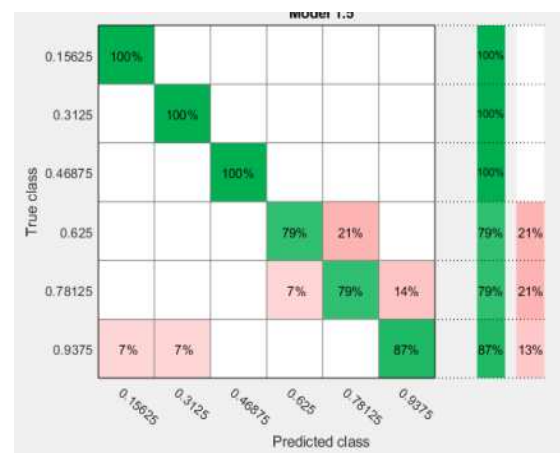
AUC Curve- The graph showing [16] the model performance at all thresholds is called as ROC curve. It plots two parameters as true positive (TP) and false positive (FP). Area under the ROC curve is called as AUC. It is aggregate measure of performance and ranges between 0 (100% wrong) & 1 (100% correct).

7. RESULTS AND DISCUSSION

Numerical method was used to examine the natural frequencies of cracked cantilever beams with various crack depths, crack locations and crack geometries. Then the relationship between different cracked geometries and natural frequencies is investigated. The data tabulated in Table 1 are the neural network's training data for V-shaped and U-shaped cracked cases.

As explained in methodology, we made a comparative analysis of various classifiers as prediction algorithms. All classifiers are trained with

a cross-validation factor 5. The standard Classifier learning app available in MATLAB 2018a had used for classification. Details of a parameter we used for each classifier are tabulated in Table 2. A comparison of performances of all the classifiers for accuracy is tabulated in Tables 3 and 4. The experimentation was carried out for both V-shaped and U-shaped cracked cases of a cantilever beam for crack parameters, i.e., crack location (L_1/L) and crack depth ratios (a/H). Classifiers outperformed for predicting the crack locations, i.e., L_1/L in beams. However, the accuracy of the same classifiers is poor for predicting the depth of the crack in beams, i.e., a/H. Quadratic discriminated analysis (QDA) had given the highest accuracy for predicting crack locations. It gave 94.3% accuracy for V-shaped cracked cases and 90.8% for U-shaped cracked cases. The confusion matrix and AUC curve represent better results given by this QDA. The Confusion Matrix of Quadratic Discriminated Analysis of U-shaped and V-shaped cracked cases is shown in Figure 6.

a) **U-shaped Confusion Matrix**
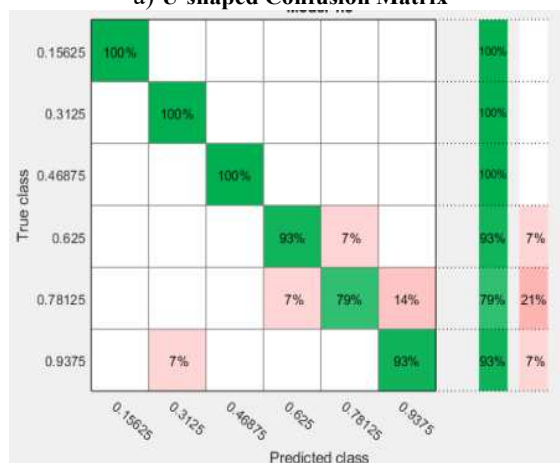
b) **V-shaped Confusion Matrix**
Figure 6. Confusion Matrix of Quadratic Discriminant Analysis (QDA)

AUC Curve of Quadratic Discriminated Analysis is shown in Figure 7. The graph shows the model performance at all thresholds is called as ROC curve.

However, the performance of ANN is best for predicting the crack parameters of defective beams amongst all 22 classifiers.
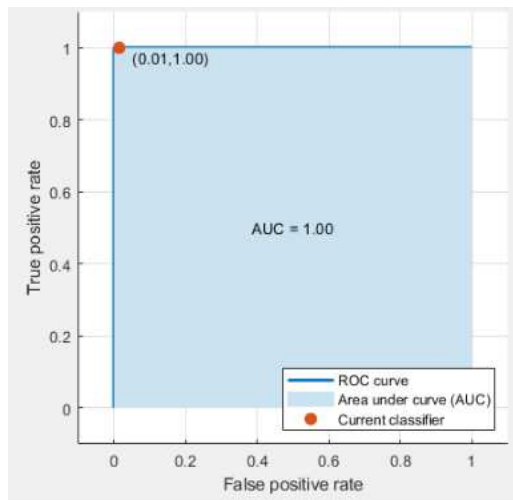
a) **U-shaped AUC Curve**
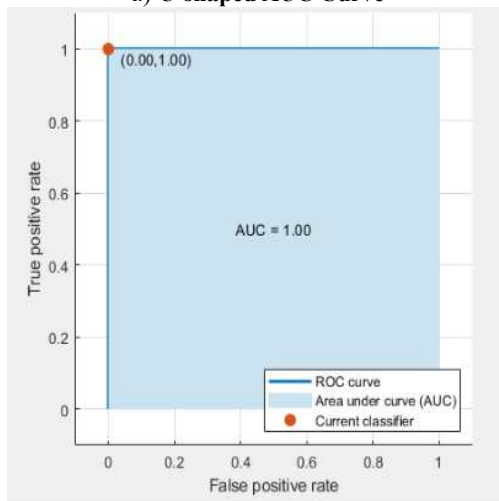
b) **V-shaped AUC Curve**

Figure 7. AUC Curve of Quadratic Discriminant Analysis (QDA)
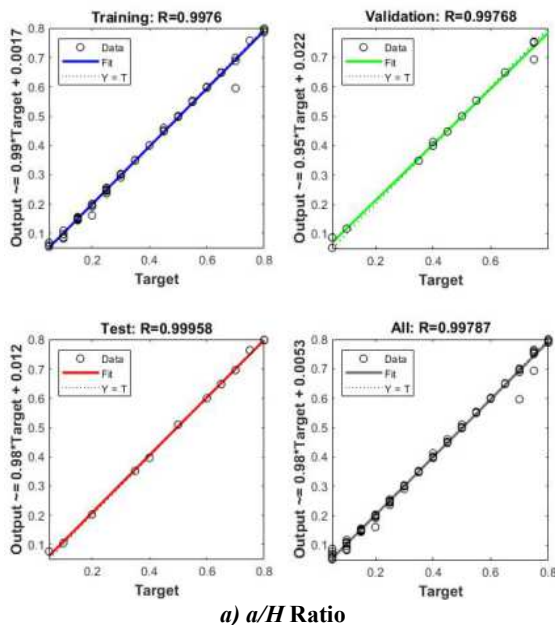
a) a/H Ratio
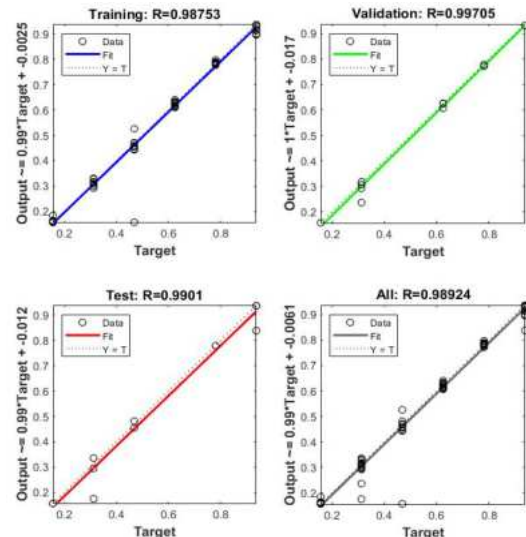
b) L_1/L **Ratio**

Figure 8. Performance of ANN for U-shaped cracked cases
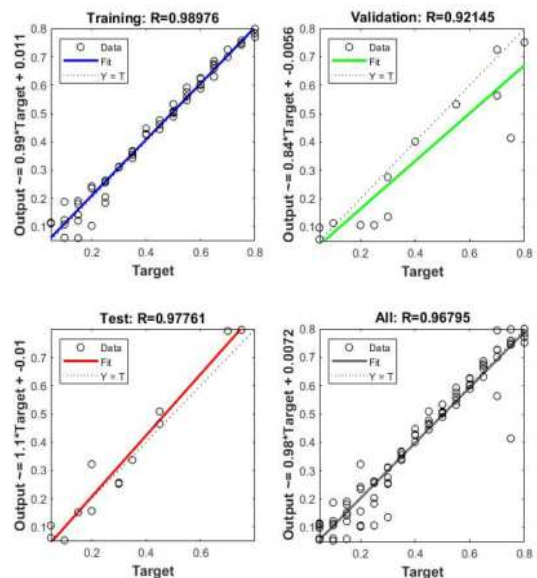
a) *a/H* **Ratio**
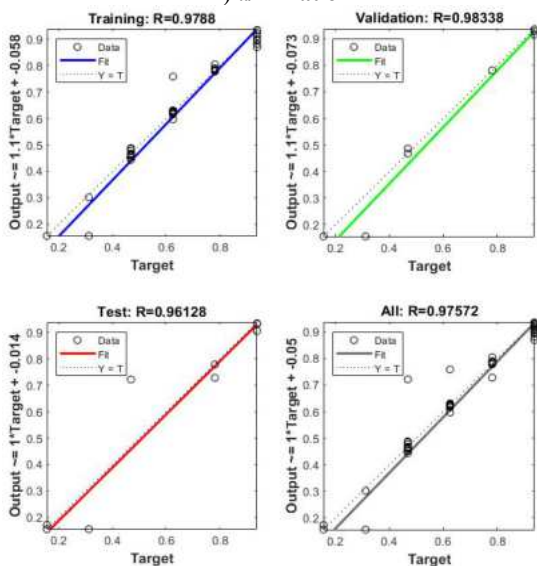
b) L_1/L **Ratio**

Figure 9. Performance of ANN for V-shaped cracked cases.

The performance of ANN for both U-shaped and V-shaped cracked cases is shown in Figure 8 and 9 respectively.

The predicted crack depths (a/H) and crack locations (L_1/L) using ANN and correlation model for V-shaped and U-shaped cracked cases are presented in Table 5 and Table 6. From, Figure 10 and 11, it is clear that the correlation model and ANN model gives good prediction for the crack depths and crack locations. The predicted crack depths and crack

locations are compared with the actual crack parameters for the same configurations. When comparing the findings of Table 5, it is evident that the ANN model performed well in predicting the crack depths and positions in U-shaped cracked cases. As a result, the ANN model can better predict the occurrence of U-shaped cracks than V-shaped cracks in beams for the same configurations.

Table 1. Training data of V-shaped and U-shaped cracked cases to the neural network.

Sr. No.			V-shaped cracked cases: Relative natural frequency			U-shaped cracked cases: Relative natural frequency		
	a/H	L_1/L	f_{r1}	f_{r2}	f_{r3}	f_{r1}	f_{r2}	f_{r3}
1	0.05	0.15625	0.998778	0.999901	1	0.998228	0.999802	0.999964
2	0.1	0.15625	0.994563	0.999405	0.999891	0.992852	0.999305	0.999854
3	0.15	0.15625	0.986987	0.998611	0.999709	0.984054	0.998313	0.999636
4	0.2	0.15625	0.976356	0.997519	0.999454	0.972141	0.997023	0.999308
5	0.25	0.15625	0.962488	0.99603	0.99909	0.956317	0.995335	0.998944
6	0.3	0.15625	0.944282	0.994145	0.998653	0.937256	0.993351	0.998434
7	0.35	0.15625	0.922959	0.991911	0.998107	0.91294	0.990919	0.997815
8	0.4	0.15625	0.894673	0.989063	0.997378	0.88563	0.98813	0.997087
9	0.45	0.15625	0.864919	0.986195	0.99665	0.853006	0.984934	0.996213
10	0.5	0.15625	0.828262	0.982662	0.995667	0.814944	0.981362	0.995157
11	0.55	0.15625	0.786229	0.978861	0.994502	0.770345	0.977332	0.993919
12	0.6	0.15625	0.74053	0.974911	0.993337	0.719941	0.973025	0.992499
13	0.65	0.15625	0.682001	0.970177	0.991625	0.660679	0.968331	0.990824
14	0.7	0.15625	0.621579	0.965661	0.989987	0.595045	0.963478	0.988822
15	0.75	0.15625	0.548192	0.96047	0.987766	0.520192	0.958347	0.986455
16	0.8	0.15625	0.467675	0.955468	0.985253	0.435282	0.953176	0.983542
17	0.05	0.3125	0.999389	0.999802	0.999782	0.999022	0.999702	0.999636
18	0.1	0.3125	0.997067	0.999008	0.998835	0.99609	0.998611	0.998471
19	0.15	0.3125	0.992852	0.99742	0.997196	0.991386	0.996923	0.99665
20	0.2	0.3125	0.986804	0.995137	0.994902	0.984665	0.994442	0.994247
21	0.25	0.3125	0.978983	0.992279	0.992208	0.97599	0.991266	0.991298
22	0.3	0.3125	0.969208	0.988656	0.992208	0.96487	0.987227	0.987766
23	0.35	0.3125	0.956806	0.98419	0.98529	0.950819	0.982205	0.983724
26	0.5	0.3125	0.897055	0.963517	0.970507	0.886486	0.960193	0.967994
27	0.55	0.3125	0.867058	0.953613	0.963662	0.854778	0.94997	0.96144
28	0.6	0.3125	0.831745	0.942646	0.956671	0.81641	0.93816	0.954231
29	0.65	0.3125	0.787573	0.929248	0.948915	0.767595	0.923948	0.945711
30	0.7	0.3125	0.735215	0.914738	0.940468	0.708822	0.908178	0.936353
31	0.75	0.3125	0.666606	0.89731	0.929872	0.638258	0.890939	0.925794
32	0.8	0.3125	0.582521	0.878186	0.918111	0.547733	0.871586	0.912759
33	0.05	0.46875	0.999695	0.999206	0.999964	0.999572	0.998809	0.999927
34	0.1	0.46875	0.998717	0.99603	0.999891	0.99835	0.994839	0.999854
35	0.15	0.46875	0.996945	0.990304	0.999782	0.996273	0.98816	0.999636
36	0.2	0.46875	0.994379	0.982235	0.999527	0.993341	0.979188	0.999417
37	0.25	0.46875	0.990836	0.971427	0.999272	0.989492	0.967586	0.99909
38	0.3	0.46875	0.986376	0.958347	0.998944	0.98436	0.952848	0.998689
39	0.35	0.46875	0.980389	0.941832	0.998507	0.978128	0.935937	0.998179
40	0.4	0.46875	0.972507	0.921338	0.997925	0.969697	0.914629	0.99756
41	0.45	0.46875	0.963099	0.89863	0.997306	0.959311	0.890185	0.996869
44	0.6	0.46875	0.916422	0.808347	0.994575	0.906525	0.79343	0.99381
45	0.65	0.46875	0.888624	0.767507	0.993264	0.875794	0.75137	0.992281
46	0.7	0.46875	0.855327	0.726786	0.991917	0.836083	0.707572	0.990606

Sr. No.	a/H	L_1/L	V-shaped cracked cases: Relative natural frequency			U-shaped cracked cases: Relative natural frequency		
			f_{r1}	f_{r2}	f_{r3}	f_{r1}	f_{r2}	f_{r3}
47	0.75	0.46875	0.804741	0.678444	0.990023	0.780242	0.659964	0.988494
48	0.8	0.46875	0.732832	0.62761	0.987766	0.702346	0.611195	0.985982
49	0.05	0.625	0.999878	0.999206	0.999745	0.999878	0.998908	0.999636
50	0.1	0.625	0.999633	0.996328	0.998835	0.999572	0.995236	0.998507
51	0.15	0.625	0.999145	0.991207	0.997342	0.998961	0.989162	0.996759
52	0.2	0.625	0.99835	0.983674	0.995157	0.998106	0.980717	0.994465
53	0.25	0.625	0.997312	0.973869	0.992609	0.996945	0.969889	0.991589
54	0.3	0.625	0.995907	0.960967	0.989331	0.995479	0.956123	0.988166
55	0.35	0.625	0.994257	0.946149	0.985909	0.993463	0.938845	0.984307
56	0.4	0.625	0.991813	0.925715	0.981576	0.990958	0.918162	0.979901
57	0.45	0.625	0.988697	0.901737	0.976733	0.987659	0.893321	0.974913
58	0.5	0.625	0.985093	0.875506	0.972036	0.983382	0.86318	0.969342
59	0.55	0.625	0.979778	0.841048	0.96581	0.977334	0.825715	0.963079
62	0.7	0.625	0.949108	0.699226	0.943417	0.941227	0.67369	0.939084
63	0.75	0.625	0.927114	0.634835	0.933513	0.915078	0.607037	0.928743
64	0.8	0.625	0.89009	0.560341	0.922335	0.872434	0.534845	0.917128
65	0.05	0.78125	1	0.999802	0.999745	1	0.999702	0.999563
66	0.1	0.78125	1	0.999008	0.998726	1	0.998611	0.998325
67	0.15	0.78125	0.999939	0.997519	0.997014	1	0.996923	0.996286
68	0.2	0.78125	0.999878	0.995435	0.994502	1	0.994541	0.993664
69	0.25	0.78125	0.999817	0.992447	0.991516	0.999878	0.991137	0.990424
70	0.3	0.78125	0.999633	0.988547	0.987802	0.999756	0.98687	0.986419
71	0.35	0.78125	0.99945	0.984021	0.983797	0.999572	0.981322	0.981867
72	0.4	0.78125	0.999084	0.976509	0.978335	0.999267	0.973809	0.976296
73	0.45	0.78125	0.998717	0.967954	0.9724	0.9989	0.964768	0.97007
74	0.5	0.78125	0.998228	0.957265	0.965955	0.99835	0.952044	0.963006
75	0.55	0.78125	0.997495	0.941653	0.957472	0.997556	0.935788	0.954632
76	0.6	0.78125	0.996579	0.923035	0.948988	0.996457	0.913319	0.945383
77	0.65	0.78125	0.995112	0.895276	0.938683	0.994868	0.881937	0.933877
80	0.8	0.78125	0.983504	0.720058	0.894334	0.980694	0.683932	0.886069
81	0.05	0.9375	1.000061	1.000099	1	1.000061	1.000099	1
82	0.1	0.9375	1.000122	1.000099	0.999964	1.000244	1.000198	1
83	0.15	0.9375	1.000183	1.000099	0.999964	1.000367	1.000198	0.999964
84	0.2	0.9375	1.000244	1.000099	0.999854	1.000428	1.000198	0.999891
85	0.25	0.9375	1.000305	1.000099	0.999782	1.000611	1.000298	0.999782
86	0.3	0.9375	1.000367	1.000099	0.999636	1.000733	1.000298	0.999636
87	0.35	0.9375	1.000428	1.000099	0.99949	1.000855	1.000298	0.999454
88	0.4	0.9375	1.000489	1	0.999235	1.000978	1.000298	0.999235
89	0.45	0.9375	1.00055	0.999901	0.99898	1.0011	1.000198	0.998944
90	0.5	0.9375	1.000611	0.999802	0.998616	1.001222	1.000099	0.998544
91	0.55	0.9375	1.000672	0.999603	0.998179	1.001344	0.999901	0.998107
92	0.6	0.9375	1.000733	0.999405	0.997706	1.001466	0.999603	0.997524
93	0.65	0.9375	1.000794	0.998908	0.996978	1.001588	0.999206	0.996723
94	0.7	0.9375	1.000794	0.998313	0.996213	1.001711	0.998511	0.995776
95	0.75	0.9375	1.000855	0.99742	0.995084	1.001833	0.99742	0.994465
96	0.8	0.9375	1.000855	0.995534	0.993592	1.001894	0.995137	0.992609

Table 2. Parameter Set in Classifier experimentation

Classifier	Variant	Maximum Number of Splits	Split Criteria	-
Decision Tree	Fine Tree	100	Gini's diversity index	
	Medium Tree	20		
	Coarse Tree	4		
Discriminant Analysis	Variant	Discriminant Type	Amount of Regularization	Fill Coefficients (Property flag)

Classifier	Variant	Maximum Number of Splits	Split Criteria	-
RJAV	Linear Discriminant Analysis (LDA)	Linear	0	Off
	Quadratic Discriminant Analysis (QDA)	Quadratic	1	Off
Support Vector Machine	Variant	Kernel Function	Polynomial Order	Mapping and Kernel Scale
	Linear SVM	Linear	-	One-Vs-One and Auto
	Quadratic SVM	Polynomial	2	One-Vs-One and Auto
	Cubic SVM	Polynomial	3	One-Vs-One and Auto
K-nearest neighbor classifier	Variant Cosine KNN	Distance Cosine	Exponent -	Distance Weight Equal
	Cubic KNN	Minkowski	3	Equal
	Weighted KNN	Euclidean	-	Squared Inverse
Ensemble Classifier	Variant	Method	Number of Learning Cycles	Learners
	Boosted Trees	Adaboost M1	30	Template
	Bagged Trees	Bag	30	Template
	Subspace Discriminant	Subspace	30	Discriminant
	Subspace KNN	Subspace	30	K NN
	RUSBoosted Trees	RUSBoost	30	Template
Artificial Neural Network	Variant	Number of Nodes per layer	Number of Epochs	Learning Rate
	Feed forward back propagation	Input- 3 Hidden- 8 Output -1	1000	0.1

Table 3. Comparison of various classifier performances for V-shaped cracked cases.

Sr. No.	Training Algorithm (K=5)		Accuracy (%)	Accuracy (%)
			L_1/L	a/H
1	Decision Tree Algorithm	Fine Tree	64.4	14.9
2		Medium Tree	64.4	14.9
3		Coarse Tree	48.3	10.3
4	Discriminant Analysis Algorithm	Linear Discriminant Analysis	58.6	14.9
5		Quadratic Discriminant Analysis	94.3	11.5
6	Support Vector Machines	Linear SVM	63.2	23
7		Quadratic SVM	66.7	17.2
8		Cubic SVM	80.5	23
9		Fine Gaussian SVM	69	18.4
10		Medium Gaussian SVM	63.2	26.4
11		Coarse Gaussian SVM	47.1	12.6
12	Nearest Neighbor Algorithm	Fine KNN	77	9.2
13		Medium KNN	56.3	9.2
14		Coarse KNN	18.4	5.7
15		Cosine KNN	64.4	11.6
16		Cubic KNN	62.1	10.3
17		Weighted KNN	77	10.3
18	Ensemble Classifier	Boosted Trees	18.4	13.8
19		Bagged Trees	78.2	16.1
20		Subspace Discriminant	56.3	12.6
21		Subspace KNN	54	23
22		RUSBoosted Trees	40.2	18.4
23	Artificial Neural Network	Feed Forward Back Propagation	99.977	100

**Table 4.** Comparison of various classifier performances for U-shaped cracked cases.

Sr. No.	Training Algorithm (K=5)		Accuracy (%)	Accuracy (%)
			L_1/L	a/H
1	Decision Tree Algorithm	Fine Tree	57.5	18.4
2		Medium Tree	57.5	18.4
3		Coarse Tree	47.1	9.2
4	Discriminant Analysis Algorithm	Linear Discriminant Analysis	64.4	13.8
5		Quadratic Discriminant Analysis	90.8	10.3
6	Support Vector Machines	Linear SVM	70.1	24.1
7		Quadratic SVM	71.3	24.1
8		Cubic SVM	82.8	17.2
9		Fine Gaussian SVM	69	20.7
10		Medium Gaussian SVM	66.7	27.6
11		Coarse Gaussian SVM	48.3	18.4
12	Nearest Neighbor Algorithm	Fine KNN	80.5	11.5
13		Medium KNN	66.7	9.2
14		Coarse KNN	18.4	5.7
15		Cosine KNN	66.7	9.2
16		Cubic KNN	66.7	10.3
17		Weighted KNN	78.2	11.5
18	Ensemble Classifier	Boosted Trees	18.4	18.4
19		Bagged Trees	80.5	17.2
20		Subspace Discriminant	59.8	13.8
21		Subspace KNN	49.4	17.2
22		RUSBoosted Trees	37.9	17.2
23	Artificial Neural Network	Feed Forward Back Propagation	99.1	99.95

Table 5. Comparison between Actual and predicted ANN outputs of V-shaped and U-shaped cracked cases.

Predicted ANN results for V-shaped cracked cases								
Sr. No.	f_{r1}	f_{r2}	f_{r3}	a/H	a/H	% error	L_1/L	L_1/L	% error
				Actual	ANN		Actual	ANN	
24	0.933651	0.976141	0.979064	0.4	0.46422	**-13.83**	0.3125	0.31368	**-0.38**
25	0.912268	0.968767	0.973857	0.45	0.43949	**2.39**	0.3125	0.31363	**-0.36**
42	0.945748	0.861473	0.996031	0.5	0.55613	**-10.09**	0.46875	0.54979	**-17.29**
43	0.928886	0.829784	0.995012	0.55	0.56409	**-2.50**	0.46875	0.47352	**-1.02**
60	0.969514	0.783704	0.956052	0.60	0.71198	**-15.73**	0.625	0.62634	**-0.21**
61	0.957967	0.732205	0.947932	0.65	0.78834	**-17.55**	0.625	0.62731	**-0.37**
78	0.992363	0.837197	0.920514	0.70	0.74562	**-6.12**	0.78125	0.78647	**-0.67**
79	0.988453	0.776717	0.905112	0.75	0.79541	**-5.71**	0.78125	0.89982	**-15.18**
Predicted ANN results for U-shaped cracked cases								
Sr. No.	f_{r1}	f_{r2}	f_{r3}	a/H	a/H	% error	L_1/L	L_1/L	% error
				Actual	ANN		Actual	ANN	
24	0.939638	0.978116	0.980629	0.4	0.39789	**0.53**	0.3125	0.30495	**2.42**
25	0.919416	0.9711	0.975568	0.45	0.44714	**0.64**	0.3125	0.29721	**4.89**
42	0.951796	0.873472	0.996614	0.5	0.5026	**-0.52**	0.46875	0.4873	**-3.96**
43	0.935239	0.840919	0.995594	0.55	0.55417	**-0.76**	0.46875	0.48819	**-4.15**
60	0.972996	0.802134	0.958964	0.60	0.6038	**-0.63**	0.625	0.63822	**-2.12**
61	0.962304	0.750586	0.951573	0.65	0.65777	**-1.20**	0.625	0.63772	**-2.04**
78	0.993157	0.859726	0.928343	0.70	0.6921	**1.13**	0.78125	0.77927	**0.25**
79	0.989858	0.804913	0.912431	0.75	0.73425	**2.10**	0.78125	0.77935	**0.24**

Table 6. Comparison between Actual and predicted correlation model results of V-shaped and U-shaped cracked cases.

Predicted correlation model results for V-shaped cracked cases								
Sr. No.	f_{r1}	f_{r2}	*a/H*	*a/H*	% error	L_1/L	L_1/L	% error
			Actual	Correlation model		Actual	Correlation model	
24	0.933651	0.976141	0.4	0.3885	**2.88**	0.3125	0.2702	**13.54**
25	0.912268	0.968767	0.45	0.4052	**9.96**	0.3125	0.2862	**8.42**
42	0.945748	0.861473	0.5	0.5324	**-6.48**	0.46875	0.4969	**-6.01**
43	0.928886	0.829784	0.55	0.5852	**-6.40**	0.46875	0.5055	**-7.84**
60	0.969514	0.783704	0.60	0.6798	**-13.30**	0.625	0.7054	**-12.86**
61	0.957967	0.732205	0.65	0.8144	**-25.29**	0.625	0.7929	**-26.86**
78	0.992363	0.837197	0.70	0.7598	**-8.54**	0.78125	0.8493	**-8.71**
79	0.988453	0.776717	0.75	0.7141	**4.79**	0.78125	0.7993	**-2.31**
Predicted correlation model results for U-shaped cracked cases								
Sr. No.	f_{r1}	f_{r2}	*a/H*	*a/H*	% error	L_1/L	L_1/L	% error
			Actual	Correlation model		Actual	Correlation model	
24	0.939638	0.978116	0.4	0.3562	**10.95**	0.3125	0.2737	**12.42**
25	0.919416	0.9711	0.45	0.4038	**10.27**	0.3125	0.2711	**13.25**
42	0.951796	0.873472	0.5	0.4903	**1.94**	0.46875	0.4954	**-5.69**
43	0.935239	0.840919	0.55	0.5461	**0.71**	0.46875	0.5042	**-7.56**
60	0.972996	0.802134	0.60	0.6151	**-2.52**	0.625	0.6778	**-8.45**
61	0.962304	0.750586	0.65	0.7207	**-10.88**	0.625	0.7377	**-18.03**
78	0.993157	0.859726	0.70	0.5257	**24.90**	0.78125	0.6904	**11.63**
79	0.989858	0.804913	0.75	0.6935	**7.53**	0.78125	0.7997	**-2.36**
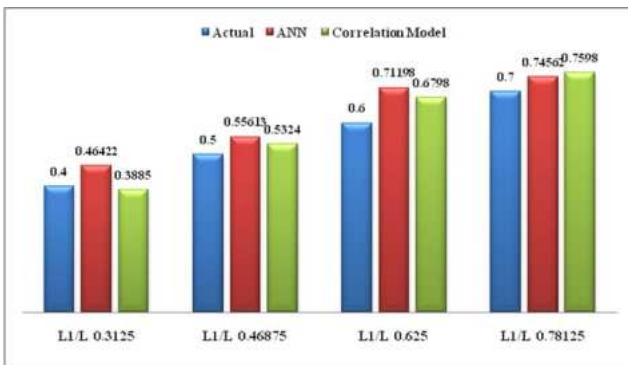
Figure 10. Predicted crack depth ratios using ANN and Correlation model at different crack location ratios.
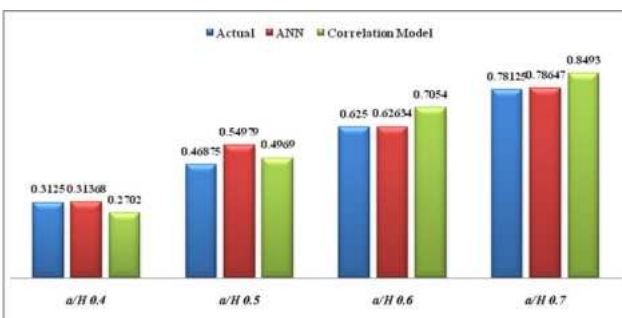
Figure 11. Predicted crack locations ratio using ANN and Correlation model at different crack depth ratio.

It is also apparent that, for the identical configurations, the natural frequency decrease of a U-shaped cracked beam compared to an un-cracked beam is considerably larger than that of a V-shaped cracked beam. As a result, it is clear that as the difference in natural frequency between the un-cracked and cracked beams grows; the ANN model can more accurately predict the crack characteristics. Similarly, when comparing the findings of Table 6, it is evident that the correlation model comparatively performed well in predicting the crack depths and positions in V-shaped cracked cases of beams. As a result, the correlation model can better predict the occurrence of V-shaped cracks than U-shaped cracks in beams for the same configurations.

8. CONCLUSIONS

The presence of crack changes the stiffness and vibration response of the beam. The crack development in a beam causes it to fail suddenly and without warning. Structural health monitoring is required to avoid hazards, damages, and breakdowns. In this research study, the natural frequencies of the un-cracked and cracked beams were evaluated using numerical method. Afterward, the correlation model

is developed for V-shaped and U-shaped cracked cases to predict the crack parameters in the beam. Furthermore, Machine learning approaches, i.e., artificial neural network (ANN), were utilized for the crack detection in beams. The following conclusions can be drawn from this research:

1. The beams' crack locations and depths can be accurately predicted using the correlation model, ANN, and the Discriminant Analysis Algorithm.

2. The correlation model predicts crack parameters more accurately in V-shaped cracked beams than U-shaped cracked beams for the same configurations.

3. According to the findings of this study, the ANN model is more accurate than other Machine Learning models at predicting the crack locations and crack depths in beams.

4. For the identical configurations, structural health monitoring utilizing a machine learning approach for U-shaped cracked cases is comparatively more successful than V-shaped cracked instances.

9. FUTURE SCOPE

A neural controller can be made and installed in structures using the ANN algorithm and can be programmed according to it, predicting the damages and providing prior warning and indication.

REFERENCES

[1] Vakil-Baghmisheh, M.T., Peimani, M., Sadeghi, M.H., & Ettefagh, M.M., *Crack detection in beam-like structures using genetic algorithms,* Applied soft computing, 8(2), 2008, pp. 1150–1160.

[2] Khatir, A., Tehami, M., Khatir, S., & Wahab, M.A., *Multiple damage detection and localization in beam-like and complex structures using co-ordinate modal assurance criterion combined with firefly and genetic algorithms,* Journal of Vibroengineering, 18(8), 2016, pp. 5063–5073.

[3] Sutar, M.K., Pattnaik, S., & Rana, J., *Neural Based Controller for Smart Detection of Crack in Cracked Cantilever Beam,* Materials Today: Proceedings, 2(4-5), 2015, pp. 2648–2653.

[4] Nasiri, S., Khosravani, M.R., & Weinberg, K., Fracture *mechanics and mechanical fault detection by artificial intelligence methods:* A review, Engineering Failure Analysis, 81, 2017, pp. 270–293.

[5] Teidj, S., Khamlichi, A., & Driouach, A., *Identification of beam cracks by solution of an inverse problem,* Procedia Technology, 22, 2016, pp. 86–93.

[6] Thatoi, D.N., Choudhury, S., Das, H.C., Jena, P.K., & Agrawal, G., CFBP Network–A Technique for Crack Detection, Procedia materials science, 6, 2014, pp. 10–17.

[7] Pan, D.G., Lei, S.S., & Wu, S.C., Two-*stage damage detection method using the artificial neural networks and genetic algorithms,* In International Conference on Information Computing and Applications, 2010, pp. 325–332.

[8] Orhan, S., Luy, M., Dirikolu, M.H., & Zorlu, G.M., The *effect of crack geometry on the non-destructive fault detection in a composite beam,* International Journal of Acoustics and Vibration, 21(3), 2016, pp. 271–273.

[9] ANSYS Release 12.1, ANSYS Inc.

[10] Khalkar, V., & Ramachandran, S., *The effect of crack geometry on non-destructive fault detection of EN 8 and EN 47 cracked cantilever beam,* Journal of Noise and Vibration Worldwide, 50, 2019, pp. 92–100.

[11] Khalkar, V., & Ramachandran, S., *The effect of crack geometry on stiffness of spring steel cantilever beam,* Journal of low frequency noise, vibration and active control, 37, 2018, pp. 762–774.

[12] Margaret, H.D., *Data Mining Introductory and Advanced Topics,* Pearson Education, 2008, India.

[13] Christianini, N., & Shawe-Taylor, J.C., *An Introduction to Support Vector Machines and Other Kernel-based Learning Methods,* Cambridge, U.K. Cambridge University, Press, 2000.

[14] Ian, H.W., Eibe, F, & Mark, A.H., *Data Mining,* 3rd Edition Morgan Kaufmann publisher, 2011

[15] Elaine, R., & Kevin, K, *Artificial Intelligence,* Third Edition, Tata McGraw-Hill Education Pvt. Ltd., 2008

[16] Fawcett, T., *An Introduction to ROC Analysis,* Pattern Recognition, 2006.

[17] Gillich, N., Tifisi, C., Sacarea, C., Rusu, C.V., Gillich, G., Praisach, Z., & Ardeljan, M., *Beam Damage Assessment Using Natural Frequency Shift and Machine Learning, Sensors,* 22, 2022, pp. 2–23.

[18] Tufisi, C., Gillich, N., Ardeljan, M., Paun, R.L., Rusu, V., & Gillich, G., *A Cost Function to Assess Cracks in Simply Supported Beams with Artificial Intelligence,* Romanian Journal of Acoustics and Vibration, 18(1), 2021, pp. 46–52.

[19] Tufisi, C., Rusu, C.V., Gillich, N., Pop, M.V., Hamat, C.O., Sacarea, C., & Gillich, N. (2022). *Determining the Severity of Open and Closed Cracks Using the Strain Energy Loss and the Hill-Climbing Method,* Applied Science, 12, 2022, pp. 2–18.

[20] Tufisi, C., Rusu, V., & Gillich, G., *Locating Transverse Cracks in Prismatic Beams Using Random Forest Method and the Frequency Drop,* Romanian Journal of Acoustics and Vibration, 18(2), 2021, pp. 119–125.

[21] Onchis, D.M., & Gillich, G., *Stable and explainable deep learning damage prediction for prismatic cantilever steel beam,* Computers in Industry, 125, 2021, pp. 1–8.

[22] Khalkar, V. Kumbhar, S.G., Hariharsakhtisudhan, P., Moshi, A.M.M., Jadhav, S.D., Kumbhar, N., Oak, P., & Joshi, P.S., *Some Studies on Verifying the Applicability of Free Vibration-based Modes Shapes Method to Rectangular Shaped Cracks in a Cantilever Beam,* U.Porto Journal of Engineering, 8 (2), 2022, pp. 82-94.

[23] Khalkar, V. Kumbhar, S.G., Logesh, K., Hariharsakhtisudhan, P., Jadhav, S.D., Danawade, B.A., Gharat, S.H., Jugulkar, L.M., Borade, J.G.., Experimental and numerical investigation of a cracked cantilever beam for damping loss factor to access its applicability in the crack detection, U.Porto Journal of Engineering, 8 (2), 2022, pp. 169-186.

RESEARCH ARTICLE

Quasi-static compression behavior and crashworthiness of GLARE laminate conical frustum with progressive circular and square cut-outs

K. Logesh[1] | P. Hariharasakthisudhan[2] | Renjin J. Bright[3] |
Sathish Kannan[4] | V. Khalkar[5] | N. Sundaraiah[1]

[1]Department of Mechanical Engineering, Vel Tech Rangarajan Dr. Sagunthala R&D Institute of Science and Technology, Chennai, Tamil Nadu, India

[2]Department of Mechanical Engineering, Sri Krishna College of Technology, Coimbatore, India

[3]Department of Production Engineering, PSG College of Technology, Coimbatore, India

[4]Department of Mechanical Engineering, College of Engineering, American University of Sharjah, Sharjah, United Arab Emirates

[5]Department of Mechanical Engineering, Gharda Institute of Technology, Ratnagiri, India

Correspondence
P. Hariharasakthisudhan, Department of Mechanical Engineering, Sri Krishna College of Technology, Kovaipudur, Coimbatore, Tamil Nadu, India.
Email: harimeed2012@gmail.com

Abstract

The design of structures using advanced composite materials such as fiber metal laminate requires an in-depth understanding of their deformation behavior and response to the discontinuities in the structures. In the present study, a GLARE kind of fiber metal laminate in 2/1 configuration was fabricated in the form of conical frustum. Three cut-outs of two different shapes such as circular and square were intentionally made at the center of the frustum at an angular distance of 120°. The quasi-static compression test was conducted to determine the crashworthiness characteristics of laminate frustums with cut-out and the results were compared with perfect frustum. The study showed that the laminate with cut-out undergone for inward buckling near the discontinuities. Apart from that, the delamination and outward buckling were noted in the edges of the cut-outs. The energy absorption of laminate frustum with circular cut-outs was observed to be better than square cut-outs. The performance of laminate frustums with cut-outs was ranked using Technique for Order Preference by Similarity to an Ideal Solution technique. A finite element analysis was carried out to simulate the deformation behavior of laminate frustum with cut-outs and the numerical results of deformation mode closely represented the experimental results.

KEYWORDS
damage tolerance, forming, laminate mechanics, laminates, mechanical testing, statistical methods

1 | INTRODUCTION

In view of reducing the carbon footprint and improving the fuel efficiency, conventional metals used in the structural applications of automobile, and aircraft industries are replaced by the lightweight composite materials. Apart from providing high specific strength, these materials need to impart considerable damage resistance under a crash impact.[1] The advanced class of composite materials, namely the fiber metal laminates (FML), are suitable replacement for structural applications of aerospace and automobile due to their superior fatigue resistance, fracture toughness, and damage tolerance.[2–9] However, the safety concerns in such sectors, regarding the utilization of these materials for constructing aerospace and automobile structural components, necessitate the importance of conducting crashworthiness tests.

A Novel Reconfigurable Coordinated Control
for Autonomous Low Voltage DC Microgrid

Shrishell Muchande, Sushil Thale

Abstract – *DC microgrids with a small electrical network of locally available energy resources and distributed loads are becoming popular in real-life applications, especially in remote areas and in some specific urban applications. This, in turn demands a serious insight into the control and reliability enhancement of such systems so that the availability of secure and safe energy can be assured to the users. But the integration of intermittent renewable energy resources in dc microgrids lead to a serious concern regarding the stability of the microgrid bus voltage under continuous change in available source power and the loading conditions. While the microgrid management is still a challenge under steady state operating conditions, it becomes much complex under some emergency events like faults, failure of controllers/sources and overloads etc. This paper proposes a novel reconfigurable coordinated control architecture for a Low Voltage DC (LVDC) microgrid comprises of solar photovoltaic, fuel cell based renewable energy sources supported Energy Storage System (ESS) formed with battery and ultra-capacitor banks. The reliability of the system is ensured in the proposed reconfigurable coordinated control with three layered hierarchy viz. Emergency control layer sandwiched between the supervisory and local control layers. The proposed control strategy is implemented through a new Microgrid Bus Controller (MGBC) strengthened by an "emergency" control layer which handles the responsibility in emergency conditions to coordinate the energy sources, loads and controllers. The MGBC facilitates the fault identification and isolation to ensure the reliable operation of the healthy microgrid sections and speedy fault recovery. The MGBC is dedicated for observing the bus parameters and identify the fault location by monitoring the bus branching currents. Some of the key hardware and simulations results validating the proposed architecture along with the details of the control implementation are presented in this paper. **Copyright © 2023 Praise Worthy Prize S.r.l. - All rights reserved.**

Keywords: *Autonomous Microgrid, Coordinated Control, DC Microgrid, Reconfigurable Control*

Nomenclature

d_{CMC}	Duty cycle for converter in CMC mode
d_{bat_chg}	Duty cycle for battery converter in charging mode
d_{MPPT}	Duty cycle for converter in MPPT mode
d_{UC_chg}	Duty cycle for UC charging mode
d_{VMC}	Duty cycle for converter in VMC mode
G_I	Transfer Function for current controller
G_V	Transfer Function for voltage controller
I_{bat}^*	Reference value of battery current
I_{bat_chg}	Charging current required by Battery to track V_{bat}^*
$I_{bat\_chg}^*$	Reference value of the battery current in charging mode
I_{bat}^{max}	Maximum limit of battery current
I_{bat}^{min}	Minimum limit of battery current
I_{CL}	Critical load current
I_{flti}	Fault current in MG bus
I_L	MG bus load current
I_{L_fc}	Inductor output current value of Fuel Cell converter
$I_{L\_fc}^*$	Reference current value of the Fuel Cell converter inductor
I_{L_PV}	Inductor output current value of PV converter
$I_{L\_PV}^*$	Reference value of the PV converter inductor current
I_{NCL}	Non-critical load current
I_{o_fc}	Fuel Cell converter output current
I_{o_bat}	Battery converter output current
I_{o_PV}	PV converter output current
I_{o_uc}	UC Cell converter output current
I_{PV}	Output current of Solar PV
I_{uc}	UC converter output current
I_{uc}^*	Reference value of UC current
I_{uc_chg}	Charging current required by UC
$I_{uc\_chg}^*$	Reference value of the UC charging current
I_{uc}^{max}	Maximum limit of UC current
I_{uc}^{min}	Minimum limit of UC current
k_p	Proportional gain
k_i	Integration gain
P_{BAT}	Powers supplied by Battery
P_{FC}	Power feeding from Fuel Cell

P_{PV}	Powers supplied by solar PV
P_L	Load power demand
P_{UC}	Power supplied by Ultra-capacitor
PWM	Pulse Width Modulation
V_{bat}^*	Reference value of battery voltage
V_{MPPT}^*	Reference value of MPPT output voltage
V_{mg}	MG bus voltage
V_{o_bat}	Battery converter output voltage
V_{o_fc}	Fuel Cell converter output voltage
$V_{o\_fc}^*$	Reference value of Fuel Cell voltage
V_{o_PV}	PV converter output voltage
V_{o_uc}	UC converter output current
V_{PV}	Output voltage of PV
V_{uc_ref}	UC Converter Reference voltage value
τ_{CI}	System Time constant
ω_s	Switching frequency
ω_{CI}	Gain-crossover frequency
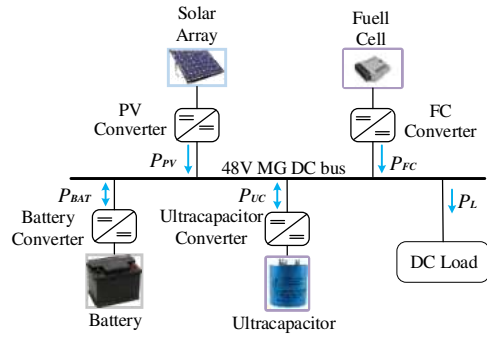
I. Introduction

Microgrid (MG) facilitates integrating multiple small-capacity Renewable Energy Sources (RESs) with an aggregated electrical load. It serves more like a grid supply, especially where conventional grid infrastructure may not be reliable or available. The Energy Storage Systems (ESSs) are also incorporated in MG power architecture to ensure the reliability and stability of the microgrid under all operating conditions. These RESs and ESSs are interfaced to Microgrid's common bus through Power Conditioning Units (PCUs). The microgrids are classified into DC microgrids, AC microgrids and Hybrid AC-DC microgrids [1]-[4]. In the initial phase, the research in microgrid domain was focused more on AC microgrids which in later years got concentrated on DC and Hybrid microgrids. The DC microgrids possess significant advantages by offering simplified PCUs with increased efficiency while eliminating the need for the complex synchronization process. Recently, increased interest is witnessed in a Low Voltage DC (LVDC) autonomous microgrid to replace the power grid in applications like office building, telecom power systems, spacecraft etc., and now, it is commonly used in the residential applications also. Fig. 1 shows the power architecture of an autonomous LVDC microgrid. It consists of various microgrid sources, ESSs and power electronic converters considered for the proposed study. However, there are numerous challenges associated with control as well as protection of the DC microgrids. Due to the significantly different dynamic behavior of RESs and unpredictable loads, uncertainties are happening in microgrid operation.

This results into poor power quality such as voltage dips and fluctuations. On the other hand, for improved reliability, microgrid architecture comprising different types of RESs and energy storage units demands adoption of effective control methods [5]. Taheruzzaman [6] demonstrated the hidden potential to share power amongst households within the same DC-MG in Bangladesh.

Fig. 1. Schematic of LVDC Autonomous Microgrid under study

Rani et al. [7] presented an approach for controlling the power between DC source and utility grid, and vice versa. The modelling and implementation of grid-following mode and grid-forming mode of converters is showcased. This paper presents the particulars of the research carried out with an autonomous LVDC microgrid shown in Fig. 1 to address various power sharing and protections issues under normal and abnormal operating conditions. A laboratory prototype of autonomous LVDC MG under study was developed to operate at 48V and net rated power capacity of 4 kW.

The details of the research work carried out are given in the following sections. A review of existing control and protection schemes for microgrid is reported in Section II. The proposed control and power architecture of the developed prototype is presented in Section III.

The key simulation and experimental results captured under some of the specific emergency conditions of proposed reconfigurable control scheme are explained in Section IV. Section V illustrates the conclusion based on the research work carried out.

II. DC Microgrid Control and Protection

The existing literature illustrated various microgrid control strategies generally classified into decentralized, centralized, and hierarchical control [8]-[12], [26]-[28].

The hierarchical control shows the more reliable and robust performance over the difficulties associated with decentralized and centralized control. Sandeep et al. [8] proposed a procedure of reduced order model to analyze the stability of droop controlled low-voltage DC MG.

Mohsen et al. [9] presented comprehensive control scheme for multi-bus DC MG to share the dc and oscillatory components of the load current among the DG units based on their rated power. Qianwen Xu et al. [10] proposed a robust droop-based controller for decentralized power sharing in DC MG to enhance the robustness against the uncertainties happening in system parameters. A nonlinear disturbance observer-based droop scheme is used for decentralized power sharing in DC MG considering large-signal stability. Jin et al. [11] proposed the coordination control strategy among multiple sources and energy storage elements implemented through three level hierarchical control for

reliable and economical operation of autonomous DC MG. Zhao et al. [12] proposed coordinated control strategy including five hierarchical levels based on the voltage variation range in multi-bus-based DC MG system. Muchande et al. [13] proposed Hierarchical Control of a Low Voltage DC Microgrid with Coordinated Power Management Strategies. Thale et al. [2] proposed AC MG and its reliability and sustainability are ensured through a 4-level hierarchical control under all possible operating conditions. The optimal or suboptimal operation in emergency is handled by reconfigurable control and power network of microgrid.

The main aim of the microgrid is to bring in the decentralized generation to support the existing main grid. Microgrid can operate either standalone or grid connected. In grid connected microgrid operation, while power interchanges with the existing distribution network faces various challenges. Jamaica-Obregon et al. [14] proposed a detailed formulation to operate microgrids with photovoltaic based renewable energy systems and storage. The system protection is an important aspect of microgrids. Especially in the DC MG, the protection is more challenging than AC MG due to no zero crossing in dc currents. The emergency conditions like faults, failure of controllers/ sources and overloads may occur in microgrid directly impacting its reliability. The electrical fault conditions and their handling are significantly different from other emergency conditions. The faults can be classified as low impedance and high impedance faults. A low impedance fault means large deep in bus voltage due to higher fault current and complete system may collapse. The high impedance fault results in lower fault current. It is challenging task to identify the fault emergency conditions from normal and abnormal conditions in DC MG. However, the emergency conditions may demand major changes in power management strategy, control, and protection schemes for DC MG. The main objective of the protection scheme is to isolate the smallest portion of the system in minimum time and continue the optimal or sub optimal operation of microgrid. Various microgrid protection schemes have been proposed that provide fast and effective methods for detection, isolation of faulty part of the system. Cairoli et al. [3] developed a fast and effective method for detecting and isolating the faults without communication between power supply converters and bus segmenting contactors for Medium Voltage DC (MVDC) microgrid. This method relies on rapid coordination between these active elements to limit currents and isolate the fault. Subramaniam et al. [4] proposed the cost-effective protection system for faster detection and selective isolation of high impedance faults. The system restoration is ensured through proper coordination control between source converters and bus sectionalized devices. This proposed scheme is based on local information to provide the robust and localized protection scheme for high impedance fault. Daniel et al. [15] presented a low-voltage dc microgrid protection system. The influences of selected protection devices and grounding method on LVDC MG are investigated and verified through simulation results. Yuan et al. [16] presented the communication based differential protection as a main scheme with solid-state electronic relays and overcurrent protection of a MVDC MG.

Furthermore, the bi-directional power flow protection for the sources and the load are ensured by communication based directional overcurrent protective relays. In a high impedance fault, it is very difficult to distinguishing the fault current in contrast to the normal current. Madingou et al. [17] designed a cost-effective protection system for detecting, isolating, and locating of high impedance ground faults using Digital Signal Processing (DSP) based control unit. The DC ring bus is divided into bus segment and monitors the bus current with current rise-based algorithm. Wang et al. [18] developed mathematical model and proposed a new fault let-through energy-based DC fault location working strategy to facilitate post-fault network maintenance.

Prince et al. [19] proposed effective protection schemes based on a complex power concept using Fast Fourier Transform for fast short-circuit fault detection and isolation in a DC microgrid. Senapati et al. [20] presented a LVDC microgrid protection system using the knowledge of the existing AC power systems. Zubieta et al. [21] presented the protection scheme for power distribution systems based on a DC microgrid for residential applications. The proposed scheme was based on use of the energy storage resources located at the consumers to decouple the load and local generation transients from the power demanded by or supplied to the DC distribution line. Ali et al. [22] presented the state-of-the-art issues concerning the fault management of DC microgrids. The energy management is also an important task for optimal utilization of renewable energy specially in standalone applications. Therefore, a lot of extensive research activities are carried out to address the energy management issues in microgrid populated with renewable energy sources. Kassir et al. [23] proposed a new Energy Management System (EMS) based approach to standalone microgrid comprised of a Solar Photovoltaic (SPV) unit as a main source, a hydrogen Fuel Cell (FC) as a standby source and a Hybrid battery-Based Energy Storage System (BESS) for residential application. This approach is used not only to distribute the power between renewable energy sources, the FC, the Battery and the ultra-capacitor but also regulating the battery State of Charge (SoC) between two desirable limits, while minimizing the cost of battery usage and hydrogen consumption. This is achieved by a gain controlled low-pass filter where gain value is adapted online in order to increase flexibility of source's use. In a microgrid, the DC bus voltage is always changes due to the inherent behavior of distributed energy sources which depends on geographical and environmental conditions.

Krishna et al. [24] proposed voltage droop control strategy to keep the DC bus link voltage at a constant value for renewable energy sources for energy management. Long et al. [25] proposed load shedding in

islanded mode microgrids with consideration to improve the voltage quality of the isolated microgrid system. As described above, the existing literature include details of research work related to microgrid control and the fault management. However, the current research still does not provide sufficient insights into coordination in control and protection operations with enhanced reliability under steady-state and emergency conditions. Hence, to address this issue, this paper proposes a novel reconfigurable coordinated control and power architecture for an autonomous LVDC MG. The simulation and experimental results presented confirms the validation of the proposed control. The main contribution of this research work is the proposed reconfigurable coordinated control based on monitoring the bus current magnitudes at each bus segment to enable effective implementation of the coordination and control algorithm within the microgrid. This facilitates the microgrid to continue to operate under all emergency conditions with fault identification, isolation, and restoration. The proposed reconfigurable coordinated control strategy includes three hierarchical levels of control. Based on the hierarchical control inputs, the coordination decisions and local level controls are implemented in different control layers.

III. Proposed Control Architecture and System Description

The proposed reconfigurable coordinated control strategy includes three hierarchical control levels shown in Fig. 2. The Primary control is a local level control which covers the source optimization algorithms like MPPT, source life cycle management and the power control.

The operating modes in Primary control are Voltage Mode Control (VMC) and Current Mode Control (CMC). Depending on the role assigned by the Supervisory control, it either controls the bus voltage or current supplied by the source. Each source is equipped with at least one local controller which is coordinated to ensure reliable operation of the microgrid. The Secondary control is implemented through two different layers named Coordination Control Layer (CCL) and Emergency Control Layer (ECL) located in the supervisory controller.
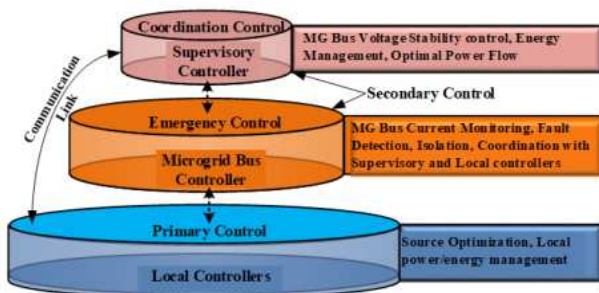
The system level functionalities are implemented through Supervisory controller supported with a Controller Area Network (CAN) communication link.

The local controllers are dependent on reference generated by secondary control. In secondary control, the microgrid bus voltage maintenance, optimal utilization of energy storages and sources is ensured though the CCL.

Whereas, the ECL handles the emergency conditions such as bus fault or source faults through reconfigurable control to coordinate various microgrid resources while identifying and isolating the faulty microgrid segment and continue the operations with remaining heathy system. The proposed autonomous LVDC-MG under study is designed to operate at 48 V and net rated power capacity of 4 kW composed of various locally available Renewable Energy Sources (RESs) including Solar Photovoltaic (SPV), Fuel Cell (FC), with battery-UC based Energy Storage System (ESS) with DC/DC converters. The ESS combination of battery-UC is used to compensates for slower dynamic response of battery during transient phases and to enhance the system power quality. The SPV system is generally operated with the Maximum Power Point Tracking (MPPT). The SPV converter is fed with solar PV emulator iTECH6536C which can mimic the characteristics of solar PV panels.

The SPV is connected to microgrid bus through DC/DC boost converter. The battery pack with two batteries, each of 12V/35Ahr Lead-Acid type connected in series is used to form a battery source. The UC source is configured with LS-Mtron 165F/ 48V UC unit. The battery and UC are interfaced with MG bus through two distinct Bidirectional Converters (BDC). In addition to these sources, the emulated fuel cell imitating characteristics of 24 V/50 A Proton Exchange Membrane Fuel Cell (PEMFC) is used to support the MG bus load requirement. The proposed LVDC-MG power architecture thus configured have two dispatchable sources (ESS and FC) and one non-dispatchable source i.e., SPV. The MG bus is designed with a ring type bus configuration as shown in Fig. 3 which provides more reliability and flexibility in operation under any emergency conditions. MG bus is sectioned in multiple bus segments to allow easy isolation of faulty bus segment.

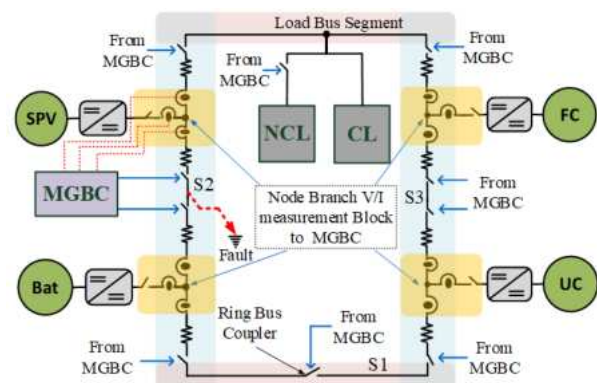Fig. 2. Proposed Three-level Hierarchical Control and Assigned Functions

Fig. 3. Schematic of LVDC MG with four bus segments forming Ring Power Network with the help of Ring Bus Coupler

The measurement and monitoring of voltages and currents in each of the segments and the nodes facilitates verification of the healthy status and onset of any fault conditions. The resistive elements shown in figure represents the MG bus resistance for that segment. Each of the converter associated with ESS and FC are programmed to work in different modes like VCM, CCM, droop control mode and that for SPV converter, MPPT mode and droop control modes are configured.

For coordination control, communication based hierarchical control structure is used for power sharing from battery-based ESS and fuel cell to maintain stable bus voltage profile in steady state operating conditions.

The coordination decision and local level control under normal and emergency conditions are implemented in different control layer. Various control boundaries have been identified based on the operational limits of the various microgrid resources. The Supervisory Controller (SC) is configured on TI's Dual core TMS320F28379D board whereas the Local Controller (LC) for each source is realized on TI's- TMS320F28069 controller boards. A central Microgrid Bus Controller (MGBC) is embedded in TMS320F28379D board itself and is programmed for monitoring the bus voltage and branch currents to facilitate health assessment of the microgrid resources. It interacts closely with the supervisory controller. Fig. 4 shows the hardware setup of the proposed LVDC-MG under study. The detailed description of the hardware setup for the proposed study is reported in [13]. The proposed reconfigurable coordinated control is implemented through the interaction of MGBC with SC and LCs. MGBC is dedicated for observing the bus voltage / current parameters and evaluating the health of MG. The measured branch currents are used to perform fault identification and location algorithms. The reconfigurable control implementation is carried out at two levels viz.- first at the level of LCs with operational mode reconfiguration and second at the level of assigning the responsibility to each of the source with its LC to ensure the sustained operation under any emergency conditions.

III.1. *Control of Microgrid Source Converters*

A solar PV converter is configured to operate in either MPPT or current control mode. The Perturb and Observe (P&O) algorithm is used for MPPT.
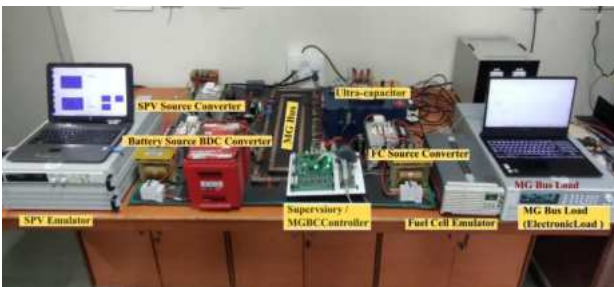
Fig. 4. Hardware Setup of the Proposed LVDC-MG

The control structure for SPV converter is presented in Fig. 5(a). The Proportional-Integral (PI) controller is used in current and MPPT controllers. The PI controller transfer function is $(K_p + K_I/s)$. The mode of operation is selected by the Supervisory Control (SC). In SPV source, the MPPT mode is used as default mode to ensure the extraction of available power for supplying the microgrid loads and thus reducing the burden on other sources like FC, Battery, and UC. The CMC mode is activated when SPV power is more than the load demand. The bi-directional converter is used to process the BESS power.

As shown in Fig. 5(b), The BDC is designed to operate in three modes; viz.-CMC, VMC and battery charging mode. In the situation of excess generation from SPV, the battery charging mode is activated to maintain the MG bus voltage by absorbing excess power. The control scheme for Fuel Cell source converter is as shown in Fig. 5(c). In full load condition, the fuel cell source working in current controlled mode supplements the SPV sources feeding the load.


(a)

(b)

(c)

(d)
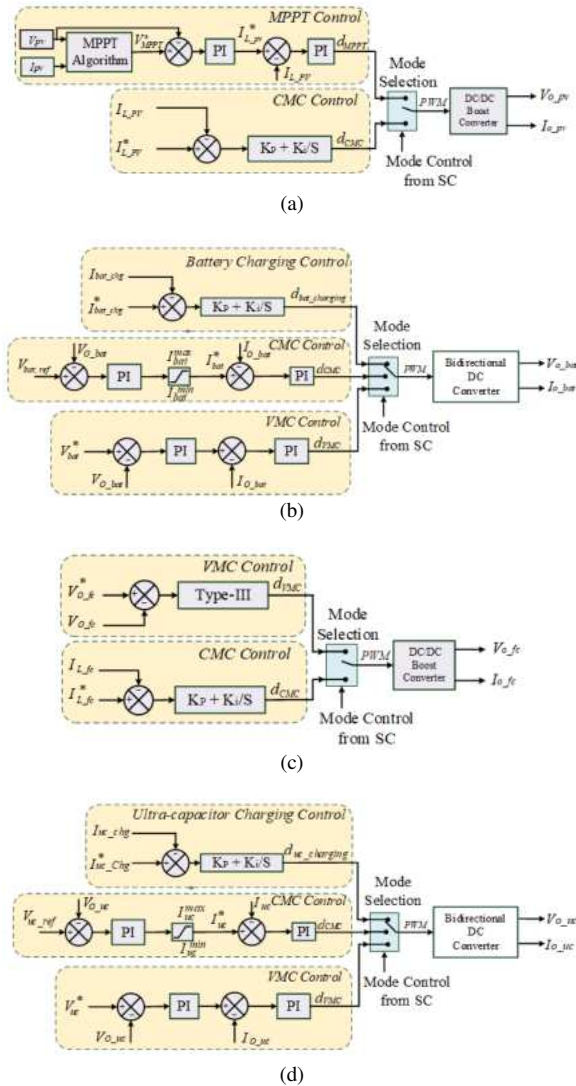
Figs. 5. (a) Control Scheme of SPV Boost converter; (b) Control Scheme of BESS Converter; (c) Control Scheme of Fuel Cell converter; (d) Control Scheme of UC converter

It is configured in VMC to deliver the available power to the load while maintaining the MG bus voltage when Battery source is engaged in charging through the FC.

The Type III controller is used for VMC operation of the FC source as the droop in the FC terminal voltage is significant from no load to full load condition. The ultra-capacitor converter is configured in VMC, CMC and charging modes as shown in Fig. 5(d). The VMC mode is the default mode to handle the transient current requirement and thus to relieve the battery source from supplying the transient load. The reference voltage for UC source is always kept below MG bus voltage which is 48V. This ensures that the UC source will always be ready in VMC but will not be participating in power sharing under steady state operations. But in transient loading conditions, as the MG bus voltage falls below the reference voltage of UC source, the UC will pump the current to fulfill the transient demand. It is ensured that the UC's State of the Charge (SoC) is always maintained above 50% for its readiness to handle transient load conditions. The charging mode facilitates the fast charging of the UC under any possible situations. Under light load conditions, the UC source also facilitates the CMC mode to supplement battery and FC sources.

III.2. Converter Specifications and Controller for Microgrid Source Converters

As mentioned earlier, Boost converter topology shown Fig. 6(a) is used for the SPV and FC sources, and the Bidirectional Converter (BDC) topology shown in Fig. 6(b) is used for Battery and UC sources. The BDC provides buck and boost operations for facilitating the charging and discharging of Battery and UC. Table I gives the details of the converter's specifications used for the proposed LVDC Microgrid. Local Controllers (LCs) acting directly on these converters are designed with the VMC, CMC, Charging/ Discharging modes and MPPT control algorithms.

(a)

(b)
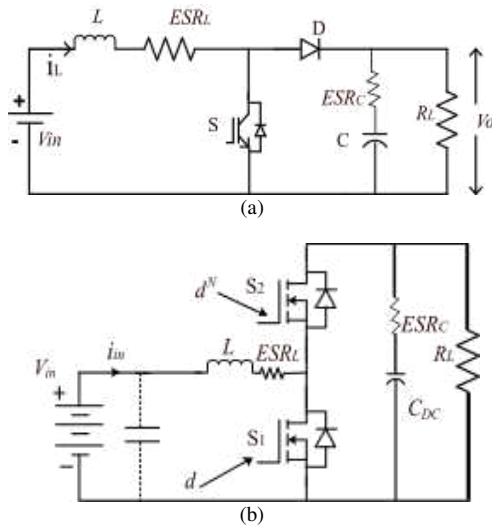
Figs. 6. (a) Boost Converter used for SPV and Fuel Cell Source; (b) Bi-directional Converter (BDC) used for Battery and UC

TABLE I
CONVERTERS SPECIFICATIONS AND COMPONENTS USED

Source & Converter type	V_{IN}	P_{OC} (kW)	L (mH)	ESR_L	C_{DC}	ESR_C
Battery (BDC)	24V	1kW	0.56 mH 50A	10mΩ	470μF 200V	0.05Ω
SPV (Boost)	31V	1kW	0.26 mH 50A	6 mΩ	1000μF 200V	0.1Ω
Fuel Cell (Boost)	24V	1.2kW	0.56 mH 50A	10mΩ	1000μF 200V	0.1Ω
UC (BDC)	24V	2.0 kW (peak)	0.56 mH 50A	10mΩ	200μF 200V	0.17Ω

The selection of the operational mode is done through the coordinated control algorithm through Supervisory control. Some insights about the current and voltage controllers used in the above modes are described below.

III.3. Current Controller and Voltage Controller

CMC and VMC are implemented with outer voltage control loop and inner current control loop. The current control loop is designed with the wider bandwidth to provide faster response (time constant τ_{CI}) while to avoid the disturbance due to switching frequency (ω_S) component in the feedback loop, the gain-crossover frequency (ω_{CI}) < ω_S is ensured. In this study, generally, ω_{CI} is set to ω_S /10. The Plant Transfer Function (G_I) for Buck/ Boost/ Bi-directional converter for current controller is given in Table II. The dominant pole of $G_p(s)$ located at $S = -ESR_L/Ls = -ESR_L/L$ is poorly stable as the ESR_L is very low. Therefore, a PI controller is effective to ensure the stable reference current tracking. The outer voltage controller bandwidth is set to 1/30th of ω_s as faster dynamic response is not generally essential. The plant transfer function (G_V) for voltage controller is as given in Table II. Fig. 7 shows the Bode plot of open loop and closed loop system transfer function for current controller and voltage controller for SPV boost converter.

TABLE II
CONVERTERS PLANT TRANSFER FUNCTION AND CONTROLLER

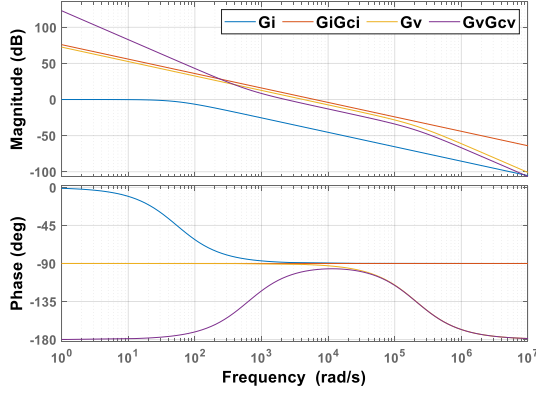| Plant Transfer Function (PTF)/Controller |
|---|
| Current Controller |
| PTF |
| $$G_I(S) = \frac{\hat{I}_L}{\hat{d}} = \frac{1}{Ls + ESR_L}$$ |
| Controller $\quad G_{CI}(S) = \frac{K_P S + K_I}{S}$ |
| Where |
| $$K_P = \frac{L}{\tau_{CI}} \; ; \; K_I = \frac{ESR_L}{\tau_{CI}} \; ; \; \tau_{CI} = 1/\omega_{CI}$$ |
| Voltage Controller |
| PTF |
| $$G_V(S) = \frac{\widehat{V_O}}{\hat{d}} = \frac{V_{IN}}{(1-D)^2} \frac{\left(\frac{S}{\omega_{ESR_C}} + 1\right)\left(1 - \frac{S}{\omega_{RHP}}\right)}{\left(\frac{S}{\omega_O}\right)^2 + \frac{S}{\omega_O Q} + 1}$$ |
| Controller $\quad G_{CV}(S) = \frac{\frac{\omega_{CV}}{kA_{CV}}\left(\frac{\sqrt{k}}{\omega_{CV}}\right)^2}{S\left(\frac{S}{\sqrt{k}\omega_{CV}}+1\right)^2}$ |
| Where |
| $$\omega_{ESR_c} = \frac{1}{ESR_C} \; ; \; \omega_O = \frac{1}{\sqrt{LC}} \; ; \; \omega_O Q = \omega_{RHP} = \frac{R_{LOAD}}{L}$$ |

Fig. 7. Bode plot of open-loop and closed-loop system transfer function for voltage and current controllers of Boost converter for SPV source

The dominant double pole of G_V, results in a sudden phase lag of 180° which needs to be compensated by a phase boost. Generally, Type III compensator is more suitable for such applications, but in this study PI controller is used. which results in slight instability.

III.4. Maximum Power Point Tracking Control (MPPT)

The standard Perturb and Observe (P&O) MPPT algorithm is incorporated to extract maximum power from SPV source under all operating conditions. The MPPT control algorithm is integrated with CMC operates SPV source at around 30 V to deliver the available power to the load at given radiation level.

III.5. Power Sharing Strategy

Due to dynamically changing MG sources especially SPV source and continuous change in load, unbalance in source and load power is introduced in autonomous microgrid operation which in turn affects the MG bus voltage profile. To overcome the above-mentioned problem, coordinated operation of each MG source and ESSs converters is needed. The proposed coordinated control strategy ensures the reliable power supply and optimal source utilization under all operating conditions.

Under the light load conditions, the SPV source is operated in MPPT mode to extract maximum energy available and supply the load. The battery and UC sources are operated in charging mode to absorb the differential power. The FC source is kept on standby.

The power is balanced between system load and sources using following Eq. (1):

$$P_{PV} = P_L + P_{BESS} + P_{UC} \tag{1}$$

All such normal operating conditions and the corresponding converter control modes are shown in Table III. The sources which are configured in VMC shall maintain the MG Bus voltage and the one in CMC will supply the demanded load power. The source with VMC operation will dynamically supply the load power as per the requirement.

TABLE III
CONVERTER OPERATING MODES UNDER NORMAL LOADING CONDITIONS

Operating Modes / Load condition	SPV	Battery	Fuel Cell	UC
Light Load with Battery and/or UC charging	MPPT Mode	Charging Mode	Charging Mode	Charging Mode
	$P_{PV} = P_L + P_{BESS} + P_{UC}$			
Light Load with Battery and/or UC Discharging mode	CMC	VMC	OFF	VMC @44V
	(Normal) $P_{PV} + P_{BESS} = P_L$			
	(Transient) $P_{PV} + P_{BESS} + P_{UC} = P_L$			
Partial Load	MPPT / CMC	VMC/ CMC	OFF/ CMC/ VMC	VMC @44V
	$P_{PV} + P_{BESS} + P_{UC} + P_{FC} = P_L$			
Full load	MPPT	VMC	CMC	VMC @44V
	$P_{PV} + P_{BESS} + P_{UC} + P_{FC} = P_L$			

The UC source is configured to operate in VMC with the reference voltage set at slightly more than 90% of the bus voltage i.e., approximately 44 V.

IV. Proposed Reconfigurable Coordination Control Scheme

In a microgrid, it is very essential to ensure the availability of power to the load under all operating condition. In steady state conditions, the microgrid operational control is required to engage only in the source power management and the load management.

But the microgrid may face some of the emergency situations as listed below which are to be tackled:
1. Short circuit fault at MG bus or source terminals;
2. Loss of the dispatchable source maintaining the MG bus voltage;
3. Failure of a source due to:
   a. Loss of source power- SPV with no solar radiation (passing clouds) or battery with sudden loss of SoC;
   b. Loss of local controller of a particular source converter;
   c. Any other critical component failure of a particular source converter;
4. Loss of communication link;
5. Heavy overload or high transient current loading.

In autonomous microgrids, there can be many more abnormal or emergency situations that may result in a difficulty to maintain the microgrid operational. Some cases may cause the microgrid to shut down completely.

In case of shutdown, the microgrid need to go through the black-start operation to initiate the process of energization the network. So, it is important that in emergency conditions, the microgrid should sustained its operation in best possible ways [14]. For safe and reliable operation, the system demands significant change in control and coordination between various subsystems of microgrid to survive and continue the operation. The emergency control is designed to maintain the reliability of the supply when abnormal conditions occur in the system. The emergency control has the higher priority to schedule each source, storage, and load converter

operating in a reasonable mode. The control action is based on observability of branch current magnitude over each bus segment of the microgrid. The proposed scheme is implemented with the help of the MGBC. Some of the emergency conditions can be handled through the simple coordination. Some situations like loss of a dispatchable or MG bus faults etc., demands restructuring or reconfigurable feature to ensure the continuation of operation through healthy resources and isolation of faulty elements. The simulation and experimental studies were carried out to verify the effectiveness of operational management of microgrid under both steady state and abnormal or emergency conditions. The following subsection highlights some of the key simulation results of the proposed reconfigurable coordinated control functionalities to sustain the MG operation under the specific emergency conditions.

IV.1. Simulation Study of the Emergency Fault Conditions

As shown in Fig. 3, the DCMG under study is designed with two dispatchable sources, Battery and Emulated Fuel Cell. These are supported with one non-dispatchable source i.e., solar PV source and the transient backup provided by UC source. As mentioned in Table III, in this power architecture, at any given time, battery source shall operate to maintain the MG bus voltage and SPV source will be engaged in managing the load current requirement. The SPV source is also controlled to maintain the SoC of the battery to a suitable value. The FC source is engaged only when the effective load on DC MG is large enough. In the situation when the battery source fails or not in position to maintain the MG bus voltage, then also the FC is engaged to execute the responsibility given to the battery source. With the above considerations the proposed DCMG simulation model is created in PSIM simulation platform and various operating conditions have been simulated. The simulation results are as shown below. Fig. 8 shows the simulation result of the continuous high impedance fault on MG bus on bus segment S3 with 1 Ω load resistor is shunted across the MG bus terminals. The high impedance fault level is in the range of 35 A. The sustained high impedance fault does not take MG bus voltage to zero but causes significant voltage dip nearly to 13 V.
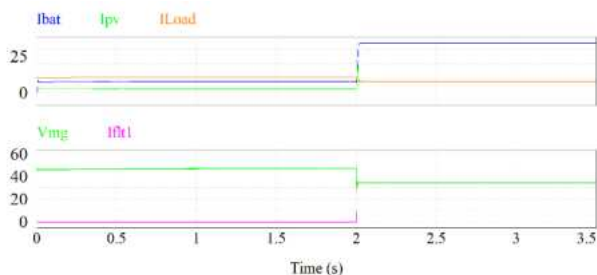
Fig. 8. Continuous High Impedance fault (1Ω) with Battery Source in VMC and SPV CMC mode (current in A and voltage in V)

Fig. 9 shows the simulation result of the continuous Dead short circuit fault on MG bus segment S3. The simulated short circuit fault level (I_{flt1}) is in the range of 200 A. The contribution from all active MG sources also can be seen. The similar simulations were carried out when FC is operated in place of battery source to understand the fault levels. The results are as shown in Fig. 10 and Fig. 11. As can be seen, the fault current levels are much lower compared to the battery source operations. This is due to the fact the FC source has a limited peak current capacity compared to the battery source.

IV.2. Simulation Study of the Reconfigurable Control Under Emergency Fault Conditions

These simulations are carried out to verify the effectiveness of the proposed reconfigurable coordinated control. The reconfigurable coordinated control is carried out at two levels. One at the power topology and second at the operational control of the sources. In the event of faults like short circuit on MG bus, MGBC controller monitoring the current and voltages at every branch and nodes, detects the increase in the fault current or dip in the MG bus voltage.
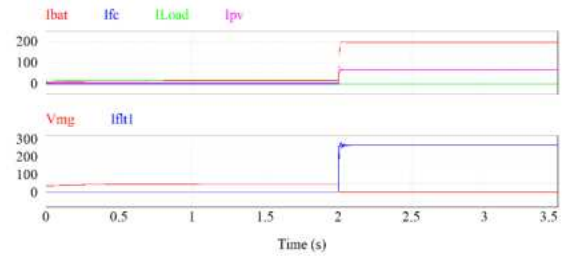

Fig. 9. Continuous Dead Short Circuit fault with Battery source in VMC and SPV CMC mode (current in A and voltage in V)
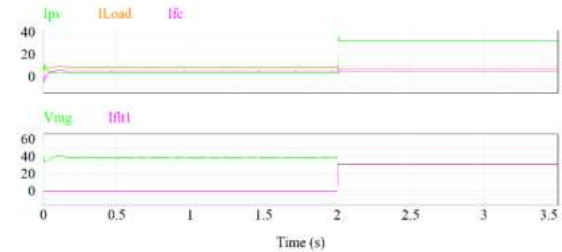

Fig. 10. Continuous High Impedance fault (1Ω) with FC source in VMC and SPV in CMC mode (current in A and voltage in V)
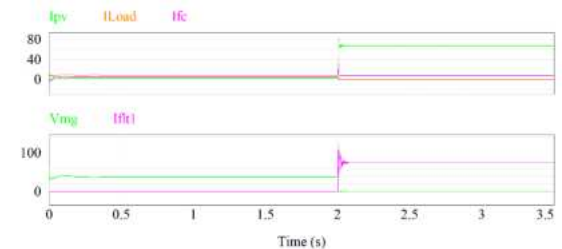

Fig. 11. Continuous Dead Short Circuit fault with FC Source in VMC and SPV CMC mode (current in A and voltage in V)

The MGBC controller is programmed to identify the location of the fault based on the current and voltage status of each bus segment. Once the faulty bus segment is identified, that bus segment is isolated by opening the branch switches by MGBC. Thus, faculty section is separated keeping the healthy section to continue the MG operation. The MGBC samples the data of the various nodes and branches at the interval of control code ticking time i.e., 50 µs. Considering the system time constant, the response time decided is 10 ms which is safer for all the MG resources. Fig. 12 shows the simulation result where a dead short circuit fault on MG bus segment S3 at 2 seconds results in fault current to rise around 200 A (I_{filt1}). MGBC identifies the fault and isolates bus segment S3 in 10 ms restoring the healthy sections of MG bus. As this isolation disconnects the rest of the healthy section of MG bus from battery source, the Ring bus-coupler is closed to reroute the power to the MG load. Thus, there is reconfiguration of the power topology at bus level helps to restore the operating condition prevailing before the fault. Fig. 13 shows the simulation result where a high impedance fault on MG bus segment S3 at 2 seconds results in fault current to rise around 35 A (I_{filt1}). In this case also, the MGBC identifies the fault and isolates bus segment S3 in 10 milliseconds restoring the healthy sections of MG bus.

Thus, there is a reconfiguration of the power topology at bus level which helps to restore the operating conditions prevailing before the fault. Figs. 14 and Figs. 15 show the similar fault conditions at non-critical load segment (dead short as well as high impedance fault conditions). MGBC shows it way to disconnect and isolate the complete the non-critical load, isolating the faulty load segment while maintaining the critical load supply without any disruptions.
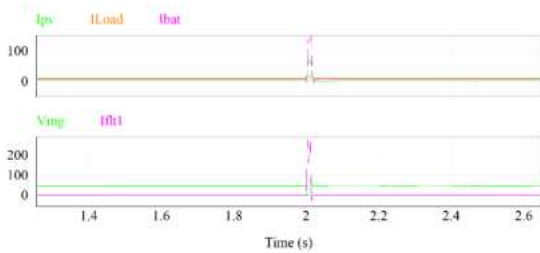
Fig. 12. Dead Short Circuit fault on MG f with Battery source in VMC and SPV CMC mode occurred at 2 s and isolated in 10 ms restoring the healthy sections of MG bus. (Current A / Voltage V)
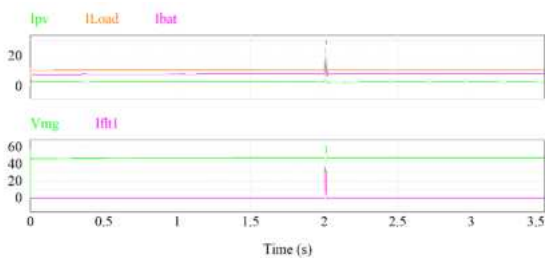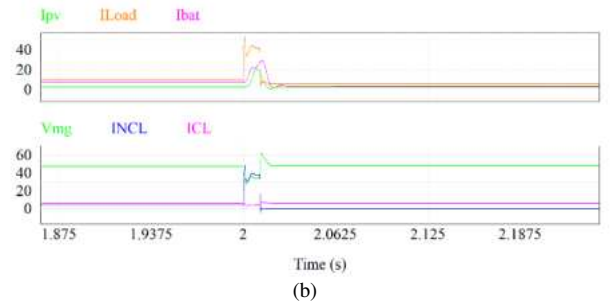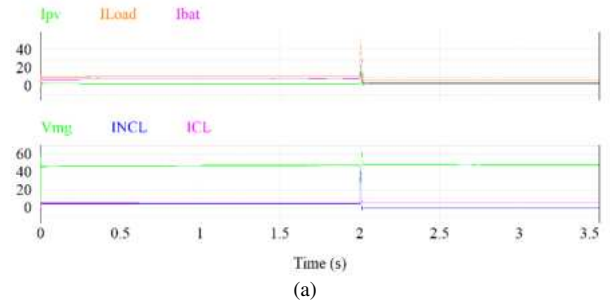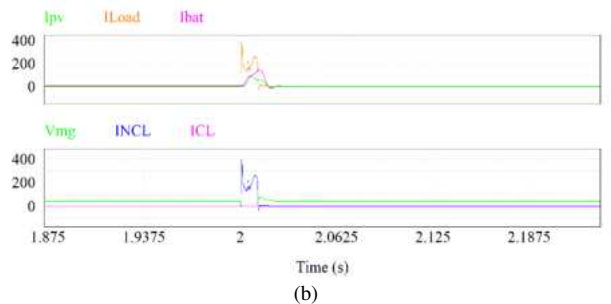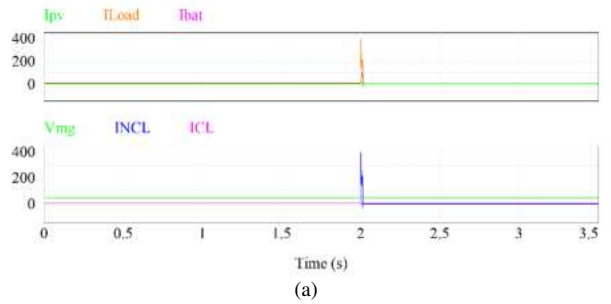

Fig. 13. High Impedance fault with Battery Source in VMC and SPV CMC mode (current (A) / voltage (V) occurred at 2 s. and isolated in 10 ms

Figs. 14. (a) High Impedance fault (1Ω) at Non-Critical Load (NCL) termination (current in amps and voltage in volts) occurred at 2 s and isolated in 10 ms (b) Expanded view

Figs. 15. (a) Dead Short circuit fault at Noncritical load (NCL) termination (current in amps and voltage in volts) occurred at 2 s; (b) Expanded view

The recovery of system shows the increase in bus voltage (as can be seen in the expanded view) after the isolation which is due to the sudden reduction in MG bus load.

The loss of source maintaining the MG bus voltage can be very dangerous as it may result in sudden rise or fall in bus voltage resulting in damage to the connected resources and load. Fig. 16 shows the emergency condition where there is loss of the battery source resulting in MG bus operation with SPV in CMC mode.
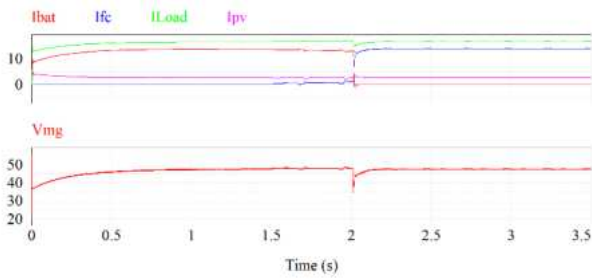
Fig. 16. Loss of Battery source resulting in MG bus operation with SPV with CMC mode- Reconfiguration of the FC source to maintain the bus voltage and the stability of the system

The reconfiguration of the MG control to transfer this responsibility to the FC source to maintain the bus voltage and maintain system stability. As can be seen in Fig. 16, the MG bus voltage witnesses a voltage dip rather than complete non-operational situation. The battery source becomes inactive after the event. Whereas, the FC source manages the show with SPV source to maintain the MG Bus stability.

IV.3. Experimental Study of the Emergency Fault Conditions

In an autonomous LVDC-MG, the short circuit fault level is determined by the factors viz. the number of sources operating under given situation, the available source power capacity and peak current rating and source to fault network impedance. In order to activate the emergency response mechanism under the reconfigurable coordinated control, it is essential to know these fault levels and other parameters like bus voltage so that the appropriate threshold can be fixed. The emergency conditions were created on the Microgrid lab prototype shown in Fig. 4. In normal operation, the battery source is set to operate in VMC mode and SPV in CMC mode while feeding the normal load on MG bus. The temporary dead short circuit is created across the MG bus terminals for approximately 120 ms. Fig. 17(a) shows the impact of this situation on the MG bus voltage dipping to zero during this period. The short circuit contribution by SPV source is limited due to it CMC mode of operation and limited by source short circuit capacity. Transient contribution comes from output capacitors of the converters which is around 200 A. Fig. 17(b) shows the contribution of battery and SPV sources towards the high impedance fault (heavy overload) case, a 1 Ω load resistance is connected across the MG bus for short duration. The fault current is limited to 40 A. Fig. 17(c) shows the impact of capacitor bank switching transient on MG operation. The amplitude of the transient current drawn by the capacitor bank depends upon the bus voltage and capacitor value. In this case, uncharged film capacitor bank of 200 µF is placed across the MG bus.

This transient loading does not affect the MG bus voltage, but can impact any of the MG source while supplying the transient current seriously resulting in probable converter protection to get activated.
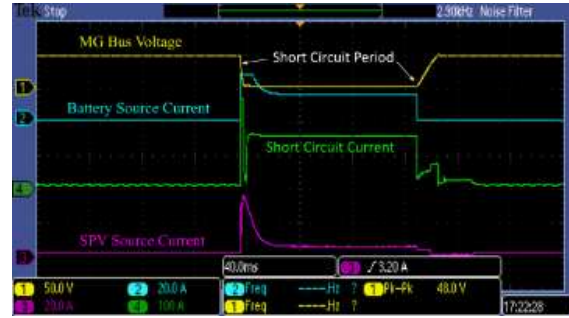

(a)

(b)

(c)

Figs. 17. (a)Temporary Dead Short Circuit fault at bus segment S2; (b) Short duration High Impedance fault (1Ω) on MG bus segment S2; (c) Transient current demand-with Capacitive bank switching

Figs. 18 show the impact of the loss of generation from any of the active MG source. Fig. 18(a) shows the normal operation for the reference. Battery source operating in VMC and SPV source in CMC mode. SPV source delivers the set power to the load and rest comes from battery source. In the event of passing cloud over the SPV panels will result in loss of its generation suddenly and then battery source has to take on the complete MG load as can be seen in Fig. 18(b). Figs. 18(c), (d) and (e) show three different operating conditions resulting in different impact on the MG bus voltage when the loss of battery source takes place. Fig. 18(c) shows impact of loss of the battery source when the SPV source is handling the complete MG bus load. In this case the MG bus voltage does not change, the system appears to be healthy. Fig. 18(d) shows the impact of load changes under these conditions resulting in continuous change in bus voltage as SPV source is operating in CMC mode. Fig. 18(d) shows the significant fall in MG bus voltage leading to possible shutdown of MG. The complete shutdown is not desirable in MG operation.
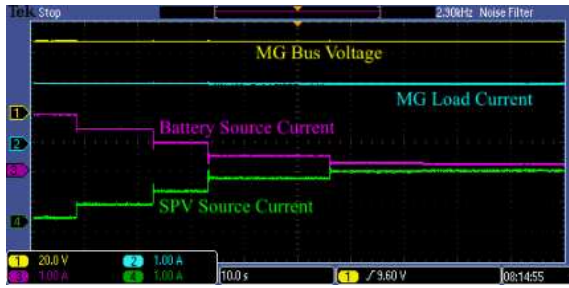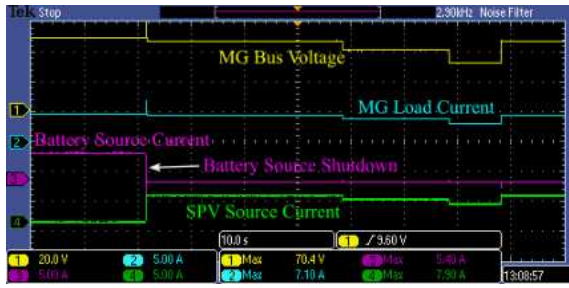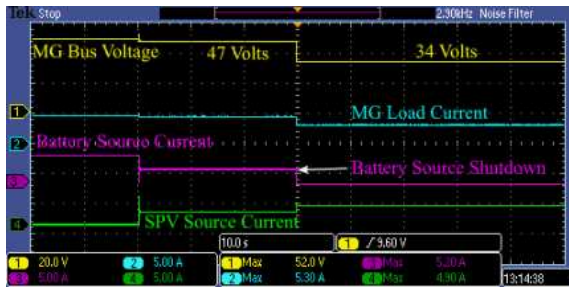
(a)
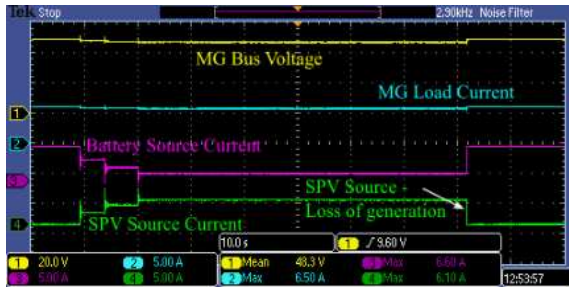
(b)
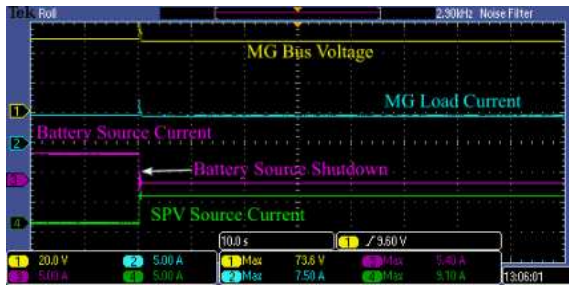
(c)

(d)

(e)

Figs. 18. (a) Normal operation of MG; (b) Loss of the SPV source generation resulting in sudden loading of battery source; (c) SPV source handling the complete MG bus load in normal condition resulting in constant MG bus voltage in the event of loss of the battery source; (d) Loss of the battery source resulting continuous change in Mg bus voltage due to CMC operation of the SPV source; (e) significant fall in MG bus voltage

The next section illustrates how the proposed reconfigurable coordinated control offers recovery out of these situations.

IV.4. Experimental Study of Reconfigurable Control Under Emergency Fault Conditions

In the event of loss of the source operating in VMC mode responsible for maintaining the MG bus voltage, one of the solutions is to bring in alternate source in VMC mode to take over the same responsibility. In the proposed MG power architecture, FC is an alternative to battery being a dispatchable source. Before the event, the FC source may be active in CMC mode or on idle depending on the load demand. If it is operating in CMC mode, then immediately after the failure of battery source, the FC mode is changed to VMC from CMC as shown in Fig. 19.

The loss of battery source is identified as the bus voltage falls significantly except under balanced power conditions. This emergency condition is managed with reconfigurable control approach resulting in continuous MG operation with only small glitch in the MG bus voltage.

Fig. 20(a) shows dead short circuit fault resulting in large current drawn from all the active sources. The MGBC monitoring the node voltages and branch current, identifies the location of the fault, trips the relevant bus contactors isolates the faulty bus segment and close the Ring bus coupler.

This sequence of operation facilitates the quick (40 ms) recovery of MG from dead short circuit fault. Fig. 20(b) shows the similar situation with higher fault impedance (1Ω) resulting in lesser fault current but MGBC locates and isolates the fault allowing with reconfigurable control to recover the system.

Figs. 21(a) and (b) show the participation of UC source under dead short circuit and high impedance short circuit fault conditions. Under any kind of short circuit faults, the UC source significantly contributes to fault current along with the other source. This increase fault current levels, enables the quick detection, location and isolation of faulty bus segment, therefore quick recovery of the system. Only in this case 50% rise in MG bus voltage is observed for a short period due to faster dynamics of the UC.
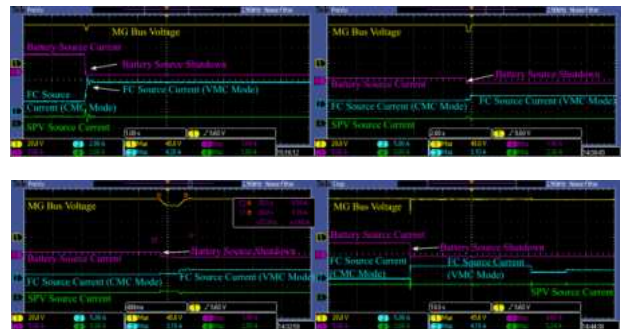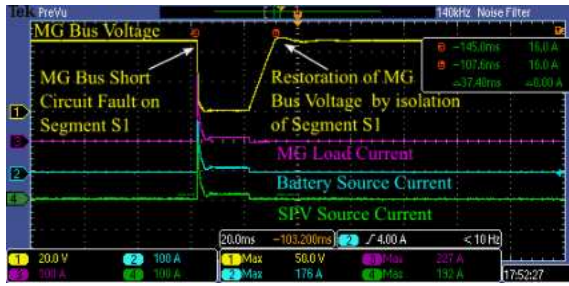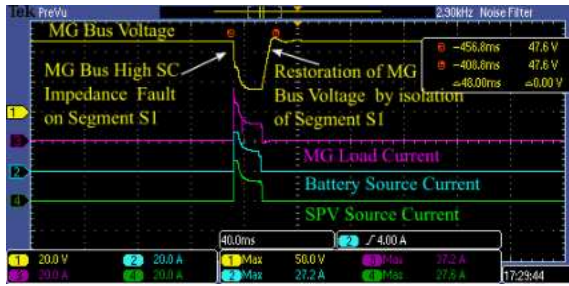

Fig. 19. Loss of Battery source (VMC mode): FC Switches to VMC mode from CMC mode and maintain the stability of the microgrid
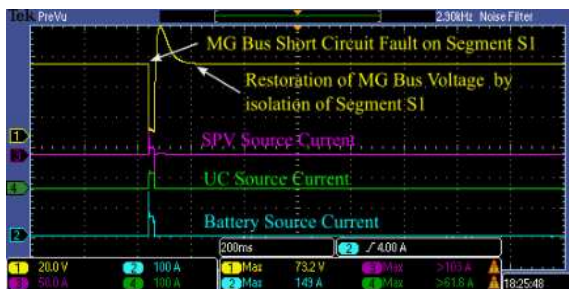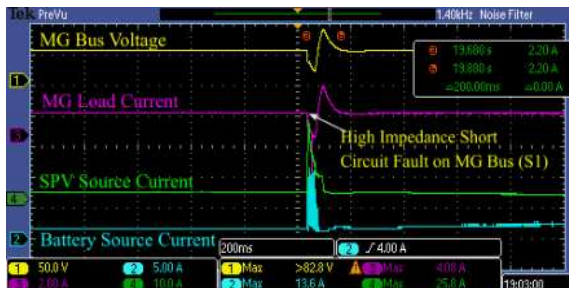
(a)

(b)

Figs. 20. (a) MG bus Short Circuit fault with Reconfigurable Control,
(b) High Short Circuit Impedance Fault with Reconfigurable Control

(a)

(b)

Figs. 21. MG bus Short Circuit Fault and MG bus High Short Circuit
Impedance Fault with UC source participation. Reconfigurable Control
restores the system quickly

IV.5. Results and Discussions

The results obtained in simulation and experimentation show successful implementation of a novel reconfigurable coordinated control for a low voltage autonomous DC Microgrid. As can be seen from the simulation and hardware results Under, the normal operating conditions, the power sharing between various sources ensures the appropriate loading of each microgrid sources while fulfilling the load requirement.

The power balance with generation and load demand is always met to ensure the MG bus voltage to have constant flat profile.

The reconfigurable coordinated control feature is extremely useful to sustain the microgrid operation under emergency conditions. The simulation and experimentation results with overload, transient loading, loss of generation and short circuit conditions on MG system provide assured continuity of the MG operation. The reliability enhancement of MG through this reconfiguration is witnessed in the results.

One more aspect also gets highlighted in the results that after the reconfiguration of the system topology or control, the operation of MG continues to assume the normal operating conditions with the healthy microgrid resources and share the load current according to the laid down the control laws. The proposed control strategy assures the reliable operation under normal as well as emergency conditions thus meeting the achievement of main objectives of microgrids. In LVDC Autonomous MG, the successful control strategy implementation demands clear understanding of dynamics of all energy sources and storage elements used in power topology.

V. Conclusion

Autonomous LV DC microgrids are very important from the context of remote area electrification where grid supply is not available. Sustainable and reliable Microgrid operation under all circumstances will be one of the major requirements in such applications.

Appropriate power architecture based on locally available energy resources along with the proposed novel reconfigurable coordinated control strategy can provide such possibility.

This paper illustrated the particulars of LVDC autonomous microgrid power topology, a proposed reconfigurable control architecture and operational details under steady state and emergency conditions. The proposed reconfigurable control showcased the reliability of the system with a three layered hierarchy of emergency control layer sandwiched between the supervisory and local control layers. The proposed emergency" control layer facilitates of system management under emergency conditions to coordinate the energy sources, loads and controllers. It provides the fault identification and isolation to ensure the reliable operation of the healthy microgrid sections and speedy recovery of faulty section. The key hardware and simulations results presented validate the proposed architecture along with the control implementation. The research work illustrated in this paper did not account for source and system optimization. In future scope of the work, the source and system performance optimization can be achieved. The objective function can be configured around economic dispatch, life cycle optimization while ensuring the reliability under all operating conditions. This shall be then the best solution for remote area electrification.

References

[1] R. Wandhare, S. Thale and V. Agarwal, Reconfigurable Hierarchical Control of a Microgrid developed with PV, wind, micro-hydro, fuel cell and Ultra- Capacitor, *28th Annual IEEE App. Power Electron. Conference and Exposition (APEC-2013)*, March 17-21, 2013, Long Beach, CA, USA.

[2] S. Thale, R. Wandhare, and V. Agarwal, A novel Reconfigurable Microgrid Architecture with Renewable Energy Sources and Storage, *IEEE Trans. Ind. App.,* vol. 51, no. 2, March 2015, pp. 1805 - 1816.

[3] P. Cairoli, R. Dougal, Fault Detection, and Isolation in Medium Voltage DC microgrids: Coordination Between Supply Power Converters and Bus Contactors, *IEEE Trans. Power Electro.,* vol. 33, no. 5, May 2018, pp. 4535 – 4546.

[4] K. Subramaniam, M. Illindala, High Impedance Fault Detection and Isolation in DC Microgrids, *IEEE/IAS 55th Ind. and Comm. Power Systems Technical Conference (I&CPS),* May 5-8, 2019, Calgary, AB, Canada.

[5] D. Dam, and Hong-Hee Lee, A Power Distributed Control Method for Proportional Load Power Sharing and Bus Voltage Restoration in a DC Microgrid, *IEEE Transactions on Ind. App.*, vol. 54, no. 4, July-August 2018, pp. 3616 - 3625.

[6] M Taheruzzaman, Designing and Sizing of standalone solar homes system integrated microgrid: for rural electrification, *2019 5th International Conference on Advances in Electrical Engineering (ICAEE)*, Jan 30, 2020, Dhaka, Bangladesh.

[7] P Rani; Shikhar; S Murugesan; A Singh, Modeling and Implementation of Grid Following and Grid Forming Inverters, *2022 IEEE 9th Uttar Pradesh Section International Conference on Electrical, Electronics and Computer Engineering (UPCON)*, Dec 02-04, 2022, Prayagraj, India.

[8] Sandeep Anand and B. G. Fernandes, Reduced-Order Model and Stability Analysis of Low-Voltage DC Microgrid, *IEEE Transactions on Industrial Electronics,* vol. 60, no. 11, Nov. 2013, pp. 5040 - 5049.

[9] M. Hamzeh, A. Ghazanfari, Y. Abdel-Rady, I. Mohamed, Y Karimi, Modeling and Design of an Oscillatory Current-Sharing Control Strategy in DC Microgrids, *IEEE Transactions on Industrial Electronics*, vol. 62 no. 11, Nov. 2015, pp. 6647 – 6657.

[10] Q. Xu, Y. Xu, C. Zhang, P. Wang, A Robust Droop-Based Autonomous Controller for Decentralized Power Sharing in DC Microgrid Considering Large-Signal Stability, *IEEE Transactions on Industrial Informatics*, vol. 16 no. 3, March 2020, pp. 1483 – 1494.

[11] C. Jin, P. Wang, J. Xiao, Y. Tang, and F. Choo, Implementation of Hierarchical Control in DC Microgrids, *IEEE Trans. Ind. Electronics,* vol. 61, no.8, Oct. 2013, pp. 4032 – 4042.

[12] Z. Zhao, J. Hu, J. Liu, Hierarchical Coordinated Control of Multi bus-based DC Microgrid considering fault occurred in buses, *2016 China International Conference on Electricity Distribution (CICED),* August 10-13, 2016, Xi'an, China.

[13] S. Muchande and S. Thale, Hierarchical Control of a Low Voltage DC Microgrid with Coordinated Power Management Strategies, *Engineering, Technology & Applied Science Research,* vol. 12, no. 1, pp. 8045-8052, Feb. 2022.

[14] Jamaica-Obregón, J., Moreno-Chuquen, R., Flórez-Cediel, O., Optimal Operation of Grid-Connected Microgrids with Photovoltaic Generation and Storage, (2021) *International Review of Electrical Engineering (IREE)*, 16 (1), pp. 50-59.
doi: https://doi.org/10.15866/iree.v16i1.18561

[15] D. Salomonsson, L. Soder, and A Sannino, Protection of Low-Voltage DC Microgrids, *IEEE Trans. Power Deli.,* vol. 24, no.3, July 2009, pp. 1045 - 1053.

[16] C. Yuan, M. Haj-ahmed, and M. Illindala, Protection Strategies for Medium-Voltage Direct-Current Microgrid at a Remote Area Mine Site, *IEEE Trans. Ind. Appl.,* vol 51, no. 4, July 2015, pp. 2846-2853.

[17] G. Madingou, M. Zarghami, M. Vaziri, Fault Detection, and Isolation in a DC Microgrid Using a Central Processing Unit, *2015 IEEE Power & Energy Society Innovative Smart Grid Technologies Conference (ISGT),* February 18-20, 2015, Washington, DC, USA.

[18] D. Wang, V. Psaras, A. Emhemed, and G. Burt, A Novel Fault Let-through Energy based Fault Location for LVDC Distribution Networks, *IEEE Trans. Power Delivery,* vol. 36, no. 2, April 2021, pp. 966 - 974.

[19] S. Kumar Prince, S. Affijulla, G. Panda, Protection of DC Microgrids Based on Complex Power During Faults in ON/OFF-Grid Scenarios, *IEEE Transactions on Industry Applications,* vol. 59, no. 1, Jan.-Feb. 2023, pp. 244-254.

[20] M Senapati, C Pradhan, Fault Detection in Photovoltaic (PV) Based Low Voltage DC Micro-Grid, *2020 International Conference on Computational Intelligence for Smart Power System and Sustainable Energy (CISPSSE)*, July 29-3, 2020, Keonjhar, India.

[21] L Zubieta, Y Zhang, D Bauer, Protection Scheme for a Residential DC Microgrid, *2021 IEEE Fourth International Conference on DC Microgrids (ICDCM),* July 18-21, 2021, Arlington, VA, USA.

[22] Z Ali, Y Terriche, L Hoang, S Abbas, M Hassan, M Sadiq, Chun-Lien Su, J Guerrero, Fault Management in DC Microgrids: A Review of Challenges, Countermeasures, and Future Research Trends, *IEEE Power & Energy Society Section,* vol. 9, Sept. 13, 2021, pp. 128032-128054.

[23] Kassir, S., Doumiati, M., Machmoum, M., Francis, C., El Rafei, M., Energy Management System Based on Cost Optimization of Battery Aging and Hydrogen Consumption in a Microgrid, (2022) *International Review of Electrical Engineering (IREE)*, 17 (4), pp. 346-359.
doi: https://doi.org/10.15866/iree.v17i4.21983

[24] T Krishna, M Maharana, C Panigrahi, Integrated Design and Control of Renewable Energy Sources for Energy Management, *Engineering, Technology & Applied Science Research,* vol. 10, no. 3, Jun. 2020, pp. 5857-5863.

[25] B Long N Phung, T Nghia Le, Load Shedding in Microgrids with Consideration of Voltage Quality Improvement, *Engineering, Technology & Applied Science Research*, vol. 11, no. 1, Feb. 2021, pp. 6680-6686.

[26] Iben Ammar, I., Doumiati, M., Kassir, S., Machmoum, M., Francis, C., Chaabane, M., New Nonlinear Control Based on Polynomial Approach for Islanded DC Microgrid Robustness and Voltage Stability, (2022) *International Review of Automatic Control (IREACO)*, 15 (5), pp. 263-275.
doi:https://doi.org/10.15866/ireaco.v15i5.22535

[27] Boudiaf, B., Zebirate, S., Aissani, N., Chaker, A., Isolated Microgrid Management Using a Multi-Agent System, (2021) *International Review on Modelling and Simulations (IREMOS)*, 14 (1), pp. 1-9.
doi:https://doi.org/10.15866/iremos.v14i1.18940

[28] Delfianti, R., Nusyura, F., Priyadi, A., Abadi, I., Soeprijanto, A., Optimizing the Price of Electrical Energy Transactions on the Microgrid System Using the Shortest Path Solution, (2022) *International Review on Modelling and Simulations (IREMOS)*, 15 (4), pp. 279-286.
doi:https://doi.org/10.15866/iremos.v15i4.22712

Authors' information

Dept. of Electrical Engineering, Agnel Charities' Fr. Conceicao Rodrigues Institute of Technology, Navi Mumbai, Maharashtra 400703, India.

Shrishell Muchande (Corresponding Author) completed his B.E. and M.E degrees in electrical engineering from the University of Mumbai, Mumbai, India, in 2008 and 2013, respectively. Since 2016, he has been a research scholar in the Department of Electrical Engineering, Fr. C. Rodrigues Institute of Technology, Navi Mumbai, Mumbai, India. Since 2013, he has been a member of the Faculty of Dept. of Electronics and Telecomm. Engineering, Gharda Institute of Technology, Ratnagiri, Maharashtra, India.
E-mail: skmuchande@git-india.edu.in

Sushil Thale obtained his Bachelor's degree in Electrical Engg. in 1992 and M.E. in Electrical Engg in 1996 from University of Mumbai, India. He completed his Ph.D. from Indian Institute of Technology-Bombay with specialization in Power Electronics and Power System in 2015. He is currently working as Professor in Electrical Engineering at Fr. C. Rodrigues Institute of Tech., Navi Mumbai.

Acquisition of natural remanence in the basaltic laterites of Deccan volcanic province (India): Implications to palaeomagnetic studies in laterites

N.B. Kadam [a][e], S.J. Sangode [a] ✉, M. Venkateshwarlu [b], D.C. Meshram [a], Y.R. Kulkarni [c], Firoz Badesab [e], Jyotibala Singh [a], S.S. Gudadhe [d]

[a]   Department of Geology, Savitribai Phule Pune University, Pune 411 007, India
[b]   CSIR-National Geophysical Research Institute, Hyderabad, India
[c]   Department of Civil Engineering, Gharda Institute of Technology, Khed, Ratnagiri, India
[d]   Yashwantrao Chavan Arts, Commerce and Science College, Lakhandur, India
[e]   CSIR-National Institute of Oceanography, Panaji, Goa, India

Heavy Mineral and Mineral Magnetic Tracers of Basaltic versus Cratonic Weathering as Indicators of Spatio–temporal Shifts in the Monsoonal Intensity over Central Indian Region

Y. R. Kulkarni ✉, S. J. Sangode & D. C. Meshram

Abstract

Indian summer monsoon holds its core over Central Indian Region (CIR) through Bay of Bengal and Arabian Sea branches. The majority of CIR is occupied by the Godavari Drainage Basin (GDB) which generates a large and episodic flux of sediments in the Bay of Bengal indicating a major shift in the monsoonal pattern over CIR. The large part of Deccan basalt province of GDB is present in the semi-arid watershed governed by the precipitation mostly from Arabian sea branch. Whereas the cratonic province is present in a high monsoonal zone governed by the precipitation from Bay of Bengal branch. Both these zones also represent Cratonic (non-basaltic) versus Basaltic sources converging at the

ELSEVIER

Bioethanol from various types of banana waste: A review

Ashish N. Sawarkar [a] ⊠ , Nikhil Kirti [a], Ankita Tagade [a], Shyam P. Tekade [b]
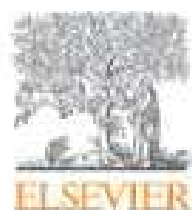
Show more ∨

+ Add to Mendeley   ⌁ Share   🙾 Cite

Get rights and content ↗

Abstract

Various types of banana waste (BWs) generated after banana crop cultivation have tremendous potential for bioethanol production. The present review paper aims to bring together information on various facets such as i) variation in physico-chemical and biochemical composition of various types of banana waste ii) various pretreatment methods, viz. mechanical, chemical, and biological iii) acid hydrolysis and enzymatic hydrolysis iv) fermentation mechanism and role of microbes in banana wastes conversion v) various fermentation schemes for bioethanol production from banana wastes, coherently on a single platform based on reported literature. Analysis revealed that novel pretreatment techniques such as organic acid pretreatment and electrical pretreatment techniques such as microwave and ultrasonic are making substantial progress. Robust statistical approaches are proven to be effective as regards to process parameters optimization. Finally, current challenges along with research needs for making further inroads in the production of bioethanol from various BWs have also been deliberated.

Graphical abstract

Insights into kinetic and thermodynamic analyses of co-pyrolysis of wheat straw and plastic waste via thermogravimetric analysis

Sanjay Singh [a], Ankita Tagade [a], Ashish Verma [a], Ajay Sharma [b], Shyam P. Tekode [c], Ashish N. Sawarkar [a] 👤 ✉

Show more ⌄

+ Add to Mendeley   ⌰ Share   🢖🢖 Cite

Get rights and content ↗

Abstract

This work studied the co-pyrolysis of wheat straw (WS) and polyethylene (PE) via thermogravimetric experiments from room temperature to 1000°C at various heating rates (10, 20, and 30°C/min). Thermal behavior revealed that the maximum decomposition of WS, PE, and their blend occurred in three temperature ranges, viz. 250 – 496, 200 – 486, and 200 – 501 °C. Kinetic parameters were determined using model-free isoconversional methods. Activation energy from KAS (163.56, 220.26 and 196.78 kJ/mol for WS, PE, and blend), FWO (165.97, 222.05, 198.86 kJ/mol for WS, PE, and blend), and Starink (163.45, 220.05, 196.46 kJ/mol for WS, PE, and blend) method was estimated. From among various solid-state kinetic models, first-order reaction kinetics

Feedstocks, Synthesis, and Characterization of Cellulosic Materials for Advanced Applications with Emphasis on Microcrystalline Cellulose (MCC)

Sunil J. Kulkarni[1]

Abstract

Cellulosic materials find applications in pharmaceutical, food, and cosmetic industry due to their surface, mechanical, and antimicrobial properties. Many investigations are reported on synthesis of cellulosic products from raw feedstocks that contains 40 to 80% cellulose. Microcrystalline cellulose (MCC) is synthesized from raw feedstock with a methodology involving alkali treatment, acid hydrolysis, and dewatering. Various modifications in terms of alkali, acid, and dewatering methods are explored for effective synthesis with desired characteristics. Also application-oriented research include combination of MCC with polymers to get better and customized materials. Microcrystalline cellulose is also used as an anticaking material, dispersing agent, and stabilizer. The properties of microcrystalline material depends on the synthesis conditions and the starting material. Being microcrystalline in structure, the characterization for its size, strength, crystallinity, pH, crystal size, stability, and flow properties is an important factor deciding the suitability of the material for specific applications. This review provides important insight on raw materials and MCC properties. The sisal fiber MCC was reported to have crystallinity index 81.5% and the Kraft pulp MCC, 88%, highest among the feedstocks. Carr's index was highest, 29–26%, for cotton MCC. pH of the product ranged from 6 to 7. The yield of MCC for raw feedstock was reported to be satisfactory, the highest being 88% for *Rabdosia rubescens* residue. This article reviews the investigations on MCC to explore feedstocks, characterization methods, and applications of microcrystalline cellulose in pure and composite form.

Keywords Crystallinity · Angle of repose · Yield · Carr's index · Hausner ratio

1 Introduction

Cellulose is the material that is abundantly present in the wood. It consists 1–4-linked β-D-anhydro glucopyranose [1, 2]. Cellulose in various forms is used in food, packaging, pharmaceutical, and beauty industry [3–7]. These forms are hydroxypropyl methyl cellulose phthalate, cellulose acetate butyrate, cellulose acetate phthalate, cellulose acetate trimelitate (CAT), and cellulose acetate (CA). Synthesis of cellulose and its derivatives is being explored by investigators for customized properties and novel methods [8–12]. In food industry, cellulose is used as an additive [13–17]. It is being used as an antimicrobial agent and coating film for packaging in the food industry applications [18–23]. Some modern applications involve cellulose composites with polymers for better properties [13–15]. Various forms of cellulosic materials are also explored for their application in paint, pigment, and color industry due to their reduced environmental foot prints compared to synthetic counterparts [24–27]. Their antimicrobial properties are advantage in these applications [28–32]. Cellulose is basically a linear polymer of glucose whereas MCC is the partially depolymerized cellulose. Pristine cellulose is less reactive. Cellulose fibrils contains two domains, one is highly ordered and other amorphous. MCC and cellulose nanocrystals can be separated from cellulosic sources [33–36]. Lignocellulosic cellulose is referred to as hemicellulose frequently. The crystalline cellulose is a result of the hydrogen bonds between monomers of glucose cellulose structure. The cellulose is classified as alpha, beta, and gamma based on its solubility in 17.5% sodium hydroxide. Crystalline structure of MCC is discontinuous and contains amorphous regions. The cellulose in the form of micro and nanocrystals has excellent mechanical and structural properties [32, 37, 38]. These forms

✉ Sunil J. Kulkarni
  suniljayantkulkarni@gmail.com

1 Gharda Institute of Technology, 415708 Lavel., Maharashtra, India

and their composites can be derived from cellulose feed stocks and can be complexed with polymers for customized material solutions [39–43]. Lignocellulosic biomass is also explored for synthesis of fuel [44–47]. Cellulose in the form of microcrystalline cellulose is a widely investigated material for its synthesis and applications. This article sheds light on the investigation on raw materials, synthesis methods, characterization, and application of MCC. Along with food, packaging, and pharmaceutical industry, MCC also finds application in membranes [48, 49].

Refined wood pulp is termed as microcrystalline cellulose [48]. Micro cellulose (MCC) can be used as an anti-caking agent, emulsifier, emulsion and thermal stabilizer, and tabulating and dispersing agent. The pharmaceutical industry is a major candidate for MCC utilization [48–52]. For the applications of MCC in pharmaceutical industry, the hydrogen bonding is a very important aspect [53–55]. Derivatives of cellulose namely nitrocellulose, cellophane, and cellulose acetate find applications in pharma industries [56]. Cellulose is half polymerized to obtain MCC [57–61]. Due to its superior excipient properties and dry nature, it is a widely used binder in pharmaceuticals [53–57]. Less lubrication during tableting is an added advantage. Important properties that contribute to a wide application of MCC include crystallinity, mechanical strength, and moisture content [62–64]. MCC can be synthesized by various processes namely enzyme mediated, steam explosion, acid hydrolysis, and reactive extrusion [65].

Synthesis of MCC from agricultural and other low-cost material is explored by the investigators to optimize the parameters, characterize the product, and explore the possibility of composite material with superior properties [66–68]. Recent studies indicate that due to its surface properties, microcrystalline cellulose can be used as an adsorbent for dyes and heavy metals [69–71]. Microcrystalline cellulose demand is increasing with its novel applications, and sustainable synthesis methods [72–75]. US market size in 2021 was 269.6 million dollars and for China it was 225.1 million dollars [72].

Many investigations are currently focused on the raw materials for better yield, properties, and economy. These articles contain the raw material purification, isolation of compounds, hydrolysis, and product analysis. Each of these aspect needs detailed discussion. In reported literatures, these aspects are discussed separately. This article is an attempt to discuss raw materials, characterization, synthesis, and application-oriented research.

2 Raw Materials

Raw materials for microcrystalline cellulose are composed of lignin, hemicelluloses, and cellulose. Wood pulp and cotton linters are usually used as a source for the synthesis of microcrystalline cellulose. Various plant fibers can be used for synthesis of MCC. Sisal is one such plant used for MCC

synthesis. Investigations are reported on synthesis of MCC from sisal fibers [76]. Ropes, cordages, and nets are prepared from the sisal fibers. Application of these fibers for such materials is practiced since long ago. Use of raw material depends on the availability and cost. In countries like Bangladesh, local raw material *Bombax ceiba* L. known as shimul-tula is found everywhere [77]. Vora and Shah, in their investigation, used corn husk as a raw material [78]. They carried out acid and alkali treatment followed by bleaching with sodium hypochlorite. Suryadi et al. used water hyacinth powder as a raw material for MCC synthesis [79]. In enzymatic hydrolysis, they optimized the hydrolysis time. Achor et al. used dried bark of the fruit of the plant *Lageriana siceraria* for MCC synthesis [80]. Swantomo et al. explored use of waste cotton fabrics for synthesis of microcrystalline cellulose [81]. These materials were obtained from tailoring and shredding activities. Microcrystalline cellulose synthesis from coconut fiber was reported by Nasution et al. [82]. Bleached Kraft bagasse and bleached soda rice straw pulps were used as a raw material for MCC by Hassan and El-Sakhawy [83]. They prepared bleached cotton stalks pulp by pulping cotton stalks with sodium hydroxide and bleached with sodium hypochlorite. Raw oil palm empty fruit bunch (REFB) fiber was used for MCC by Junadi et al. [84]. Lembang plant (*Typha angustifolia* L.) was a source of MCC in investigation carried out by Adawiyah et al. [85]. Rizka et al. used cotton waste from local cotton mill for MCC preparation [86]. First it was cleaned from dirt, leaves, roots branches, etc. and then fed to cotton selector machine to obtain cotton lint. In Asian countries, jute fiber or jute stick is an easily available raw material for MCC [87, 88]. Many agricultural raw materials, cotton linters, and plant part can be used for MCC synthesis with more or less modifications in heating methods [89–92]. Bacterial cellulose is also reported as a raw material for MCC [93]. Betung bamboo (*Dendrocalamus asper*) was used for MCC with extraction methods namely (1) decoction extraction, (2) maseration with ethanol, and (3) maseration with ethanol:n-hexane (2:1) [94]. Murigi et al. compared the microcrystalline cellulose synthesis from Kenyan Biomass materials namely banana stem, rice straws, water hyacinth, and papyrus reeds [95]. Flowability of banana stem MCC was the highest and least for papyrus reeds MCC. In an investigation involving rice husk, Ahmad et al. observed that 2 M nitric acid resulted in 83% MCC yield while 1 M, 80%, and 1 and 2 M hydrochloric acid resulted in 60 and 69% yield respectively [96]. Crystallinity index of 2 M nitric acid–treated MCC was 63.9% compared to other acids [96]. Investigations are also reported on utilization of waste papers, hardwood, fly ash, bean hulls, and grass as raw material for MCC [97–99]. Many investigations are reported on methods to form composite material to take advantage of MCC properties and remove drawbacks of conventional materials like poor mechanical properties, hydrophobicity, and surface morphology [100–106]. Figure 1 depicts the raw materials used for

MCC synthesis. Composition of some selective raw materials is summarized in Table 1.

3 Synthesis methodologies

The use of extracting method for micro cellulose depends on the amount cellulose in the raw material and properties of the products obtained. Micro cellulose from renewable sources is gaining importance due to environmental concerns. Synthesis of MCC consists of a separation of lignin and then extraction of hemicelluloses by bleaching and

washing. In the experiments conducted by Singh et al., sisal fibers were washed with water repeatedly and then dried at 353 K for one day [76]. Then the fibers were chopped to 3–6 mm and then subjected to caustic treatment at 353 K for 240 min. Residual alkali was removed by washing. Hydrogen peroxide was used as a bleaching agent and it was carried out at 328 K for 60 min at pH value ranging from 10 to 11. In the preparation of MCC from *Bombax ceiba* L., alpha cellulose preparation from bamboo cotton is followed by treatment with hydrochloric acid. After heating this sample at 100 °C and cooling to room temperature, the obtained alpha cellulose is washed with water to remove the acid [77].
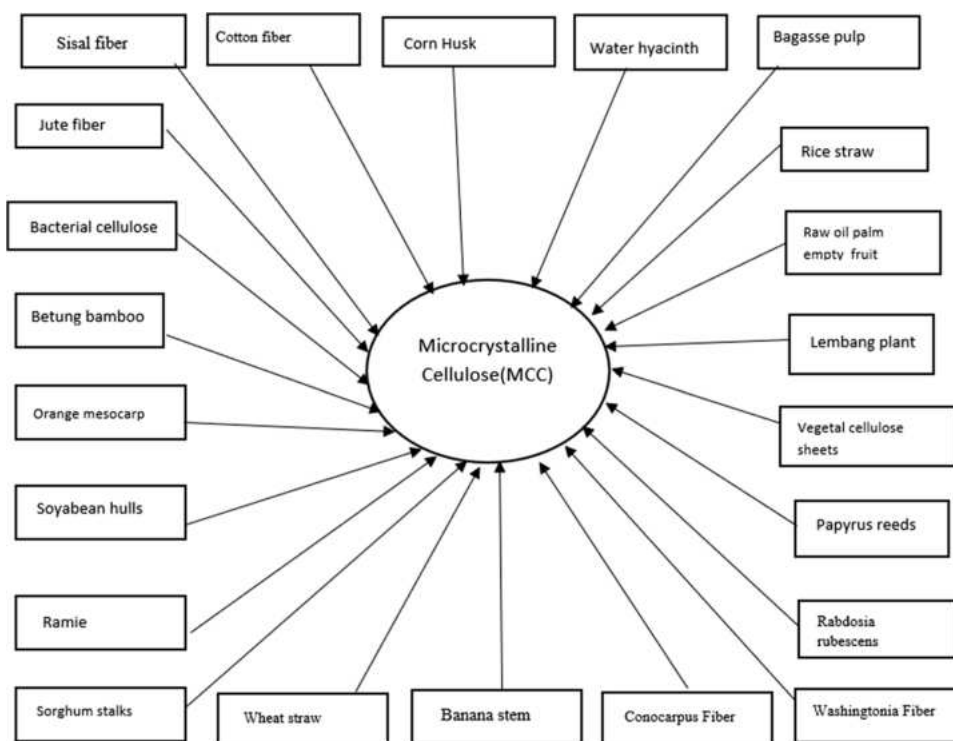

Fig. 1 Raw materials for MCC

Table 1 Raw material composition

Source	Cellulose %	Lignin %	Hemicelluloses % /holocellulose	Wax %/ash %	Moisture %/ash%	Other
Sisal fibers [76]	50–74	8–11	10–14 hemicelluloses	2	2–4 moisture	1% pectin
Pretreated cotton [77]	___	___	___	___	5–6 moisture	___
Coconut fiber [82]	44.2	20.5	56.3 holocellulose	2.2 ash	___	___
Bagasse-bleached pulp [83]	77.6 (alpha cellulose)	0.84	21.4 hemicelluloses	___	1.3 ash	___
Cotton stalks bleached pulp [83]	75.1 (alpha cellulose)	0.94	19.3 hemicelluloses	___	1.3 ash	___
Rice straw bleached pulp [83]	71.2 (alpha cellulose)	1.32	17.4 hemicelluloses	___	13.8 ash	___
Jute stick fiber [87]	65.8	14.67	18 hemicellulose	___	0.65 ash	0.3 pectin
Rice husk [96]	___	___		___	___	Crystallinity index 39%
Washingtonia trunk spine raw fibre [105]	41 (alpha cellulose)	21	21 hemicellulose	___	___	___

For obtaining MCC from corn husk, the material is pulverized to the powder. Sodium hydroxide is used to delignify it. Then it is treated with acids and distilled, and washed repeatedly until neutral pH was obtained. Drying happens to be the last process in the sequence to obtain MCC [78]. In their work, oil palm trunk, and stem of water hyacinth were used for microorganism synthesis by Suryadi et al. [79]. Achor et al. used dried bark of the fruit of the plant *Lageriana siceraria* for MCC synthesis [80]. The treatment with sodium hydroxide, acid, and hypochlorite washing yielded alpha cellulose. The alpha cellulose was acid hydrolyzed, filtered, and dried to obtain product [80].

The synthesis of MCC from waste cotton, which was disintegrated using 35% hydrogen peroxide for 120 min at 363 K, was irradiated in a Gamma Chamber-40 [81]. Washing and grounded yielded the final product. Nasution et al., for obtaining MCC from coconut fibers, used nitric acid instead of commonly used hydrochloric acid to obtain alpha cellulose [82]. For the preparation of the MCC from agricultural waste, bleached pulp obtained from waste was hydrolyzed with distilled water and washed. In the application of ultrasound for extraction of MCC from alpha cellulose (raw oil palm empty fruit bunch fiber), Junadi et al. soaked the cellulose in 10% sodium hydroxide (1:25 ratio) followed by ultrasonic treatment, and then repeatedly ultrafiltered [84]. The resultant MCC had 81% crystallinity compared to 45–54% (REFB and cellulose). Ultrasound-assisted synthesis exhibited 53% increase in the crystal size of REFB. In the process of obtaining MCC from cotton waste from mills, the cotton lint is first treated with sodium hydroxide solution and bleached with hydrogen peroxide [86]. This is followed by usual steps of acid hydrolysis and dewatering/drying. The heating of the sample required post hydrolysis can be made more effective with microwave heating [88]. Two stage hydrolysis in MCC synthesis yields better results than single stage [88–90]. Figure 2 describes the common steps involved in MCC synthesis.

4 Characterization Methods and Analysis

The characterization includes particle size analysis, Fourier transform infrared spectrophotometer (FTIR) analysis, Gravimetric analysis, X-ray diffraction meter analysis, scanning electron microscopy, and water retention time

[76]. The particle size of MCC derived from sisal fiber was more (14 μM) than commercial MCC (10.5 μM). FTIR studies were used to characterize lignin present, indicated by peaks at 1500^{-1}, 1600 cm^{-1}. Absence of transmittance bands (1500^{-1}, 1600 cm^{-1}) indicates absence of lignin in MCC. Based on analysis of the intensity bands, it can be inferred that due to removal of amorphous cellulose, C–OH, C–O–C, and C–C bonds were exposed, increasing stretching absorbency. The decomposition of sisal fibers starts at higher temperature than the sisal MCC and commercial MCC. This confirms the presence of higher quantity of hemicelluloses or lignin in sisal fibers [76]. X-ray diffraction analysis confirms the higher crystallinity of MCC than sisal fibers. Water retention value of sisal MCC was 1.4 times higher than commercial MCC. Scanning electron microscope studies indicate that the sisal MCC was fibrous with good length-to-diameter ratio. The analysis of the MCC obtained from bamboo cotton indicated that the moisture content was 5%, below the 8% stated in British Pharmacopoeia, 1993. Interparticle friction is indicated by Hausner ratio whereas Carr's index indicates the compressibility of a powder. Internal and cohesive force assessment is indicated by angle of repose. Carr's index below 16 indicates good flowability and above 35 indicates cohesiveness. Hausner ratio above 1.25 is desirable for flow properties [77]. The analysis of spectra for cotton MCC indicated the characteristic intermolecular and intramolecular OH stretching vibration band. The analysis also indicates the removal of lignin effectively in chemical treatment. Gravimetric analysis indicated that only 0.59% residue was present in the synthesized MCC from bamboo cotton fibers. The corn husk MCC indicated good structural and thermal stability with satisfactory crystallinity as shown in Table 1. Water hyacinth MCC showed crystalline characteristic similar to microcrystalline cellulose reference (Avicel pH 101) [79]. Results of investigation by Achor et al. indicate that the MCC obtained from back of the fruit of *Lageriana siceraria* (water gourd) had better water absorption and retention capacity than Avicel 101 [80]. They obtained 29% yield of MCC from this raw material. The MCC obtained by using waste cotton was having properties similar to commercial MCC. The crystallinity of irradiated cotton fabric MCC was better

Fig. 2 Steps in MCC synthesis from raw feedstock
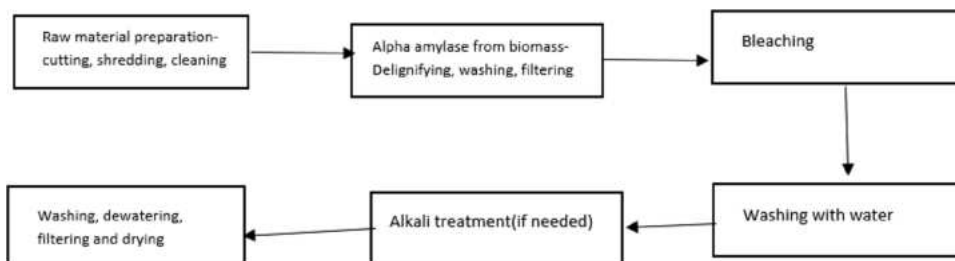
(70.8%) compared to cotton fabric [6]. The MCC by ultrasound-assisted extraction had 81% crystallinity compared to 45–54% (REFB and cellulose [84]. Lembang (*Typha angustifolia* L.) MCC synthesis indicated that the use of strong acid increases the mechanical properties of the resultant MCC [81]. In their work, Rizka et al. studied the bleaching process with various bleaching agent strength [86]. Alpha cellulose yield increases from 87 to 90%, for 5 to 30% increase in the bleaching agent concentration. So 5% is optimum concentration. Optimum temperature was 96 °C for MCC hydrolysis. At lesser temperature, some moisture is retained, and at higher, formation of sugar of glucose or polysaccharide takes place due to hydrolysis of cellulose chain and cleavage of beta-1–2 glycosidic bonds. Bhandari et al. studied zeta potential values for jute fiber MCC [87]. Agglomeric tendency in water is indicated by negative zeta potential. Murigi et al. compared the microcrystalline cellulose synthesis from Kenyan biomass materials namely banana stem, rice straws, water hyacinth, and papyrus reeds [95]. They observed that flowability of banana stem MCC was highest and least for papyrus reeds MCC. Bulk and tapped densities of water hyacinth MCC were highest and least for papyrus reeds MCC. Also according to this investigation, rice straw MCC was thermally stable compared to banana stem, water hyacinth, and papyrus reeds. Most of the investigation on MCC is focused on efficient MCC isolation procedures, treatments, and drying [96, 99]. Synthesis from *Rabdosia rubescens* residue was reported with an impressive yield of 88–95% [95]. In their investigation on MCC synthesis from *Rabdosia rubescens* residue, Li et al. considered three important factors namely hydrogen chloride (HCl) concentration (A), reaction temperature (B), and hydrolysis time (C). This investigation emphasized the importance of HCl strength which acts as a solvent and acid catalyst. Hydrolysis needs energy but a very high energy level results in the breaking of glycosidic bonds and a reduction in MCC content due to glucose formation [99]. The characterization details are explained in Table 2. Properties and applications of MCC derived from various raw materials are depicted in Fig. 3.

5 Application-Oriented Research on MCC

Modification of MCC and complexing with other materials results in application-oriented product with a desired product. Dimitrov et al. investigated Fe_3O_4 for modification of MCC to form composite material [100]. Surface-bonded magnetite was produced with Fe^{+2}/Fe^{+3}. Polyurethane polymer and magnetite MCC were cross-linked to yield composite product. Analysis of the product indicated the presence of nanosized magnetite. The water absorption capacity indicated that composite was suitable for water environment.

Also it had higher electrical conductivity. MCC with required properties in terms of size, crystallinity, and physicochemical properties is synthesized by maintaining required conditions [101]. Conventional chemical methods produce a MCC that has hydrophilic sulfate surface chemistry. This puts limitations on its application. Enzymatic synthesis of cellulose nanocrystals and microcrystalline cellulose has been reported with better properties [102]. MCC can be used for composite film in medical materials for reducing pathogenic activities [103, 107, 108]. Conventionally fish gelatin is used for this purpose with limitation of low mechanical strength. MCC/fish gelatin composite has better mechanical properties than original material. Date palm fiber (*Phoenix dactylifera* L.) MCC was modified to nanocrystalline cellulose by Hachaichi et al. [104]. Nanocrystalline cellulose thus obtained had a crystallinity index 71% and excellent mechanical properties [104]. Figure 3 depicts characteristics and applications of MCC in various fields. Tarchoun et al. used chlorine free delignification for giant reed [109]. The peaks obtained in FTIR analysis were very close to those for commercial MCC. The crystallinity index ranged from 73 to 80%. The author has also used oceanica brown algae for MCC synthesis [110]. The crystallinity obtained was 60 to 75%. Various natural resources are being explored and examined by investigators for cost effective, environment friendly synthesis of MCC with customized properties for various applications [109–114].

6 Discussion and Conclusion

Microcrystalline cellulose is synthesized from raw feedstock with a methodology involving alkali treatment, acid hydrolysis, and dewatering. Being microcrystalline in structure, the characterization for its size, strength, crystallinity, pH, crystal size, stability, and flow properties is an important factor deciding the suitability of the material for specific applications. The yield obtained for the synthesis of MCC from coconut fiber was 43% [82]. In most of the investigations, the crystallinity index obtained was above 60%. The resulting alpha cellulose had 47% crystallinity and MCC, 75%. The agricultural residues (bleached pulp of bagasse, cotton stalks, and rice straw) indicated that rice straw MCC had greater tensile strength. Negative effect of wet granulation was reduced due to presence of silica in raw materials [83]. Use of strong acid during synthesis increases mechanical properties of MCC [81]. Eighty to 85% yield is reported for jute stick and jute fiber MCC [87, 88]. The MCC yield reported from jute stick varied from 25 to 33% depending on treatment [91]. A mixture of n-hexane solvent:ethanol (2:1) resulted in maximum 15.05% yield of MCC compared to decoction extraction and maseration with ethanol [94]. Bulk and tapped

Table 2 Characterization of MCC

Raw material	pH	Angle of repose/crystal size	Crystallinity index	Other index/moisture content/other
Sisal MCC [76]	___		81.5	___
Cotton MCC [77]	6–7	Angle of repose 32–37°		Carr's index 29–36% and Hausner ratio 1.3–1.5, moisture content 5–6%
Corn Husk MCC [78]	6.8	Angle of repose 34–37°	79	Carr's index 16–20% Hausner ratio 1.2–1.25, moisture content 4%
Water hyacinth MCC [79]	___	___	70	
Back of the fruit of *Lageriana siceraria* (water gourd) MCC [80]	6.8	Angle of repose 32.9°	___	Carr's index 23.5% and Hausner ratio 1.31
Waste cotton fibers (gamma radiation treatment) MCC [81]	5	___	___	Loss on drying, 5–6%, bulk density 1.2–1.27, polymerization 122–133%
Coconut fiber MCC [82]	7	___	75	Loss on drying, 5%,
Bagasse bleached pulp MCC [83]	___	___	76	___
Cotton stalks bleached pulp [11]	___	___	77	Yield 90% for alpha cellulose and 75% for MCC
Rice straw bleached pulp MCC [83]	___	___	78	
Raw oil palm empty fruit bunch (REFB) fiber MCC [84]	___	Crystal size 17.09 A	81	Decomposition temperature, 314 °C
Lembang plant (*Typha angustifolia* L.) MCC [85]	___	Crystal size 2.4 nm	71.1	Decomposition temperature, 353 °C 13.61% weight loss
Jute fiber [16]	___	Crystal size 6.9 nm	60	
Oil palm empty fruit brunch fiber MCC [92]	___	___	___	Yield 22%
Bacterial cellulose MCC [93]	___	An average particle size between 70 and 90 nm	69	___
Vegetal cellulose (VC) sheets produced from bleached Kraft eucalyptus pulp MCC [93]	___	Size smaller than 30.0 μm	88	___
Betung bamboo (*Dendrocalamus asper*) MCC [94]	6.88	Angle of repose 31.39°, Size 150 to 240 nm	___	Carr's index 31 to 34%, yield, Hausner ratio 1.45, 53.6%, moisture content 4.36%, yield 15.05%
Banana stem MCC [95]	___	___	___	Carr's index 16.63, Hausner's ratio 1.19, yield 18.35%
Rice straws MCC [95]	___	___	___	Carr's index 28.93, Hausner's ratio 1.41, yield 19.62%
Water hyacinth MCC [95]	___	___	___	Carr's index 22.56, Hausner's ratio 1.29, yield 23.39%
Papyrus reeds MCC [95]	___	___	___	Carr's index 56.01, Hausner's ratio 2.28, yield 23.63%
Rice husk MCC [96]	___	___	63.9	
Rabdosia rubescens residue [99]	___	___		Yield 88%
Washingtonia fiber MCC [105]	___	___	82.9	Yield 72.6%
Conocarpus fiber MCC [106]	___	___	72.7	___
Giant reed MCC [109]	___	___	73–80	___
Oceanica brown algae [110]	___	Average diameter 8.4 ± 2.1 μm	60–75	___

densities of water hyacinth MCC were highest and least for papyrus reeds MCC. Also according to this investigation, Rice straw MCC was thermally stable compared to banana stem, water hyacinth, and papyrus reeds.

Various modifications in terms of alkali, acid, and dewatering methods are explored for effective synthesis with desired characteristics. Also application-oriented research include the combination of MCC with polymers to get

Fig. 3 Properties and applications of MCC
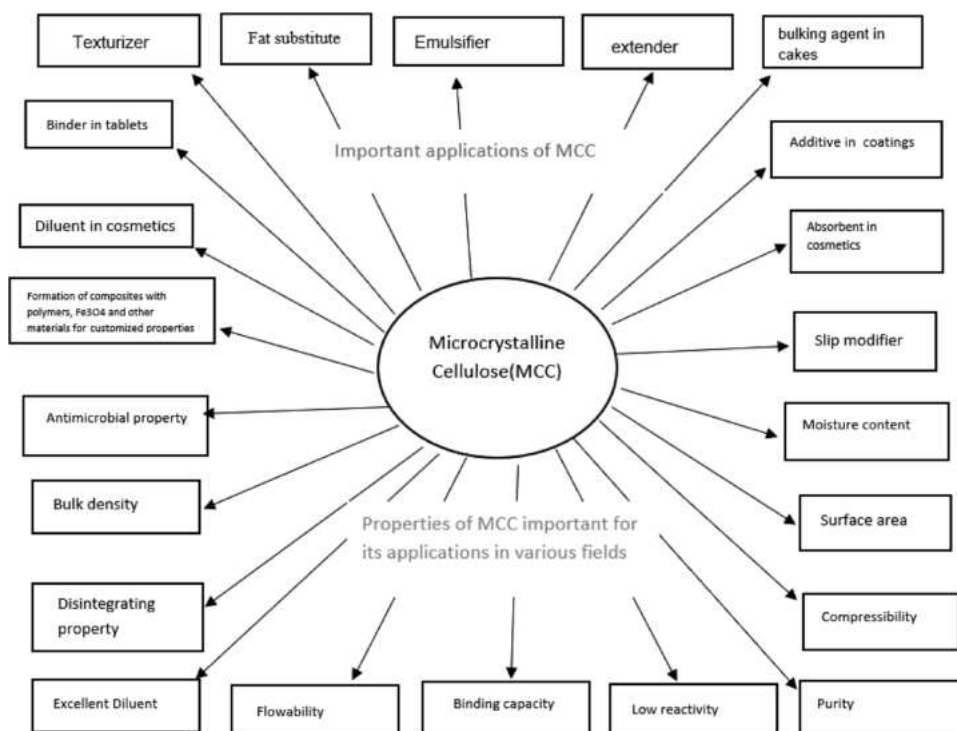
better and customized materials. Chlorine-free delignification provides environment friendly process. The properties of microcrystalline material depends on the synthesis conditions and starting material. From this review, it can be concluded that the MCC obtained various raw feedstocks has the properties very close to the commercial MCC.

Data Availability No additional data and materials are associated with this article to support the findings of the article.

Declarations

Ethics Approval and Consent to Participate Not applicable.

Consent for Publication Not applicable.

Competing Interests The authors declare no competing interests.

References

1. Klemm, D., Philipp, B., Heinze, T., Heinze, U., Wagenknecht, W. (1998). Comprehensive cellulose chemistry. *Volume 1: Fundamentals and Analytical Methods* WILEY-VCH Verlag GmbH, Weinheim ISBN: 3–527–29413–9

2. Trachea, D., Hazwan Hussinb, M., Tan Hui Chuinb, C., Sabarc, S., Nurul Fazitad, M. R., Taiwod, O. F. A., Hassand, T. M., & Mohamad Haafizd, M. K. (2016). Microcrystalline cellulose: Isolation, characterization and bio-composites application—A review. *International Journal of Biological Macromolecules, 93*, 789–804.

3. Shokri, J., & Adibkia, K. (2013). Application of cellulose and cellulose derivatives in pharmaceutical industries. In T. a. de Ven, & L. Godbout (Eds.), *Cellulose - Medical, Pharmaceutical and Electronic Applications*. IntechOpen.https://doi.org/10.5772/55178

4. Frohoff-Hülsmann, M.A., Lippold, B.C., McGinity, J.W. (1999). Aqueous ethyl cellulose dispersion containing plasticizers of different water solubility and hydroxypropyl methyl-cellulose as coating material for diffusion pellets II: properties of sprayed films.*European Journal of Pharmaceutics and Biopharmaceutics*, *48*(1), 67-75. https://doi.org/10.1016/s0939-6411(99)00023-5. PMID: 10477331.

5. Hossein, Z., Thomas, E. N., Louis, A. L. (2005). Why infusion and not microcapsules or other controlled release Methods?, Editor(s): D.R. Karsa, R.A. Stephenson, In Woodhead Publishing Series in *Food Science, Technology and Nutrition, Encapsulation and Controlled Release*, Wood head Publishing, 117–130, ISBN 9781855738201.https://doi.org/10.1533/9781845698218. 117

6. Thakur, V. K., & Voicu, S. I. (2016). Recent advances in cellulose and chitosan-based membranes for water purification: A concise review. *Carbohydrate Polymers, 146*, 148–165. https://doi.org/10.1016/j.carbpol.2016.03.030

7. Brown, R.M. (1990). Algae as tools in studying the biosynthesis of cellulose, nature's most abundant macromolecule. In: Wiessner, W., Robinson, D.G., Starr, R.C. (eds) *Cell Walls and Surfaces, Reproduction, Photosynthesis. Experimental Phycology*,

vol 1. Springer, Berlin, Heidelberg.https://doi.org/10.1007/978-3-642-48652-4_2

8. Brunton, L. L., Lazo, J. S., & Parker, K. L. (2006). Goodman and Gilman's the pharmacologic basis of therapeutics. *Goodman and Gilman's the Pharmacologic Basis of Therapeutics, 1*, 1–2021.

9. Seddiqi, H., Oliaei, E., Honarkar, H., et al. (2021). Cellulose and its derivatives: Towards biomedical applications. *Cellulose, 28*, 1893–1931. https://doi.org/10.1007/s10570-020-03674-w

10. Abe, K., Nakatsubo, F., & Yano, H. (2009). High-strength nanocomposite based on fibrillated chemi-thermomechanical pulp. *Composites Science and Technology, 69*, 2434–2437. https://doi.org/10.1016/j.compscitech.2009.06.015

11. Abraham, E., Weber, D. E., Sharon, S., Lapidot, S., & Shoseyov, O. (2017). Multifunctional cellulosic scaffolds from modified cellulose nanocrystals. *ACS Applied Materials & Interfaces, 9*, 2010–2015. https://doi.org/10.1021/acsami.6b13528

12. Agoda-Tandjawa, G., Durand, S., Berot, S., Blassel, C., Gaillard, C., Garnier, C., & Doublier, J. L. (2010). Rheological characterization of micro fibrillated cellulose suspensions after freezing. *Carbohydrate Polymers, 80*, 677–686. https://doi.org/10.1016/j.carbpol.2009.11.045

13. Kumari, N., & Kumar, K. (2018). Efficacy of composites for fabrication of orthotic calipers. In R. Somashekar, & T. Urs G. (Ed.), *Emergent Research on Polymeric and Composite Materials*(267–286) IGI Global. https://doi.org/10.4018/978-1-5225-3023-7.ch012

14. Ramdani, N., & Azibi, M. (2018). Properties enhancement of polymer/ceramic nanocomposites: Polymer nanocomposites. In R. Somashekar, & T. Urs G. (Ed.),*Emergent Research on Polymeric and Composite Materials, 99*–121. IGI Global. https://doi.org/10.4018/978-1-5225-3023-7.ch004

15. Lin, D., Liu, Z., Shen, R., Chen, S., & Yang, X. (2020). Bacterial cellulose in food industry: Current research and future prospects. *International Journal of Biological Macromolecules, 158*, 1007–1019. https://doi.org/10.1016/j.ijbiomac.2020.04.230

16. Choi, S.M., Rao, K.M., Zo, S.M., Shin, E.J., Han, S.S. (2022). Bacterial cellulose and its applications. *Polymers (Basel), 8*, 14(6), 1080 https://doi.org/10.3390/polym14061080.

17. Feng, X., Ullah, N., Wang, X., Sun, X., Li, C., Bai, Y., Chen, L., Li, Z. (2015). Characterization of bacterial cellulose by Gluconacetobacter hansenii CGMCC 3917. *Journal of Food Science* 80(10), 2217–27.https://doi.org/10.1111/1750-3841.13010. Epub 2015 Sep 9. Erratum in: *Journal of Food Science* 2019 Jul;84(7):2003. PMID: 26352877

18. Gomes, R,J., Ida, E.I., Spinosa, W.A. (2022). Nutritional supplementation with amino acids on bacterial cellulose production by Komagataeibacter intermedius: Effect analysis and application of response surface methodology. *Biotechnology and Applied Biochemistry*, *194*(11)5017–5036

19. Kaczmarek, M., Jędrzejczak-Krzepkowska, M., Ludwicka, K.(2022). Comparative analysis of bacterial cellulose membranes synthesized by chosen *Komagataeibacter*strains and their application potential. *International Journal of Molecular Sciences,* 23(6), 3391. https://doi.org/10.3390/ijms23063391

20. Xie, Y., Qiao, K., Yue, L., Tang, T., Zheng, Y., Zhu, S., Yang, H., & Fang, Z. (2022). A self-crosslinking, double-functional group modified bacterial cellulose gel used for antibacterial and healing of infected wound. *Bioactive Materials, 17*, 248–260. https://doi.org/10.1016/j.bioactmat.2022.01.018

21. Osorno, D. M., & Castro, C. (2018). Cellulose application in food industry: A review. In R. Somashekar, & T. Urs G. (Ed.), *Emergent Research on Polymeric and Composite Materials* 38–77 IGI Global. https://doi.org/10.4018/978-1-5225-3023-7.ch002

22. Rashid, S. and Dutta, H. (2022). Industrial applications of cellulose extracted from agricultural and food industry wastes. In *Handbook of Biomass Valorization for Industrial Applications* (eds Shahid-ul-Islam, A.H. Shalla and S.A. Khan).https://doi.org/10.1002/9781119818816.ch18

23. Kulkarni, S. J. (2016). Downstream processing in biotechnology: Research and studies. *International Journal of Science and Healthcare Research, 1*(3), 8–10.

24. Tothill, I. E., & Seal, K. J. (1993). Biodeterioration of waterborne paint cellulose thickeners. *International Biodeterioration & Biodegradation, 31*(4), 241–254. https://doi.org/10.1016/0964-8305(93)90020-3

25. Tothill, I. E., Best, D. J., & D.J., K.J. Seal, K.J. (1988). The isolation of Graphium putredinis from a spoilt emulsion paint and the characterisation of its cellulase complex. *International Biodeterioration and Biodegradation, 24*(45), 359–365. https://doi.org/10.1016/0265-3036(88)90021-8

26. Olayide, O.F., Ayomikun, K.E., Temitope, F.O. (2022). A first report on the identification of a novel archaea, Methanospirillum lacunae from spoilt paints in Lagos, Nigeria using a metagenomic approach. *Scientific African*, 15 https://doi.org/10.1016/j.sciaf.2021.e01029

27. Kulkarni, S. J. (2017). Environment friendly synthesis of colour, pigment and dyes: A review. *International Journal of Research and Review, 4*(4), 19–23.

28. Da Silva, V. Q. (2003). Microbial deterioration of paints. *Microbiologist, 4*(1), 43.

29. Odokuma, L. O., Berebon, D. P., & Ogbonna, C. B. (2013). Potential biodeteriogens of indoor and outdoor surfaces (coated with gloss, emulsion and textcoat paints). *IOSR Journal of Pharmacy and Biological Sciences 7*(1), 12.

30. Obidi, O. F., Aboaba, O. O., Makanjuola, M. S., & Nwachukwu, S. C. U. (2009). Microbial evaluation and deterioration of paints and paint-products. *Journal of Environmental Biology, 30*(5), 835.

31. Botta, C., & Cocolin, L. (2012). Microbial dynamics and biodiversity in table olive fermentation: Culture-dependent and independent approaches. *Frontiers in Microbiology, 3*, 245.

32. Dong, X., Zhang, Z.L., Zhao, Y.Y., Li, D., Wang, Z.L., Wang, C., Song, F., Wang, X.L. & Wang, Y.Z. (2022) Bio-inspired non-iridescent structural coloration enabled by self-assembled cellulose nanocrystal composite films with balanced ordered/disordered arrays. *Composites Part B: Engineering, 229*,10945610.https://doi.org/10.1016/j.compositesb.2021.109456

33. Siro, I., & Plackett, D. (2010). Microfibrillated cellulose and new nanocomposite materials: A review. *Cellulose, 17*, 459–494.

34. Klemm, D., Kramer, F., Moritz, S., Lindstrom, T., Ankerfors, M., Gray, D., & Dorris, A. (2011). Nanocelluloses: A new family of nature-based materials. *Angewandte Chemie, International Edition., 50*, 5438–5466.

35. Eichhorn, S., Dufresne, A., Aranguren, M., Marcovich, E., Capadona, J., Rowan, S., Weder, C., Thielemans, W., Roman, M., Renneckar, S., et al. (2010). Review: Current international research into cellulose nanofibres and nanocomposites. *Journal of Materials Science, 45*, 1–33.

36. Dufresne, A. (2012). *Nanocellulose: From nature to high performance tailored materials. Walter de Gruyter: Berlin*, Germany. https://doi.org/10.1515/9783110254600/html

37. Xie, S., Zhang, X., Walcott, M., & Lin, H. (2018). Cellulose nanocrystals (CNCs) applications. A review. *Engineered Science, 2*, 4–16. https://doi.org/10.30919/es.1803302

38. George, J., & Sabapathi, N. (2015). Cellulose nanocrystals: Synthesis, functional properties, and applications. *Nanotechnology, Science and Applications, 8*, 45. https://doi.org/10.2147/NSA.S64386

39. Zope, G., Goswami, A. & Kulkarni, S. (2022). Isolation and characterization of cellulose nanocrystals produced by acid hydrolysis from Banana Pseudostem. *BioNanoScience*, 12 https://doi.org/10.1007/s12668-022-00960-8

40. Berumen, P., & Catalina. (2021). Cellulose nanocrystals: Obtaining and sources of a promising bionanomaterial for advanced applications. *Biointerface Research in Applied Chemistry, 11*(11797), 11816. https://doi.org/10.33263/BRIAC 114.11797118

41. Abe, K., & Yano, H. (2009). Comparison of the characteristics of cellulose microfibril aggregates of wood, rice straw and potato tuber. *In Cellulose*. https://doi.org/10.1007/ S10570-009-9334-9

42. Kulkarni, S., & J. (2021). Synthesis of various products from different feed stocks- An insight into application to biotechnology. *International journal of chemical synthesis and chemical reactions, 7*(2), 18–21.

43. Varanasi, P., Singh, P., Auer, M., Adams, P. D., Simmons, B. A., & Singh, S. (2013). Survey of renewable chemicals produced from lignocellulosic biomass during ionic liquid pretreatment. *Biotechnology for Biofuels, 6*(14), 1–9.

44. Bilal, M., Nawaz, M. Z., Iqbal, H. M. N., Hou, J., Mahboob, S., Al-Ghanim, K. A., & Cheng, H. (2018). Engineering ligninolytic consortium for bioconversion of lignocelluloses to ethanol and chemicals. *Protein and Peptide Letters, 25*(2), 108–119. https:// doi.org/10.2174/0929866525666180122105835

45. Zhu, P., Abdelaziz, O., Hulteberg, C., Riisager, A. (2019). New synthetic approaches to biofuels from lignocellulosic biomass. *Current Opinion in Green and Sustainable Chemistry*, 21 https:// doi.org/10.1016/j.cogsc.2019.08.005.

46. Becker, J., & Wittmann, C. (2019). A field of dreams: Lignin valorization into chemicals, materials, fuels, and health-care products. *Biotechnology Advances*, 37 https://doi.org/10.1016/j. biotechadv.2019.02.016

47. Sedlak, M., & Nancy, W. Y. H. (2004). Production of ethanol from cellulosic biomass hydrolysates using genetically engineered saccharomyces yeast capable of cofermenting glucose and xylose. *Applied Biochemistry and Biotechnology, 113–116*, 403–416.

48. Cameron, J. S. (2000). Practical haemodialysis began with cellophane and heparin: The crucial role of William Thalhimer (1884–1961). *Nephrology Dialysis Transplantation, 15*(7), 1086–1091. https://doi.org/10.1093/ndt/15.7.1086

49. Albers, J., Knop, K., & Kleinebudde, P. (2006). Brand-to-brand and batch-to-batch uniformity of microcrystalline cellulose in direct tableting with a pneumo-hydraulic tablet press. *La Pharmacie Industrielle, 68*, 1420–1428.

50. Koo, O. M. Y., & Heng, P. W. S. (2001). The influence of microcrystalline cellulose grade on shape and shape distributions of pellets produced by extrusion–spheronization. *Chemical & Pharmaceutical Bulletin, 49*, 1383–1387.

51. Landin, M., Vazquez, M. J., Souto, C., Concheiro, A., Gomezamoza, J. L., & Martinezpacheco, R. (1992). Comparison of 2 varieties of microcrystalline cellulose as filler-binders. 1. *Prednisone tablets. Drug Development and Industrial Pharmacy, 18*, 355–368.

52. Patel, S., Kaushal, A. M., & Bansal, A. K. (2006). Compression physics in the formulation development of tablets. *Critical Reviews in Therapeutic Drug Carrier Systems, 23*, 1–65.

53. Sherwood, B. E., & Becker, J. (1998). A new class of high functionality excipients: Silicified microcrystalline cellulose. *Pharmaceutical Technology, 22*, 183–194.

54. Thoorens, G., Krier, F., Leclercq, B., Carlin, B., & Evrard, B. (2014). Microcrystalline cellulose, a direct compression binder in a quality by design environment—A review. *International Journal of Pharmaceutics, 473*, 64–72.

55. Bhimte, N. A., & Tayade, P. T. (2007). Evaluation of microcrystalline cellulose prepared from sisal fibers as a tablet excipient: A technical note. *AAPS PharmSciTech, 8*(1), 1–6. https://doi.org/ 10.1208/pt0801008

56. Bolhuis, G. K., & Chowhan, Z. T. (1996). Materials for direct compaction. In G. Alderborn & C. Nystrom (Eds.), *Pharmaceutical Powder Compaction Technology* (pp. 419–500). Merkcel Dekker Inc.

57. Sonaglio, D., Battaille, B., Ortigosa, C., & Jacob, M. (1995). Factorial design in the feasibility of producing Microcel MC 101 pellets by extrusion/spheronization. *International Journal of Pharmaceutics, 115*, 53–60. https://doi.org/10.1016/0378-5173(94)00246-2

58. Rowe, R.C., Sheskey, P.J., Quinn, M.E. (2009). Formulation optimization utilizing D-optimal experimental design of oral capsules containing enteric-coated pellets of lansoprazole and *in vivo* bioequivalence. *Handbook of Pharmaceutical Excipients* 6th ed. American Pharmacist Association and Pharmaceutical Press, pp. 506–509

59. Thoorens, G., Fabrice, K., Bruno, L., Brian, C., Brigitte, E. (2014). Microcrystalline cellulose, a direct compression binder in a quality by design environment-A review. *International Journal of Pharmaceutics, 473*(1),64-7210. https://doi.org/10.1016/j. ijpharm.2014.06.055

60. Nicoleta, T., Ibbett, R., & Schuster, K. C. (2011). Overview on native cellulose and microcrystalline cellulose i structure studied by X-ray diffraction (WAXD): Comparison between measurement techniques. *Lenzinger Berichte, 89*, 118–131.

61. Chand, N., & Fahim, M. (2021). Natural fibers and their composites. *Tribology of Natural Fiber Polymer Composites (Second Edition)., 2021*, 1–59.

62. Suzuki, T., & Nakagami, H. (1999). Effect of crystallinity of microcrystalline cellulose on the compatibility and dissolution of tablets. *European Journal of Pharmaceutics and Biopharmaceutics., 47*, 225–230. https://doi.org/10.1016/s0939-6411(98) 00102-7

63. Shlieout, G., Arnold, K., & Muller, G. (2002). Powder and mechanical properties of microcrystalline cellulose with different degrees of polymerization. *AAPS PharmSci Tech., 3*(2), 45–84.

64. Chaerunisaa, A. Y. Sriwidodo, S., & Abdassah, M. (2019). Microcrystalline cellulose as pharmaceutical excipient. In U. Ahmad, & J. Akhtar (Eds.), *Pharmaceutical Formulation Design - Recent Practices.* IntechOpen https://doi.org/10.5772/intec hopen.88092

65. Azubuike, C.P., Okhamafe, A.O. (2012). Physicochemical, spectroscopic and thermal properties of microcrystalline cellulose derived from corn cobs. *International Journal of Recycling of Organic Waste in Agriculture*, 1(9), 1–7 https://doi.org/10.1186/ 2251-7715-1-9

66. Debnath, B., Haldar, D., Purkait, M. (2021). A critical review on the techniques used for the synthesis and applications of crystalline cellulose derived from agricultural wastes and forest residues. *Carbohydrate Polymers, 273* https://doi.org/10.1016/j. carbpol.2021.118537

67. Belali, N., Chaerunisaa, A., & Rusdiana, T. (2019). Isolation and characterization of microcrystalline cellulose derived from plants as excipient in tablet. A review. *Indonesian Journal of Pharmaceutics, 1*(2), 55–61. https://doi.org/10.24198/idjp. v1i2.21515

68. Boopasiri, S., Sae-Oui, P., & Siriwong, C. (2022). Fabrication of microcrystalline cellulose/zinc oxide hybrid composite by hydrothermal synthesis and its application in rubber compounding. *Journal of Applied Polymer Science, 139*(18), e52065. https://doi.org/10.1002/app.52065

69. Garba, Z. N., Lawan, I., Zhou, W., Zhang, M., Wang, L., & Yuan, Z. (2020). Microcrystalline cellulose (MCC) based materials as emerging adsorbents for the removal of dyes and heavy metals A review. *Science of The Total Environment, 717*, 135070. https://doi.org/10.1016/j.scitotenv.2019.135070

70. Liu, J., Chen, T., Yang, Y., Bai, Z., Xia, L., Wang, M., Lv, X., & Li, L. (2020). Removal of heavy metal ions and anionic dyes from aqueous solutions using amide-functionalized cellulose-based adsorbents. *Carbohydrate Polymers, 230*, 115619. https://doi.org/10.1016/j.carbpol.2019.115619

71. Kian, L. K., Jawaid, M., Ariffin, H., & Alothman, O. Y. (2017). Isolation and characterization of microcrystalline cellulose from roselle fibers. *International Journal of Biological Macromolecules, 103*, 931–940. https://doi.org/10.1016/j.ijbiomac.2017.05.135

72. Global Newswire(2022). Global microcrystalline cellulose (MCC) market to reach $1.5 billion by 2026,June 2022. https://www.reportlinker.com/p05899913/?utm_source=GNW

73. Petersson, L., & Oksman, K. (2006). Biopolymer based nanocomposites: Comparing layered silicates and microcrystalline cellulose as nanoreinforcement. *Composites Science and Technology, 66*(13), 2187–2196. https://doi.org/10.1016/j.compscitech.2005.12.010

74. Mamleev, V., Bourbigot, S., Le Bras, M., Yvon, J., & Lefebvre, J. (2006). Model-free method for evaluation of activation energies in modulated thermogravimetry and analysis of cellulose decomposition. *Chemical Engineering Science, 61*(4), 1276–1292. https://doi.org/10.1016/j.ces.2005.07.040

75. Colom, X., Carrasco, F., Pagès, P., & Cañavate, J. (2003). Effects of different treatments on the interface of HDPE/lignocellulosic fiber composites. *Composites Science and Technology, 63*(2), 161–169. https://doi.org/10.1016/S0266-3538(02)00248-8

76. Singh, G. P., Madiwale, P. V., & Adivarekar, R. V. (2017). Preparation and characterization of microcrystalline cellulose (MCC) from renewable source. *Current Applied Polymer Science, 1*(2), 152–158. https://doi.org/10.2174/2452271601666170721120343

77. Haque, S.M. & Chowdhury, A. & Rana, A. & Masum, M. & Ferdous, T.& Rashid, M. & Sarker, Mithun & Karim, M. (2015). Synthesis of microcrystalline cellulose from pretreated cotton obtained from Bombax ceiba L. and its characterization. *Bangladesh Journal of Scientific and Industrial Research, 50*(3),199–204 50. 199. https://doi.org/10.3329/bjsir.v50i3.25586

78. Vora R., and Shah, Y. (2017). Extraction, characterization of micro crystalline cellulose obtained from corn husk using different acid alkali treatment method. *Indo American Journal of Pharmaceutical Sciences*, *4*(08),2400–2409

79. Suryadi, H., Sutriyo, S., Hasty, S., & Rosikhoh, D. (2017). Preparation of microcrystalline cellulose from water hyacinth powder by enzymatic hydrolysis using cellulase of local isolate. *Journal of Young Pharmacists, 9*, s19–s23. https://doi.org/10.5530/jyp.2017.1s.6

80. Achor, M., Oyeniyi, Y., & J. and Yahaya, A. (2014). Extraction and characterization of microcrystalline cellulose obtained from the back of the fruit of Lageriana siceraria (water gourd). *Journal of Applied Pharmaceutical Science, 4*(01), 057–060.

81. Swantomo, D., Giyatmi, G., Adiguno, S. H., & Wongsawaeng, D. (2017). Preparation of microcrystalline cellulose from waste cotton fabrics using gamma irradiation. *English Journal., 21*(2), 173–182. https://doi.org/10.4186/ej.2017.21.2.173

82. Nasution, H., Harahap, H., Suherman, P. and Kelvin. (2018). Isolation and characterization of microcrystalline cellulose from coconut fiber using acid hydrolysis process. In *Proceedings of the International Conference of Science, Technology, Engineering, Environmental and Ramification Researches (ICOSTEERR 2018) - Research in Industry 4.0,* pp. 222–226. https://doi.org/10.5220/0010077802220226

83. Hassan, M.L., El-Sakhawy, M. (2005). Physical and mechanical properties of microcrystalline cellulose prepared from local agricultural residues. 8th Arab International Conference On Polymer Science & Technology 27 – 30 November 2005, Cairo-Sharm El-Shiekh, EGYPT

84. Junadi, N., Beg, M. D. H., Yunus, R. M., Ramli, R., Zianor, A., & Moshiul, A. K. M. (2019). Characterization of microcrystalline cellulose isolated through mechanochemical method. *Indian Journal of Fibre & Textile Research, 44*, 442–449.

85. Adawiyah, R., Suryanti V., and Pranoto. (2022). Preparation and characterization of microcrystalline cellulose from lembang (Typha angustifolia L), 6TH-ICAMBF-2021 Journal of Physics: Conference Series 2190 (2022) 012007 IOP Publishing https://doi.org/10.1088/1742-6596/2190/1/012007

86. Rizka, Y., Rr. Gustiani, S., Kasipah, C., Sukardan, M.D. (2020). Preparation of microcrystalline cellulose from cotton yarn spinning mills wastes: effect of pretreatment and hydrolysis reaction condition on the product characteristics, E3S Web of Conferences 148 https://doi.org/10.1051/e3sconf/202014

87. Ghosh, R.K., Ray, D.P., Chattopadhyay, Bhandari, S.N.K., Kundu, A., Tiwari, A., Das, I. (2018). A method for microwave assisted synthesis of microcrystalline cellulose from jute stick alpha cellulose. *International Journal of Agriculture, Environment and Biotechnology*, *11*(4), 4,697- 701 https://doi.org/10.30954/0974-1712.08.2018.12

88. Sarkar, S., Dilruba, F. A., Rahman, M., Hossen, M., Dayan, A. R., Khatton, A., Sarker, J., & Uddin, M. (2022). Isolation of microcrystalline alpha-cellulose from jute: A suitable and economical viable resource. *GSC Biological and Pharmaceutical Sciences, 18*(03), 219–225. https://doi.org/10.30954/0974-1712.08.2018.12

89. Bhakare, A. B., Bhalekar, S. S., Salvi, V. R., & Kulkarni, S. J. (2021). Synthesis of microcrystalline cellulose from raw feed stock A review. *International Journal of Advance Research and Innovation, 9*(1), 37–39.

90. Jeevananda, T., & Siddharamaiyya. (1997). Synthesis and characterization of microcrystalline cellulose powder. *India Journal of Material and Engineering Sciences, 4*, 38–40.

91. Bhandari, K., Roy, P., Bhattacharyya, A. R., & Maulik, S. R. (2020). Synthesis and characterization of microcrystalline cellulose from jute stick. *Indian Journal of Fibre & Textile Research, 45*, 464–469.

92. Soom, R. M., Aziz, A. A., Hassan, W. H. W., & Top, A. B. M. (2009). Solid state characteristics of microcrystalline cellulose from oil palm empty fruit bunch fibre. *Journal of Oil Palm Research, 21*, 613–620.

93. Rafael, O., Hernane, B., Rosana, A., Carla, M., Geandre, C., Guimes, F., Younes, M., & Sidney, R. (2011). Synthesis and characterization of microcrystalline cellulose produced from bacterial cellulose. *Journal of Thermal Analysis and Calorimetry, 106*, 703–709. https://doi.org/10.1007/s10973-011-1449-1

94. Kharismi and Suryadi (2018). MCC from D. asper through acid hydrolysis. *Journal of Young Pharmacists,* 10(2) 79-83 https://doi.org/10.5530/jyp.2018.2s.15

95. Murigi, M. K., Madivoli, E. S., Mathenyu, M. M., Kareru, P. G., Gachanja, A. N., Njenga, P. K., Nowsheen, G., Githira, P. N., Mercy, G. (2014). Comparison of physicochemical characteristics of microcrystalline cellulose from four abundant Kenyan biomasses. *IOSR Journal of Polymer and Textile Engineering (IOSR-JPTE), 1*(2), 53–63

96. Ahmad, Z., Roziaizan, N. N., Rahman, R., Mohamad, A. F., Wan Ismail, W.I.N. (2016). Isolation and characterization of microcrystalline cellulose (MCC) from rice husk (RH). MATEC Web of Conferences, 2016. https://doi.org/10.1051/matecconf/20164705013

97. Trache, D., Hazwan Hussin, M., Chuin, C. T. H., Sabar, S., Nurul Fazita, M. R., Taiwo, O. F. A., Hassan, T. M., & Haafiz, M. K. M. (2016). Microcrystalline cellulose: Isolation, characterization and bio-composites application—A review. *International*

Journal of Biological Macromolecules, 93, 789–804. https://doi.org/10.1016/j.ijbiomac.2016.09.056

98. Valchev, I., Yavorov, N., & Todorova, D. (2020). Producing bleached microcrystalline cellulose by two-stage dilute acid hydrolysis. *Cellulose Chemistry and Technology, 54*(3–4), 259–264.

99. Li, M., Wei, T., Qian, C. *et al.* Preparation of microcrystalline cellulose from *Rabdosia rubescens* residue and study on its membrane properties. *Scientific Reports,* 11 18956 https://doi.org/10.1038/s41598-021-98645-x

100. Dimitrov, K. V., Herzog, M., & Nenkova, S. (2013). Fe$_3$O$_4$ modification of microcrystalline cellulose for composite materials. *American Journal of Chemistry, 3*(5), 140–147. https://doi.org/10.5923/j.chemistry.20130305.04

101. Ishikawa, T., Mukai, B., Shiraishi, S., Utoguchi, N., Fujii, M., Matsumoto, M., & Watanabe, Y. (2001). Preparation of rapidly disintegrating tablet using new types of microcrystalline cellulose (PH-M Series) and low substituted hydroxypropyl cellulose or spherical sugar granules by direct compression method1). *Chemical & Pharmaceutical Bulletin, 49*(2), 134–139.

102. Anderson, S. R., Esposito, D., Gillette, W., Zhu, J. Y., Baxa, U., & Mcneil, S. E. (2014). Enzymatic preparation of nanocrystalline and microcrystalline cellulose. *Tappi Journal, 13*(5), 35–42.

103. Pan, L., Li, P., & Tao, Y. (2020). Preparation and properties of microcrystalline cellulose/fish gelatin composite film. *Materials (Basel), 13*(19), 4370. https://doi.org/10.3390/ma13194370

104. Hachaichi, A., Kouini, B., Kian, L. K., Asim, M., Fouad, H., Jawaid, M., & Sain, M. (2021). Nanocrystalline cellulose from microcrystalline cellulose of date palm fibers as a promising candidate for bio-nanocomposites: Isolation and characterization. *Materials (Basel), 14*(18), 5313. https://doi.org/10.3390/ma14185313

105. Azum, N., Jawaid, M., Kian, L. K., Khan, A., & Alotaibi, M. M. (2021). Extraction of microcrystalline cellulose from Washingtonia fibre and its characterization. *Polymers, 13*, 3030. https://doi.org/10.3390/polym13183030

106. Fouad, H., Kian, L. K., Jawaid, M., Alotaibi, M. D., Alothman, O. Y., & Hashem, M. (2020). Characterization of microcrystalline cellulose isolated from Conocarpus fiber. *Polymers (Basel), 12*(12), 2926. https://doi.org/10.3390/polym12122926

107. Kumar, V., Devi, B.M., & Sudha, P. N. (2016). Synthesis, characterization and applications of nanochitosan/sodium alginate/microcrystalline cellulose film. *Journal of Nanomedicine & Nanotechnology*. 07 https://doi.org/10.4172/2157-7439.1000419

108. Tran, C. D., Duri, S., Delneri, A., & Franko, M. (2013). Chitosan-cellulose composite materials: Preparation, characterization and application for removal of microcystin. *Journal of Hazardous Materials, 252–253*, 355–366. https://doi.org/10.1016/j.jhazmat.2013.02.046

109. Tarchoun, A. F., Trache, D., Klapötke, T. M., et al. (2019). Eco-friendly isolation and characterization of microcrystalline cellulose from giant reed using various acidic media. *Cellulose, 26*, 7635–7651. https://doi.org/10.1007/s10570-019-02672-x

110. Tarchoun, A. F., Trache, D., & Klapötke, T. (2019). Microcrystalline cellulose from Posidonia oceanica brown algae: Extraction and characterization. *International Journal of Biological Macromolecules, 138*, 837–845. https://doi.org/10.1016/j.ijbiomac.2019.07.176

111. Trache, D., Tarchoun, A. F., Derradji, M., Hamidon, T. S., Masruchin, N., Brosse, N., Hussin, H. (2020). Nanocellulose: From fundamentals to advanced applications. *Frontiers in Chemistry, Sec. Polymer Chemistry. 8.* https://doi.org/10.3389/fchem2020.00392

112. Kasim, F. and Asben. (2022). Synthesis of microcrystalline cellulose at several variations in alpha-cellulose hydrolysis time from oil palm empty fruit bunches by microwave pretreatment. *IOP Conference Series: Earth and Environmental Science, 1059*, 012079. https://doi.org/10.1088/1755-1315/1059/1/012079

113. Trache, D., Tarchoun, A.F., De Vita, D., Kennedy, J.F. (2022). Posidonia oceanica (L.) Delile: A Mediterranean seagrass with potential applications but regularly and erroneously referred to as an algal species. *International Journal of Biological Macromolecules*, 122624 https://doi.org/10.1016/j.ijbiomac.2022.11.169

114. Bhandari, K., Adval, A., Bhattacharya, A., & Maulik, S. (2022). Synthesis of microcrystalline cellulose from carpenter waste and its characterizations. *Journal of Natural Fibers, 19*(6), 1975–1989. https://doi.org/10.1080/15440478.2020.1788688

Recycling of Rubber Scrap Tyres and Its Processes of the Utilization

Publisher: IEEE

Cite This

PDF

Prasad Chavhan ; Zeeshan Madre ; Vaibhav Gaikwad ; S J Kulkarni **All Authors**

Abstract

Document Sections

I. Introduction

II. Recycling of Rubber

III. Literature Survey

IV. Utilization Methods for Scrap Rubber and Its Byproduct

V. The Waste of The Future

Show Full Outline ▾

Abstract:
Solid waste treatment is becoming a critical issue for the environment. According to estimates, the amount of garbage produced globally would more than quadruple by 2050 and triple by 2100 compared to 2016. Tyres is an integral component of transportation facilities. Tyre production accounts for 70% of the production of natural and synthetic rubber. The requirement and production of rubber is ever increasing. India exported rubber scrap products worth 28.5 USD Million to the overseas market. Use of rubber waste and recycling practice can reduce environmental footprints. The amount of carbon dioxide is reduced by 323 pounds as a result of recycling. Numerous physical and chemical procedures that aim to recover materials, energy, or chemicals from used tyres can be used to recycle them and convert them into useful products. Various techniques are available and are being explored for tyre recycling. Rapidly increasing rubber demand and consumption calls for effective and flexible methods for recycling of rubber waste including tyres. Recycling can reduce 10 to 30 % virgin rubber demand. Improper dumping and storage of rubber waste adversely affects the hygienic condition of the area. Waste tyres serve as a breeding ground for more mosquitoes, which can spread disease. Large tyre stacks can pose fire risks, produce toxic acid fumes that are dangerous to human health, and leave behind a risky oily residue. One tyre has a lifespan of 50–60 years in atmospheric conditions and 1500–2000 years in water. If a tyre is burnt, soot and hazardous gasses such biphenyl,

More Like This

Automated Grading of PowerPoint Presentations Using Latent Semantic Analysis

3 authors:

Jyoti Borade Khalkar
GIT
6 PUBLICATIONS **28** CITATIONS

SEE PROFILE

Arvind W Kiwelekar
Dr. Babasaheb Ambedkar Technological University
98 PUBLICATIONS **424** CITATIONS

SEE PROFILE

Laxman D. Netak
Dr. Babasaheb Ambedkar Technological University, Lonere
56 PUBLICATIONS **274** CITATIONS

SEE PROFILE

International Information and
Engineering Technology Association
Advancing the World of Information and Engineering

Automated Grading of PowerPoint Presentations Using Latent Semantic Analysis

Jyoti G. Borade*, Arvind W. Kiwelekar, Laxman D. Netak

Department of Computer Engineering, Dr. Babasaheb Ambedkar Technological University, Lonere, Raigad 402103, India

Corresponding Author Email: jyoti.borade81@gmail.com

ABSTRACT

Manual grading of students' work takes a long time and it is stressful. Evaluator may be holistic or analytic, lenient or non-lenient, experienced or inexperienced; which leads to non-uniformity in the assessment. Therefore, it is essential to do the automated grading of students' work to overcome human inadequacies through uniform assessment and also, it reduces workload of human evaluators. A novel automatic grading of students' PowerPoint presentation skills using Latent Semantic Analysis (LSA) is proposed. Program is implemented in python to extract features corresponding to the text appearance, graphics, footer, and hyperlink from the PowerPoint presentations. PowerPoint presentations are represented using feature vectors in the Latent Semantic Space using Singular Value Decomposition (SVD). SVD reveals relationships between features and PowerPoint presentations. The grades for the students' PowerPoint presentations are evaluated by finding Cosine similarity with reference presentations or finding k number of nearest reference presentations. The grades of such reference or nearest presentations are used to grade students' presentations. Kneighbors classifier used to find nearest neighbors. Kneighbors and Cosine Similarity approach give 90.90% and 81.81% accuracy, respectively, while predicting the grades for the students' PowerPoint presentations.

1. INTRODUCTION

Automated grading is an emerging technology helpful to teachers and students. It reduces the paper load of teachers and assessment-related issues. Some teachers can give overall grades based on one good impression in particular aspects or slight inclination towards their favorite students. It may lead to inconsistencies and inaccuracies in the assessment. Grading of students' work provides feedback to students for enhancing work quality. Hence, there is a need of automated grading system [1, 2]. To grade various kinds of work like reviewing research articles, evaluating programming assignments, poetry, short and long responses, various automatic grading systems have been developed. Page and Paulus employed statistical techniques to relate writing style to grade in 1968, but they neglected actual text. Some researchers applied Natural Language Processing (NLP) to retrieve linguistic features from text and then evaluated it using a variety of machine learning (ML) techniques like Support Vector Machine (SVM), Multilayer Perceptron (MLP), and Linear and Logistic regression, K-nearest Neighbors (KNN), Decision Tree (DT), and Random Forest (RF). Some have designed automated grading system using various deep learning techniques. Deep neural networks can extract features automatically. Many researchers have designed evaluation systems for various languages.

Automated grading system using LSA are also available. LSA is a machine learning method and the theory of information representation. LSA uses a mathematical approach to extract and infer relations from the contextual usage of words in the given dataset. We can evaluate answer sheets, articles, research papers, programming codes using

LSA. LSA uses a term-document matrix, and each row represents a term that occurred in the documents, while each column corresponds to each document in the dataset. The matrix is then decomposed using the SVD method into three other matrices, and their dimensions are reduced to remove the noise in the documents. Using SVD, new relationships between terms and documents get uncovered. Then the matrix will be used to obtain the similarity between the student's essay and the reference essay. In LSA, documents are mapped closer in the vector semantic space and cluster similar documents.

There is no study on how to assess the student's presentation skills. Although some researchers may consider it a minor aspect, the student must learn proper presentation skills. Design and delivery of a presentation are soft skills that will help students to increase employability skills in their professional lives. Project and Seminar presentations are essential academic activities in the curriculum of Indian universities in undergraduate studies. Presentation skill covers technical and non-technical aspects like a scholar's knowledge and presentation quality. The presentation should be graded based on the presentation quality and the accuracy and authenticity of the contents covered in the presentation. Our main objective is to evaluate the presentation quality of the PowerPoint presentations. The teachers use rubrics designed by their institute or department or sometimes use their expertise and experience to grade instead of using rubrics. This will lead to inconsistencies and inaccuracies in the assessment. Hence, we have developed automated system to grade students' PowerPoint presentations. The aim of our research study is to evaluate PowerPoint presentations with selected features and compare the grades awarded by LSA approach with grades awarded by the teachers. The features of student's

PowerPoint presentation are compared to the features that are found in a group of reference PowerPoint presentations in the semantic vector space. We have used the LSA approach to represent PowerPoint presentations in the semantic vector space. Students' PowerPoint presentations are graded using similar and nearest reference PowerPoint presentations using Cosine similarity and Kneighbors approach. Kneighbors predicts the grades of students' PowerPoint presentations with more accuracy as compared to Cosine similarity. Kneighbors and Cosine similarity approach give 90.90% and 81.81% accuracy respectively. Thus, the quality of grading of PowerPoint presentations is more reliable, robust, fast and free from favoritism and inconsistency.

The structure of this research paper is as follows. Literature review is presented in section 2. Section 3 describes methodology for automated grading of PowerPoint presentations using LSA. Feature extraction from PowerPoint presentations is presented in section 4. Singular value decomposition is illustrated in section 5. Grading of PowerPoint presentations using Cosine similarity and Kneighbours approach is illustrated in section 6. Final results using Cosine similarity and Kneighbours approach is discussed in section 7. Our work is concluded in section 8.

2. LITERATURE REVIEW

Several automated grading systems are available to grade different types of work automatically. Haendchen Filho et al. [3] developed an SVM model to grade high school children's essays. They used features emphasizing on argumentative structure, lexicon diversity, connectives, textual cohesion, and adherence to the theme. Efficiency of the machine learning model can be increased with a small dataset using imbalanced learning techniques [4]. Ajitiono and Widyani [5], Eid and Wanas [6], Contreras et al. [7], and Lam et al. [8] used Natural Language Processing (NLP) to extract a variety of linguistic features presenting the quality of essays like vocabulary, syntax, grammar, spelling, capitalization, and punctuation. Lexical features like whole word, prefix/suffix, stemmed word, lemmatized word. Grammar and syntax-related features like POS, usage of noun, verb, prepositional, conjunction. Also, features like vocabulary per passage, percentage of difficult words, rhetorical features, the proportion of grammar error, and usage errors. Further applied various machine learning techniques to grade essays.

Fazal et al. [9] developed a grading system to grade spellings using rubrics. They classified each word into four categories: simple, common, difficult, and challenging, and counted correct and incorrect words in each class. In the end, marks are assigned based on their rule-based algorithm. Leng et al. [10] proposed reviewing research articles using deep learning, and Parihar et al. [11] proposed a model to grade C programming assignments using clustering of similar submissions and measuring the distance from correct solutions in semantic space. Al-Jouie and Azmi [12] and Bashir et al. [13] graded long answers in Arabic. Ajitiono and Widyani [14] graded descriptive answers in the Indonesian language. Walia et al. [15] graded answers in the Punjabi language. Ratna et al. [16] graded answers in the Japanese language using a winnowing algorithm. In 2010, Peng et al. [17] built automated Chinese essay scoring using Vector Space Models. Suleiman et al. [18] developed poetry grading in Arabic language using Hidden Markov Model (HMM). They used

HMM for speech tagging, morphological analysis, syntactic structure, and text classification. Olowolayemo et al. [19] mapped students' answers with model answers to measure textual similarity using Levenshtein distance and Cosine similarity measures. Janda et al. [20] used the graph-based relationship to determine semantic similarity. They used SVM, Random Forest Regressor, and three-layer neural network models for predicting results.

Srihari et al. [21] developed a model to test the students' reading comprehension. Islam and Hoque [22] developed automated scoring for the Bangla language using LSA. Zen et al. [23] used LSA to grade computer programming assignments using cosine similarity between students' and reference assignments. Ratna et al. [24] proposed a grading system using LSA with learning vector quantization, an artificial neural network, and word similarity enhancement to grade answers. LaVoie et al. [25] used LSA techniques to score short answer responses to the consequences test. In 2010, Islam and Hoque [26] used n-gram instead of word for term-document matrix for the AEG system.

3. METHODOLOGY

Figure 1 depicts the proposed framework for automated grading of PowerPoint presentations using LSA. The grades of the PowerPoint presentations are evaluated by using the Kneighbors and Cosine similarity approach in Latent Semantic Space. The first process of this system is to extract features contributing to the quality of the PowerPoint presentations from all the PowerPoint presentations. Feature extraction is done by writing a program in python using the python-pptx library [2]. Then prepared a feature-document matrix. Each row of the matrix represents features in the PowerPoint presentations, while each column corresponds to each PowerPoint presentation. The matrix is then decomposed using the Singular Value Decomposition (SVD) method into three other matrices, and their dimensions are reduced to remove noise in the documents and unimportant details from the dataset. The truncated SVD matrices are used to prepare vectors for the PowerPoint presentations. Reference vectors represent the vectors of reference presentations, and query vector represents a vector of student's presentations whose grade is predicted by our system. The grade of the student's query vector is evaluated by finding cosine similarity with reference presentations or finding k number of nearest reference presentations. The grade of such similar reference presentations is assigned to the query vector. Table 1 contains the list of the features extracted from the PowerPoint presentations. Feature extraction is explained in detail in section 4. Here, we have shown a feature document matrix of 9 PowerPoint presentations.
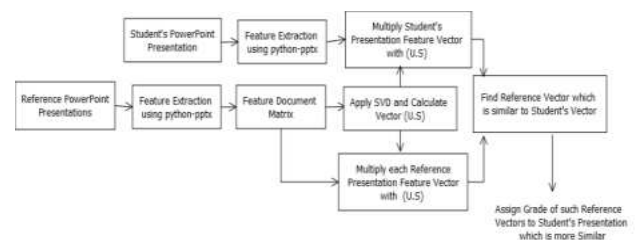
Figure 1. Block diagram of automated grading of PowerPoint presentations using LSA

Table 1. Feature-PowerPoint document matrix

Sr. No.	Features	PPT1	PPT2	PPT3	PPT4	PPT5	PPT6	PPT7	PPT8	PPT9
1	Total Slides	2	2	1	2	2	2	2	2	2
2	Tables	3	0	3	0	0	0	0	0	3
3	Images	0	3	1	1	1	0	1	1	1
4	Font types	2	2	0	1	0	1	0	0	2
5	Font color	2	2	2	0	0	0	1	0	1
6	Bold	1	1	1	0	1	1	1	1	1
7	Underline	0	1	1	0	0	0	1	1	1
8	Italic	0	1	1	0	0	0	1	1	1
9	Maximum Font Size	2	2	2	1	2	1	2	2	2
10	Minimum Font Size	2	2	2	2	2	2	2	2	2
11	Hyperlink	0	0	1	0	0	0	0	1	1
12	Footer	2	0	0	0	0	0	2	0	0
13	Date	2	2	0	0	0	0	0	2	2
14	Slide Number	2	2	0	0	0	0	2	2	2

4. FEATURE EXTRACTION

Python-pptx can be used to create and manipulate PowerPoint presentations. We have collected 86 PowerPoint presentations from our institute's undergraduate students, those were designed for Seminar presentation. They prepared PowerPoint slides using presentation software like MS Office, Python-pptx library. The feature extraction program is implemented in python, using the python-pptx library. We have considered features related to text appearance, graphics, footer, and hyperlink which check the student's efforts and contribute to the quality of PowerPoint presentations. These features will not contribute to the technical components of the student's presentation skills. We have extracted 22 features as shown in Algorithm 1. The PowerPoint presentation can be made effective by using the features related to the appearance of text, graphics, footer, and hyperlink as shown in Table 1. Hence, out of 22 features, we have considered 14 the most important features which contributes to categorize PowerPoint presentations in different grades. Machine learning algorithms require a labelled dataset. Each PowerPoint presentation is represented as a vector of 14 features with output label as its grade. Teachers have rated these presentations with Excellent, Good, and Fair grades. A panel of 3 teachers have independently graded PowerPoint presentations. The majority of the grades are assigned in the dataset as output labels with the permission of the experts. We have used 75 PowerPoint presentations as a training set or reference set in our experimentation and 11 PowerPoint presentations as query set or test set.

Algorithm 1:
Input: PowerPoint presentation
Output: List of the Features
1. From pptx import Presentation and extract features from each slide of the PowerPoint presentations.
   count=1
   ppt= Presentation(i), where i=1 to n,
        n=total PowerPoint presentations
2. Extract various graphics-related features by checking shape_type present in the slide and count them.
   for slide in ppt.slides:
   for shape in slide. Shapes:
     if (shape_type==13) indicates **Images**.
     if (shape_type==3) indicates **Charts**.
     if (shape_type==17) indicates **Textbox**.
     if (shape_type==19) indicates **Tables**.
     if (shape_type==14) indicates **Placeholders**.
3. Extract features related to the text appearance and text formatting by using the runs property of the paragraphs. Paragraphs are present

in the text_frame property of the shape.
- Check the hyperlink property of the texts and count the **Number of hyperlinks**.
  hlink=run.hyperlink
- Extract font property of the texts.
  font = run.font
- Extract different font styles used for the texts and count the **Number of font types**.
  font_name= font.name
- Extract different font sizes used for the texts and count the **Number of font sizes**.
  font_size=font.size.pt
  Find **Maximum and Minimum font size**.
- Using font property, check the presence of the Bold, Underline, Italic texts.
  font.bold! = None, font.underline! =None, font. Italic! =None indicates **Bold, Underline, and Italic** fonts.
- Extract different colors used for the texts and count the **Number of font colors**.
  font.color.rgb
4. Extract remaining features.
   phf = shape.placeholder_format
   if (phf.type==1) indicates **Title**.
   if (phf.type==2) indicates **Body**.
   if (phf.type==3) indicates **Centretitle**.
   if (phf.type==4) indicates **Subtitle**.
   if (phf.type==15) indicates **Footer**.
   if (phf.type==16) indicates **Date**.
   if (phf.type==13) indicates **Slide number**.

5. if end of the PowerPoint presentation, then **Total slides**= count
   else
       count = count+1 go to step 2.

5. SINGULAR VALUE DECOMPOSITION (SVD)

After extracting features from the PowerPoint presentations, the feature-document matrix is prepared. Here, the document is a PowerPoint presentation. In the feature document matrix, all features are put in a row. Total 14 rows are there in the feature-document matrix corresponding to 14 features, as shown in Table 1. Columns represent PowerPoint presentations. Feature-document matrix is decomposed by using SVD into three different matrices, as shown in Eq. (1). The first and third matrices are orthogonal vectors that describe a row entity and column entity. The second matrix is a diagonal that contains scalar values [24].

$$A_{txd} = U_{txn} * S_{nxn} * V_{dxn}{}^{T} \tag{1}$$

where, A is the feature-document matrix, U is the matrix that describes a feature, S is the diagonal matrix, and V^{T} describes

a PowerPoint presentation document. t is the number of features, i.e., 14, n is the latent semantic space dimension, d represents the number of PowerPoint presentations. Here we have taken PowerPoint presentations. The diagonal matrix S is obtained after applying SVD decomposition. Here, only diagonal values are shown. It is an eigenvector containing eigenvalue in decreasing order. We will consider only the first top 2 values.

S=[13.2563, 4.5605, 3.5058, 3.0361, 2.7971, 2.3939, 1.1474, 0.8404, 0.6206].

U=[[-0.40983662, -0.3101463], [-0.26914913, 0.78641571], [-0.2344467, -0.28823954], [-0.22563085, 0.13781735], [-0.23497369, 0.27701628], [-0.20223373, -0.05171161], [-0.13855827, -0.02911222], [-0.13855827, -0.02911222], [-0.40465076, -0.1147956], [-0.43350536, -0.23347783], [-0.0819615, 0.08617316], [-0.11381518, 0.10529971], [-0.24656913, 0.1259986], [-0.29508169, 0.00986846]]

V=[[-0.43283595, -0.42871556, -0.31376016, -0.19246775, -0.22122791, -0.19003774, -0.32154873, -0.33003494, -0.44271205], [0.50491871, -0.26095493, 0.34964887, -0.29655898, -0.36328906, -0.24469484, -0.26480748, -0.29757677, 0.34092318]]

Matrices U and V truncated by taking the first two columns and rows from U and V, respectively.

6. EVALUATION OF STUDENT'S POWERPOINT PRESENTATIONS

The truncated SVD matrices are used to make the PowerPoint presentation vectors [21]. The two rows in V^T represent PowerPoint presentations, and two columns in U represent features across two latent semantic spaces. The PowerPoint presentation vectors $d_{j'}$ with grades make the reference set or training set. The grade of a student's PowerPoint presentation is calculated as follows:

1. Calculate the dot product of U and S^{-1} as $U. S^{-1}$.

2. Calculate dot product of the above result with document vector.

$$d_j' = d_j^T . U. S^{-1}$$

where, d_j^T is the transpose of reference PowerPoint presentation vector.

3. Calculate dot product of student's PowerPoint presentation vector, i.e., also called as query vector with $U.S^{-1}$.

$$q_j' = q_j^T . U. S^{-1}$$

where, q_j^T is the transpose of the student's PowerPoint presentation or query vector.

4. The grades of the student's presentations are evaluated by finding cosine similarity with reference presentations or by finding k number of nearest reference presentations. The nearest or similar reference presentation grade will be assigned to the student's presentation. A similar reference presentation is found using Cosine similarity, and the nearest reference presentation is found using the Kneighbors algorithm.

6.1 Cosine similarity

Cosine similarity measures similarity between the two vectors. Let X and Y be two vectors. Cosine similarity between them is calculated as,

$$Cosine\ Similarity(X,Y) = \frac{X.Y}{||X|| * ||Y||}$$

where, $||X||$ and $||Y||$ are the length of vectors X and Y, respectively. Which are calculated as,

$$||X|| = \sqrt{\sum Xi^2} , ||Y|| = \sqrt{\sum Yi^2} \quad i=1,\ 2,\ 3...n$$

PowerPoint presentation, which has similar features, has a high LSA relationship, and will be positioned near to reference PowerPoint presentations in the latent semantic space and will have cosine similarity near to 1. The grade of such reference PowerPoint presentation will be set as a student's PowerPoint presentation grade.

For illustration, we have considered a feature-document matrix of 9 reference PowerPoint presentations as given in Table 1. Each row represents an individual PowerPoint presentation vector of size 1 x 14. After applying SVD from diagonal matrix S, the top 2 Eigenvalues are considered. Hence dimension of the reference vector becomes 1 x 2. Table 2 shows reference vectors after applying SVD.

Table 2. PowerPoint presentation vectors

Reference Presentation Vectors	Grade
ref1= [-0.43283595, 0.50491871]	Excellent
ref2= [-0.42871556, -0.26095493]	Excellent
ref3= [-0.31376016, 0.34964887]	Good
ref4= [-0.19246775, -0.29655898]	Fair
ref5= [-0.22122791, -0.36328906]	Fair
ref6= [-0.19003774, -0.24469484]	Fair
ref7= [-0.32154873, -0.26480748]	Good
ref8= [-0.33003494, -0.29757677]	Good
ref9= [-0.44271205, 0.34092318]	Excellent

Query vector is the PowerPoint presentation vector of size 1×14,

query vector=[2, 3, 1, 1, 0, 1, 0, 1, 2, 2, 0, 2, 2, 2]

After applying SVD, query vector of size 1×2 is obtained

query vector= [-0.40850238, 0.28362827]

Cosine similarity between query vector and reference vectors is calculated. Cosine similarity between the query vector and corresponding 9 reference vectors is as follows:

([0.9676087], [0.4051226], [0.973083], [-0.0312192], [-0.0598822], [0.0534046], [0.2715165], [0.2281435], [0.9987835])

We can observe that the query vector has the highest similarity with vector ref9, the 9th reference PowerPoint presentation. The grade of this PowerPoint is *Excellent*. Hence *Excellent* grade will be assigned to the student's PowerPoint presentation.

6.2 Kneighbors

It is a machine learning algorithm. We do not train a model like other machine learning algorithms during the training phase. "Instead, just store the reference presentations' vectors in the data structures. All presentation vectors are calculated in semantic space". The nearest reference presentations are found by calculating the Euclidian distance between reference presentations and students' presentations. Then k number of nearest reference presentations will be selected with minimum Euclidian distance measure. From the k number of neighbors, the most frequent majority output grade is assigned for students' presentations. Let X and Y be two vectors. Euclidian distance between X and Y is calculated as,

$$Euclidian\ Distance(X,Y) = \sqrt{\sum (X_i - Y_i)^2} \quad i=1, 2, 3 \dots n$$

Reference and query vectors are obtained using truncated SVD matrices. Euclidian distance between query vector and reference vector is as,

([0.2226243],[0.544958],[0.1154764],[0.619103],[0.203513], [0.57171],[0.555286],[0.586478],[0.0667309])

For k=4, depending on Euclidian distance, the nearest vectorsare ref1, ref3, ref5, and ref9 with grades *Excellent, Good, Fair,* respectively. The majority of the grade is *Excellent.* Hence *Excellent* grade is assigned to a student's presentation.

An *Excellent* grade is assigned to a student's presentation in both approaches.

7. EXPERIMENTAL ANALYSIS

Latent Semantic Analysis uncovers lexical-semantic links between the PowerPoint presentations. We have implemented grading of students' PowerPoint presentations using Cosine similarity and the Kneighbors approach.

7.1 Dataset

We have collected 86 PowerPoint presentations of the undergraduate students of our institute designed for the Seminar presentation. These presentations are evaluated by teachers with *Excellent, Good*, and *Fair* grades. Features are extracted using feature extraction program, written in python using the python-pptx library.
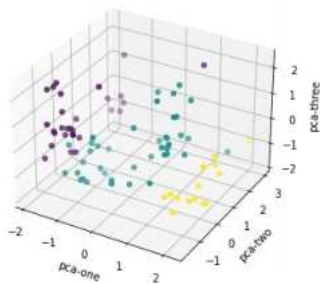

Figure 2. PowerPoint presentation dataset

As shown in Figure 2, our data set is a cluster of three classes corresponding to three output classes, i.e., *Excellent, Good, Fair.* Purple, green, and yellow color data points

represent *Excellent, Good*, and *Fair* presentations. We have total 86 presentation vectors corresponding to 86 PowerPoint presentations. We have used 75 PowerPoint presentations as a training set or reference set in our experimentation and 11 PowerPoint presentations as query set or test set.

7.2 Experimental analysis using Kneighbors approach

We have used the Kneighbors classifier from the sci-kit-learn library in our experimentation. We have considered 75 PowerPoint presentation vectors for training and 11 vectors for testing. We have repeated training and testing on the vectors by varying the size of vectors by changing eigenvalues from the diagonal matrix. Also we varied number of neighbors for the students' presentations. For the number of neighbors as 3 and PowerPoint presentation vector size 4 gives maximum accuracy. In grading of the PowerPoint presentation using Kneighbors approach gives 90.90% accuracy.

Table 3. Classification report using Kneighbors

Output Class	Precision	Recall	F1-score
Excellent	1.00	0.83	0.91
Good	0.67	1.00	0.80
Fair	1.00	1.00	1.00

Table 3 shows classification report of PowerPoint presentations using Kneighbors approach. Class *Fair* has precision, recall, and f1-score equal to 1. It shows that all presentations belonging to the class *Fair* are correctly classified. While presentations belonging to the class *Good* and *Excellent* are misclassified. From Figure 2, we can observe that data points of *Excellent* and *Good* classes are mixed at the boundary of the cluster, and *Fair* class data points are separated from other classes. So here, misclassification is occurring for *Excellent* and *Good* data points at the cluster boundary.

### 7.3 Experimental analysis using Cosine similarity approach

We have considered 75 vectors for training and 11 vectors for testing. We have found the Cosine similarity of each testing vector with all training vectors. We have observed performance by varying the number of elements from the diagonal matrix from 1 to 9. By taking the number of elements as 8, we have achieved accuracy up to 81.81%, as shown in Figure 3. Table 4 shows the classification report for the *Excellent, Good,* and *Fair* classes. Table 4 shows the classification report of PowerPoint presentations using Cosine similarity approach.

Table 4. Classification report using Cosine similarity

Output Class	Precision	Recall	F1-score
Excellent	1.00	0.83	0.91
Good	0.50	1.00	0.67
Fair	1.00	0.67	0.80

Figure 3 shows the accuracy achieved in the above experimentations by varying the vectors' dimensions by varying the elements in the diagonal matrix from 1 to 9. The accuracy obtained by the nearest neighbor approach is more significant than the cosine similarity approach. Hence, Kneighbors gives better performance compared to cosine

similarity. Using Kneighbors achieved an accuracy of 90.90% for the vector size 4. Using cosine similarity achieved an accuracy of 81.81% for the vector size 8. Kneighbors classifier accuracy gets reduced after increasing vector size greater than 4.
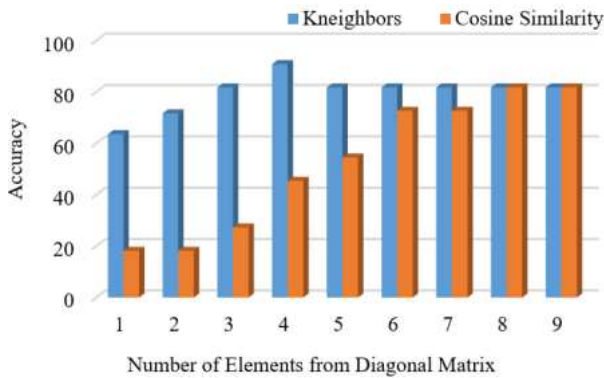
Figure 3. Accuracy using Kneighbors and Cosine similarity approach

8. CONCLUSIONS

We have extracted features from the PowerPoint presentations using the python-pptx library. We have represented students' PowerPoint presentations in the latent semantic space using LSA. The reference PowerPoint presentations similar to a student presentation are found using Cosine similarity and Kneighbors approach. Grades of such reference presentations were used to evaluate the grade of students' presentations. In the Kneighbors classifier, we have considered 3 nearest neighbors to predict the grade of the students' presentations. Kneighbors and Cosine similarity approach predict grades for the student's PowerPoint presentations with an accuracy of 90.90% and 81.81%, respectively. Kneighbors classifier achieved better accuracy compared to the Cosine similarity approach by using a lower-dimensional presentation vector compared to Cosine similarity.

REFERENCES

[1] Borade, J.G., Netak, L.D. (2020). Automated grading of essays: A review. In International Conference on Intelligent Human Computer Interaction, pp. 238-249. https://doi.org/10.1007/978-3-030-68449-5_25

[2] Borade, J.G., Kiwelekar, A.W., Netak, L.D. (2022). Feature extraction for automatic grading of students' presentations. In ICT Systems and Sustainability, pp. 293-301. https://doi.org/10.1007/978-981-16-5987-4_30

[3] Haendchen Filho, A., do Prado, H.A., Ferneda, E., Nau, J. (2018). An approach to evaluate adherence to the theme and the argumentative structure of essays. Procedia Computer Science, 126: 788-797. https://doi.org/10.1016/j.procs.2018.08.013

[4] Haendchen Filho, A., Concatto, F., Nau, J., do Prado, H.A., Imhof, D.O., Ferneda, E. (2019). Imbalanced learning techniques for improving the performance of statistical models in automated essay scoring. Procedia Computer Science, 159: 764-773. https://doi.org/10.1016/j.procs.2019.09.235

[5] Ajitiono, T., Widyani, Y. (2016). Indonesian essay

grading module using Natural Language Processing. In 2016 International Conference on Data and Software Engineering (ICoDSE), pp. 1-5. https://doi.org/10.1109/ICODSE.2016.7936117

[6] Eid, S.M., Wanas, N.M. (2017). Automated essay scoring linguistic feature: Comparative study. In 2017 Intl Conf on Advanced Control Circuits Systems (ACCS) Systems & 2017 Intl Conf on New Paradigms in Electronics & Information Technology (PEIT), pp. 212-217. https://doi.org/10.1109/ACCS-PEIT.2017.8303043

[7] Contreras, J.O., Hilles, S., Abubakar, Z.B. (2018). Automated essay scoring with ontology based on text mining and nltk tools. In 2018 International Conference on Smart Computing and Electronic Enterprise (ICSCEE), Shah Alam, Malaysia, pp. 1-6. https://doi.org/10.1109/ICSCEE.2018.8538399

[8] Lam, H.W., Dillon, T., Chang, E. (2011). Determining writing genre: towards a rubric-based approach to automated essay grading. In 2011 IEEE International Conference on Advanced Information Networking and Applications, Biopolis, Singapore, pp. 270-274. https://doi.org/10.1109/AINA.2011.32

[9] Fazal, A., Hussain, F.K., Dillon, T.S. (2013). An innovative approach for automatically grading spelling in essays using rubric-based scoring. Journal of Computer and System Sciences, 79(7): 1040-1056. https://doi.org/10.1016/j.jcss.2013.01.021

[10] Leng, Y., Yu, L., Xiong, J. (2019). Deepreviewer: Collaborative grammar and innovation neural network for automatic paper review. In 2019 International Conference on Multimodal Interaction, pp. 395-403. https://doi.org/10.1145/3340555.3353766

[11] Parihar, S., Dadachanji, Z., Singh, P.K., Das, R., Karkare, A., Bhattacharya, A. (2017). Automatic grading and feedback using program repair for introductory programming courses. In Proceedings of the 2017 ACM Conference on Innovation and Technology in Computer Science Education, pp. 92-97. https://doi.org/10.1145/3059009.3059026

[12] Al-Jouie, M.F., Azmi, A.M. (2017). Automated evaluation of school children essays in Arabic. Procedia Computer Science, 117: 19-22. https://doi.org/10.1016/j.procs.2017.10.089

[13] Bashir, A.M., Hassan, A., Rosman, B., Duma, D., Ahmed, M. (2018). Implementation of a neural natural language understanding component for Arabic dialogue systems. Procedia Computer Science, 142: 222-229. https://doi.org/10.1016/j.procs.2018.10.479

[14] Ajitiono, T., Widyani, Y. (2016). Indonesian essay grading module using Natural Language Processing. In 2016 International Conference on Data and Software Engineering (ICoDSE), Denpasar, Indonesia, pp. 1-5. https://doi.org/10.1109/ICODSE.2016.7936117

[15] Walia, T.S., Josan, G.S., Singh, A. (2019). An efficient automated answer scoring system for Punjabi language. Egyptian Informatics Journal, 20(2): 89-96. https://doi.org/10.1016/j.eij.2018.11.001

[16] Ratna, A.A.P., Luhurkinanti, D.L., Ibrahim, I., Husna, D., Purnamasari, P.D. (2018). Automatic essay grading system for Japanese language examination using winnowing algorithm. In 2018 International Seminar on Application for Technology of Information and Communication, Semarang, Indonesia, pp. 565-569. https://doi.org/10.1109/ISEMANTIC.2018.8549789

[17] Peng, X., Ke, D., Chen, Z., Xu, B. (2010). Automated Chinese essay scoring using vector space models. In 2010 4th International Universal Communication Symposium, Beijing, China, pp. 149-153. https://doi.org/10.1109/IUCS.2010.5666229

[18] Suleiman, D., Awajan, A., Al Etaiwi, W. (2017). The use of hidden Markov model in natural Arabic language processing: A survey. Procedia computer science, 113: 240-247. https://doi.org/10.1016/j.procs.2017.08.363

[19] Olowolayemo, A., Nawi, S.D., Mantoro, T. (2018). Short answer scoring in English grammar using text similarity measurement. In 2018 International Conference on Computing, Engineering, and Design (ICCED), Bangkok, Thailand, pp. 131-136. https://doi.org/10.1109/ICCED.2018.00034

[20] Janda, H.K., Pawar, A., Du, S., Mago, V. (2019). Syntactic, semantic and sentiment analysis: The joint effect on automated essay evaluation. IEEE Access, 7: 108486-108503.
https://doi.org/10.1109/ACCESS.2019.2933354

[21] Srihari, S., Collins, J., Srihari, R., Srinivasan, H., Shetty, S., Brutt-Griffler, J. (2008). Automatic scoring of short handwritten essays in reading comprehension tests. Artificial Intelligence, 172(2-3): 300-324. https://doi.org/10.1016/j.artint.2007.06.005

[22] Islam, M., Latiful Haque, A. (2013). Automated Bangla essay scoring system: ABESS. International Conference on Informatics, Electronics and Vision, ICIEV. https://doi.org/10.1109/ICIEV.2013.6572694

[23] Zen, K., Iskandar, D.F.A., Linang, O. (2011). Using Latent Semantic Analysis for automated grading programming assignments. In 2011 International Conference on Semantic Technology and Information Retrieval, pp. 82-88. https://doi.org/10.1109/STAIR.2011.5995769

[24] Ratna, A.A.P., Arbani, A.A., Ibrahim, I., Ekadiyanto, F.A., Bangun, K.J., Purnamasari, P.D. (2018). Automatic essay grading system based on latent semantic analysis with learning vector quantization and word similarity enhancement. In Proceedings of the 2018 International Conference on Artificial Intelligence and Virtual Reality, pp. 120-126. https://doi.org/10.1145/3293663.3293684

[25] LaVoie, N., Parker, J., Legree, P.J., Ardison, S., Kilcullen, R.N. (2020). Using latent semantic analysis to score short answer constructed responses: Automated scoring of the consequences test. Educational and Psychological Measurement, 80(2): 399-414. https://doi.org/10.1177/0013164419860575

[26] Islam, M.M., Hoque, A.L. (2010). Automated essay scoring using generalized latent semantic analysis. In 2010 13th International Conference on Computer and Information Technology (ICCIT). pp. 358-363. https://doi.org/10.1109/ICCITECHN.2010.5723884

Cavitation based pretreatment of biomass for intensification of biogas production

Swapnil M Mahajan, Sankalp K Salunkhe, Apurva A Mahadik & Sandip H Gharat*

Department of Chemical Engineering, Gharda Institute of Technology, Ratnagiri 415 708, Maharashtra, India

E-mail: sandipgharat78@gmail.com

Biogas, a clean and renewable form of energy, could very well substitute for conventional sources of energy (fossil fuels, oil, etc.) which are causing environmental problems. The present work investigates the application of hydrodynamic cavitation (HC) for the pretreatment of biomass with the objective of enhancing biogas production. Effect of different parameters viz.rice straw to water ratio (0.5%, 1%, 2%, 3%, and 4%), operating pressure (1-3 bar), and also treatment time (10-30 min) have been investigated using an orifice plate as a cavitating device. The water displacement method is used for the analysis of the quantity of biogas formation. As we increased the biomass ratio is increased from 0.5 to 3% with the same treatment time 15 min biogas yield also increased from 52 to 345 mL respectively. Combining chemical treatment with hydrodynamic cavitation it has been observed that it gives a maximum (470 mL) of biogas yield as compared to HC alone (360 mL) for the same biomass ratio of 4%. Overall, it has been established that a significant enhancement in the biogas production can be obtained due to the pretreatment using HC which can also be further intensified by combination with chemical treatment.

Keywords: Anaerobic digestion, Biogas, Hydrodynamic cavitation, Intensification, Lignocellulose

In today's energy-demanding lifestyle, the need for exploring and exploiting new sources of energy that are renewable as well as eco-friendly is a must[1]. Biogas, a clean and renewable form of energy, could very well substitute (especially in the rural sector) for conventional sources of energy (fossil fuels, oil, etc.) which are causing ecological–environmental problems and at the same time depleting at a faster rate[1]. Lignocellulosic biomass, such as agricultural residuals and energy crops is an abundant organic resource[2,3]. Large quantities of lignocellulosic residues accumulate from agricultural, forestry, municipal, and other activities[4].

Anaerobic digestion (AD) is a biological process in which organic matter is decomposed by an assortment of microbes under oxygen-free conditions and produces biogas[5]. The AD process can be divided into four steps as shown in. At the beginning of the process, hydrolysis occurs as extracellular enzymes, which are produced by hydrolytic microbes, decompose complex organic polymers into simple soluble monomers[6]. Proteins, lipids, and carbohydrates are hydrolyzed to amino acids, long-chain fatty acids, and sugars, respectively. These smallmolecules are then converted by fermentative bacteria (acetogens) to a mixture of volatile fatty acids (VFAs) and other minor products such as

alcohol. Acetogenic bacteria further convert the VFAs to acetate, carbon dioxide, and/or hydrogen, which provide direct substrates for methanogenesis, the last step of the AD process for methane production[4]. Lignocellulosic biomass mainly consists of three types of polymers: cellulose, hemicellulose, and lignin. The carbohydrate components (cellulose and hemicellulose) are fermentable after hydrolysis, which makes lignocellulosic biomass a suitable feedstock for bioenergy production. However, the inherent characteristics of native lignocellulosic biomass, such as structural and chemical properties, make it resistant to biodegradation by enzymes and microbes[4,6]. The properties of lignocellulosic biomass render it resistant to biodegradation. Due to the complexity and variability of biomass chemical structures, the optimal pretreatment method and conditions depend on the types of lignocellulose present[7]. Several structural and compositional properties were found to have impacts on the biodegradability of lignocellulosic biomass, including cellulose crystallinity, accessible surface area, degree of cellulose polymerization, presence of lignin, and hemicellulose To improve these properties pretreatment methods can be broadly classified into three types namely physical, chemical and biological[3,8,9]. Cavitation can be produced by the

Bioremediation of imidacloprid using *Azospirillium* biofertilizer and *Rhizobium* biofertilizer

Kavita Kulkarni[*,†], **Aishwarya Chawan**[*], **Anand Kulkarni**[*], **and Sandip Gharat**[**]

*Department of Chemical Engineering, Bharati Vidyapeeth (Deemed To Be University), College of Engineering, Pune
**Department of Chemical Engineering, Gharda Institute of Technology Lavel, Khed, Ratnagiri

Abstract–Imidacloprid is a pesticide used for agricultural purposes. Residue of pesticide in water and soil will affect the water and soil quality. Seepage out of imidacloprid to the ecological system could affect aquatic life as well as human. The toxic pollutants would affect the quality of agriculture run off, in turn contaminating water bodies acting as sink for these runoffs. Hence, there is need for reparation of these pollutants. *Azospirillium* biofertilizer and *Rhizobium* biofertilizer were used as adsorbent for the removal of imidacloprid. These biofertilizers have capability to reduce the harmful component as well as be useful for plant growth. *Azospirillium* bacteria and *Rhizobium* bacteria are competent for the removal of organic pollutant from wastewater. These biofertilizers maintain biological activity without any adverse effect. The adsorptive removal of imidacloprid by using *Azospirillium* biofertilizer and *Rhizobium* biofertilizer was investigated at different conditions using batch experimentation. Optimization of parameters, such as dosage, time, temperature, pH, and agitation speed, was carried out. Equilibrium adsorption was illustrated by Langmuir and Freundlich isotherms. The kinetic data was best described by intraparticle diffusion and pseudo-second-order model. Reusability study showed good removal efficiency of imidacloprid after fourth use also. The investigations show that these materials have potential to be an excellent alternative for removal of pesticides while supporting plant growth.

Keywords: Imidacloprid, Adsorption, Removal Efficiency, Biofertilizer

INTRODUCTION

Pesticides are widely used in the majority of agricultural production sectors to increase crop production. Most of the active components have long balance and as a result can easily enter water sources such as streams and shallow groundwater. Another common way of polluting the water assets is through the pesticide manufacturing industries. Toxicity of pesticides released in the environment damages the ecological balance [1]. Pesticides cause serious concern to the farmers and workers who get direct exposure and the general population who indirectly get exposed through food and water [2-6]. Because of non-biodegradability and toxicity, control of pesticides is essential to avoid contamination of food, water sources and damage to the environment [7,8]. It is most essential to have alternative technologies for the treatment of pesticides. Use of pesticides is directly done on soil or on the flora so that their action can be received easily into the environment. Harmful effect of pesticides has been observed on the natural habitat as well as community health. Ecosystem, health of human beings and fauna is mostly affected by dangerous pesticides. Adverse effect of these pesticides was seen after penetration to the applied field [9].

Several methods are employed for the treatment of pesticides, such as advanced oxidation processes [10,11], ozonation [12], photolysis [13], electrocatalytic oxidation [14], photo Fenton [15], bio-

degradation [16,17] photocatalytic degradation [18,19], nano filtration [20], hydrodynamic cavitation [21] and adsorption [22-26]. Due to high operational cost, less efficiency and hazardous waste generation make these methods unsuitable for the treatment of pesticides [27,28]; consequently, it is required to explore new methods which are effective, safe to environment and effective [29]. Among these methods, adsorption is supposed to be an alternative for the removal of pesticides and other pollutants because of being eco-friendly, simple, and low-cost technology [30]. Biosorption technology is a substitute for the removal of pesticides [31]. Biosorption is a fast process in which interaction between cell surface and adsorbate and live, alive, or immobile biomass. When live biomass is used, the removal mechanism may involve biodegradation along with sorption phenomena [32]. Various natural materials have been utilized for the removal of pollutants, such as agricultural residue, raw plants, animal material, and microalgae sludge [33-36]. Plant based materials have been widely used for the wastewater treatment, like peanut shell, phytolacca Americana biomass, Marula seed husk, cedar leaf, olive tree pruning, cork waste, maize stover [37-43].

Imidacloprid is a pesticide normally used for seed therapy to control sucking and biting insects. Also, it flows rapidly all through plant tissue, and provides protection to crops from insects [44,45]. Imidacloprid is extremely toxic, and globally its surface water concentration is in the range between 0.001 to 320 µg/L [46,47]. Imidacloprid (IMD) is commonly detected in surface waters and floor waters due to its excessive persistence, bioaccumulation and low biodegradability, which poses an extremely top threat to various ecological surroundings and human health [48-50]. Imidacloprid